

# **CONTROLLING EPITAXIAL MORPHOLOGIES ON THE MICROSCOPIC SCALE**

**THÈSE N° 1620 (1997)**

**PRÉSENTÉE AU DÉPARTEMENT DE PHYSIQUE**

**ÉCOLE POLYTECHNIQUE FÉDÉRALE DE LAUSANNE**

**POUR L'OBTENTION DU GRADE DE DOCTEUR ÈS SCIENCES**

**PAR**

**Karsten BROMANN**

physicien diplômé de l'Université de Hamburg, Allemagne  
de nationalité allemande

acceptée sur proposition du jury:

Prof. K. Kern, directeur de thèse  
Prof. R.J. Behm, corapporteur  
Dr H. Brune, corapporteur  
Dr M. Gioni, corapporteur  
Prof. D. Pescia, corapporteur  
Prof. W.D. Schneider, corapporteur

Lausanne, EPFL  
1997

## Version abrégée

Nous avons étudié des nanostructures métalliques sur le système particulier d'Ag sur Pt(111). Un microscope à effet tunnel à température variable a été utilisé pour étudier la structure de la surface et pour révéler les processus atomiques clef impliqués dans la formation de telles nanostructures.

Nous avons examiné trois méthodes de formation de nanostructures: La croissance auto organisée de l'épitanie moléculaire (MBE), l'exploitation des propriétés d'équilibre et la déposition contrôlée de nano-agrégats sélectionnés en taille par déposition douce.

La première partie met l'accent sur trois différents processus atomiques qui sont d'importance cruciale dans la croissance épitanie: la diffusion intracouche, la diffusion sur les bords et sur les coins d'îlots et la diffusion intercouche. En appliquant les théories de nucléation, l'énergie d'activation de la diffusion intracouche a pu être déterminée quantitativement. Elle est de  $168 \pm 10$  meV pour le système Ag/Pt(111), de  $60 \pm 10$  meV pour le système Ag/1mcAg/Pt(111) et de  $97 \pm 10$  meV pour l'Ag/Ag(111). La diminution drastique de la barrière de diffusion sur la première monocouche a pu être attribuée à des effets de contrainte. D'autre part, nous avons montré que l'anisotropie de la diffusion coin-bord est à l'origine de la croissance de structures dendritiques sur des substrats hexagonaux. Enfin nous avons développé une nouvelle méthode pour la détermination quantitative de l'énergie d'activation pour la diffusion intercouche. Cette méthode a été appliquée sur les systèmes Ag/îlots d'Ag/Ag(111) et Ag/îlots d'Ag/ Pt(111). L'énergie d'activation trouvée pour le premier système est de  $120 \pm 15$  meV, et de  $30 \pm 5$  meV pour le deuxième système. La connaissance de ces processus de diffusion est à la base d'un contrôle de l'auto organisation pendant la croissance MBE.

En deuxième partie, nous avons étudié deux structures d'équilibre. Premièrement, la morphologie de l'alliage confiné à la surface du système Ag/Pt(111), et deuxièmement la structure de relaxation des contraintes dans la première couche d'Ag déposée sur du Pt(111). Les structures caractéristiques à l'échelle nanométrique de ces deux systèmes ont pu être expliquées à l'aide de considérations sur des processus atomiques antagonistes qui contribuent à la formation des structures d'équilibre pour les deux systèmes. Dans le deuxième cas, l'existence d'une morphologie pseudomorphique réentrante qui évolue avec la présence d'une deuxième monocouche d'Ag a pu être expliquée à l'aide de calculs basés sur la théorie du potentiel effectif moyen.

Finalement, nous avons étudié la possibilité d'utiliser la déposition douce des nano-agrégats sélectionnés en taille pour créer des populations d'îles monodispersées. Nous avons trouvé que le paramètre décisif pour une déposition non destructive est l'énergie cinétique par atome dans les agrégats. Le seuil au delà duquel le substrat est endommagé est de 1 eV par atome. Nous avons également montré qu'il est possible de protéger efficacement le substrat lors du bombardement d'agréats en déposant au préalable une multicouche d'Argon. Ceci donne la possibilité d'effectuer une déposition douce à des énergies d'impact élevées.

## Abstract

The controlled formation of metallic nanostructures was studied using the model system of Ag on Pt(111). Variable-temperature scanning tunneling microscopy was used to image the surface morphology and to identify the key atomic processes involved in the formation of such structures.

Three methods of nanostructure formation were investigated: self-organized growth in molecular beam epitaxy (MBE), exploitation of equilibrium properties, and controlled deposition of size-selected clusters by soft-landing.

The first part focuses on three different atomic diffusion processes that are of crucial importance in MBE-growth, being intralayer diffusion, corner and edge diffusion, and interlayer diffusion. Applying nucleation theory, the activation energy of intralayer diffusion could quantitatively determined to be  $168 \pm 10$  meV for the system Ag/Pt(111),  $60 \pm 10$  meV for Ag/1MLAg/Pt(111), and  $97 \pm 10$  meV for Ag/Ag(111). The drastic decrease of the diffusion barrier on the first ML could be attributed to the compressive strain in this layer. Second, an anisotropy of corner-to-edge diffusion was shown to be the origin for dendritic growth of islands on hexagonal substrates. Finally, a new method for the quantitative determination of the activation energy of interlayer diffusion was developed and applied to the systems Ag/Ag-islands/Ag(111) and Ag/Ag-islands/Pt(111). The activation energies were found to be  $120 \pm 15$  meV in the former case and drastically reduced to  $30 \pm 5$  meV in the latter case. The knowledge of these three types of diffusion is a necessary prerequisite to control the self-organization process of nanostructures in MBE-growth.

In the second part, two equilibrium structures were investigated: first, the morphology of the surface-confined alloy of the Ag/Pt(111) system, second, the strain relief structure of the first ML of Ag on Pt(111). The microscopic morphologies of these two systems could be explained as a result of competing

atomic effects that lead to equilibrium structures with characteristic features on the scale of nanometers. In the latter case, the existence of a reentrant pseudomorphic morphology that evolves with the presence of second ML material could be explained using effective-medium theory.

Finally, cluster deposition under controlled soft-landing conditions and its potential as an alternative route to create monodispersed island populations was studied. The kinetic energy per atom in the cluster was determined to be the decisive parameter for a nondestructive deposition. The threshold above which damage of the bare substrate occurs was determined to be 1 eV per atom. Predeposited Ar buffer layers were shown to dissipate efficiently the kinetic energy of the clusters, providing the possibility of a soft-landing even for elevated impact energies.

## Table of contents

|          |  |            |
|----------|--|------------|
| <b>1</b> | <b>Introduction.....</b>   | <b>1</b>   |
| <b>2</b> | <b>Experimental.....</b>   | <b>13</b>  |
| <b>3</b> | <b>Diffusion.....</b>  | <b>23</b>  |
| 3.1      | Nucleation theory.....   | 23         |
| 3.2      | Effect of strain on surface diffusion and nucleation.....  | 32         |
| 3.2      | corner diffusion as origin for dendritic<br>growth on hexagonal substrates.....  | 44         |
| 3.3      | Interlayer mass transport in homoepitaxial and<br>heteroepitaxial metal growth.....  | 57         |
| <b>4</b> | <b>Equilibrium and embedded nanostructures .....</b>   | <b>67</b>  |
| 4.1      | Stability of disk and stripe patterns of<br>nanostructures at surfaces.....  | 68         |
| 4.2      | Stress relief via island formation of an<br>isotropically strained, bimetallic surface layer: the<br>mesoscopic morphology of the Ag/Pt surface alloy..... | 79         |
| 4.3      | Reentrant pseudomorphic growth in metal heteroepitaxy  | 88         |
| <b>5</b> | <b>Cluster deposition.....</b>   | <b>101</b> |
| 5.1      | Controlled deposition of size-selected silver nanoclusters....   | 101        |
| <b>6</b> | <b>Outlook.....</b>  | <b>111</b> |
| <b>7</b> | <b>References.....</b>   | <b>113</b> |



# 1 Introduction

In recent years, nanostructure formation has become an increasingly important subject. This development was triggered, on one hand, by the intrinsic scientific interest in structures of reduced dimensions, their physical properties, their morphological stability, and last but not least the fascinating question how matter can be formed and manipulated on an atomic length scale. On the other hand, there is the expectation that the gained knowledge can be transferred into new technological applications. Often given examples in this context are quantum well laser diodes [1] or new magnetic recording media [2]. The performance of both relies crucially on the ability to grow ultrathin epitaxial films with atomic precision. Instead of stressing these examples again, I want to emphasize the future importance of this field of research by quoting from an article published in the German weekly newspaper "Die Zeit" [3]. This article, reporting from a workshop on nanotechnology held in Munich and attended by several leading scientists and by representatives of high-tech companies like Hitachi, NTT, and Mitsubishi, refers to nanotechnology as the "key technology of the 21<sup>st</sup> century". Visions of potential applications that were discussed on the workshop included "storage devices and circuits working with single electrons", chemical data storage with "self-organizing""supra-molecules", or sensors that are able to detect single molecules or that can "infer the complete medical history of a patient out of a drop of blood". However, the text emphasizes as well that "there are only a few products of nanotechnology that are ready for the market today"<sup>1</sup>.

This quotation shows that nanotechnology today has still potential character in most cases. The present thesis, too, does not aim at a technical application, but focuses on basic research. In general, the relation between basic research and application is -correctly- regarded as the former supplying the basis

---

<sup>1</sup> Translations by the author.



of the latter. However, I want to introduce the object of this study further by giving a somewhat different look on the relation of these two.

A typical method of nanostructure formation is self-organized growth in molecular beam epitaxy (MBE). Here, material is evaporated onto a crystalline substrate in the form of single atoms that subsequently arrange according to the laws of nature. This process is of course determined by the externally controllable growth parameters like substrate temperature, deposition flux, choice of substrate and adsorbate, use of surfactants, etc. In any field of application, it is indispensable to have the "know-how" of relating the external parameters to the resulting growth morphologies in order to fabricate the desired structures. This know-how can either be achieved by simple "try-and-error", resulting in recipes of growth procedures, an approach being time- (and hence cost-) intensive and scientifically not very tempting. Provided with a detailed knowledge of the atomic processes governing the growth, on the other hand, we can purposely control the external growth parameters and thus either tailor the desired structures or create new ones. The course followed in basic research (and throughout the most parts of this thesis) often starts from playing with the external parameters (this "playing" of course being quite systematic). The researcher then has the task to infer the physics of the atomic processes out of the morphological properties of the structures he or she has created. In this picture, basic research and application are not so different from each other. They only start from different points in the loop of mutual dependencies schematically sketched in Figure 1.1.

Besides the already mentioned self-organized growth, there are different approaches for the nanostructuring of surfaces, all of them having their specific advantages and disadvantages. The perhaps most spectacular one is atomic manipulation with scanning-probe methods [4-6], during which the desired structures are assembled atom by atom with the tip of a scanning tunneling microscope. Though arbitrary atomic scale structures can be created using such

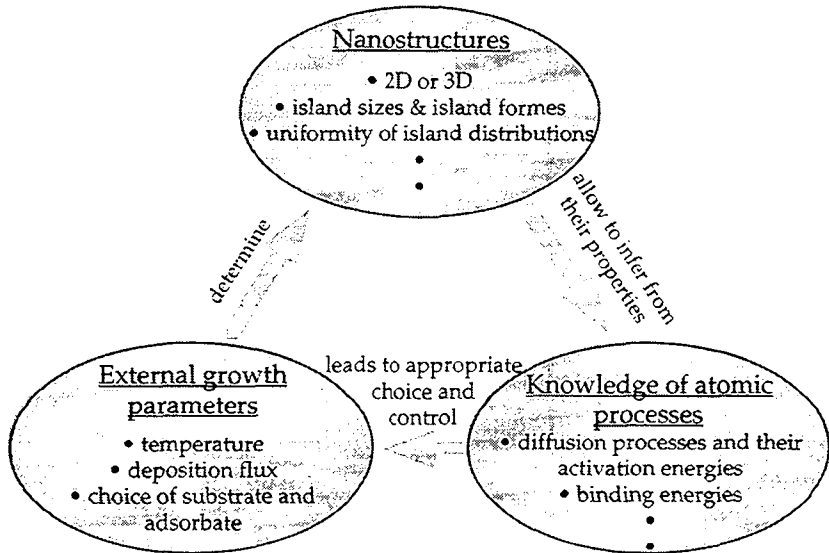


Fig. 1.1: Mutual dependencies between different aspects involved in nanostructure formation. See text for further information.

techniques, the principle drawback of the method is its time consuming serial character. This approach is not treated in the present thesis. The second approach, self-organized growth, has the advantage of creating a large number of structures simultaneously in a parallel process [7]. Its disadvantage, however, is the limited degree of control one has over the atomic motions in diffusion and nucleation processes. As such processes are basically governed by statistics, this statistics reflects itself in the variance of the structures that form during growth. Here, a detailed knowledge of the processes involved can help to find ways to increase the uniformity of the resulting structures. Alternative ways of nanostructuring can make use of equilibrium properties of the studied systems or can try to create well defined structures before they are transferred onto the supporting substrate. Examples of the latter three approaches will be discussed in the course of this thesis on the example of Ag structures on a Pt(111) substrate.

The present thesis focuses on the morphological properties of metallic nanostructures. The appropriate method to gain structural (real space) information is microscopy, and, as the features examined are metal structures of nanometer size, we used scanning tunneling microscopy (STM) as a tool that permits measurements down to the atomic scale [8-10]. The structures of interest are often metastable and exist only in limited temperature ranges. Equilibrium properties, too, normally depend on temperature. The experimental set-up has thus to provide the possibility to perform measurements at varying temperatures. We used variable-temperature STM to meet these requirements. In chapter 2, the experimental prerequisites for this study are presented. I want to emphasize that it is of course necessary for a more complete understanding to relate structural information obtained by STM with the findings of other methods, either experimental or theoretic ones. Consequently, parts of this work originated from collaborations with other groups employing He-diffraction on the experimental side (chapter 4.2), or effective-medium theory calculations (EMT) as theoretic example (chapters 3.2 and 3.3).

The key issue of this study was to go beyond a mere description of structures and their formation. By relating the experimental findings to models and theory, and by application of theoretic methods like EMT, we show that it is -at least in some cases- possible to gain *quantitative* information on the key atomic processes involved in nanostructure formation.

The third chapter shall serve as an example for this approach. As a model system, we study MBE-grown Ag structures on the Pt(111) substrate. Epitaxial growth normally takes place under conditions far from equilibrium. (The growth-"process" itself requires the existence of some sort of gradient. In perfect equilibrium, we cannot have any kind of processes except of fluctuations around the equilibrium state.) The growth and the resulting structures are hence governed by kinetic effects. Among the most important of such effects are atomic

diffusion processes. We will address three types of atomic diffusion which are of crucial importance in epitaxial growth, namely intralayer (chapter 3.2), corner and edge (chapter 3.3), and interlayer diffusion (chapter 3.4).

In the limit of a strict two-dimensional (2D) growth, the structures that form after deposition of submonolayer coverages of adatoms on the surface are flat islands of monoatomic height. Their density and their average size show in many cases a characteristic dependence on temperature, deposition flux, and coverage. This dependence is related to the intralayer diffusivity and can be described by mean-field nucleation theory [11, 12]. If applied with caution, mean-field nucleation theory can hence be used to obtain quantitative information on the energy barrier  $E_m$  and the prefactor for surface diffusion [13]. Using this approach, we show that the intralayer diffusivity depends strongly on strain. This finding is not only important for the tailoring of island distributions. It is as well a basic ingredient of the understanding of heteroepitaxial film growth in the kinetic regime. In heteroepitaxial systems, strain, resulting from lattice mismatch between the two components, is always existent in the first epitaxial adlayers, as they have to adopt the lattice constant imposed by the substrate<sup>1</sup>. Upon further growth, the film can relax through introduction of misfit dislocations. As strain influences the intralayer diffusivity, it determines how often adatoms can visit the edges of islands on which they were deposited during the growth process. Only if the visiting frequency is sufficiently high, they have the possibility to diffuse over the edges before they meet other adatoms and form the nucleus of a new island on top of the existing one, which would be the onset of a three-dimensional (3D) growth. Changes of the intralayer diffusivity, induced by varying strain in different layers of the growing film, can hence be the reason for kinetic growth instabilities in epitaxy.

---

<sup>1</sup> The only exception of this rule are alloy systems for which it is sometimes possible to tune the composition of the respective components in a way to guarantee nearly misfit-free layer structures.

A second important point whether or not the adatoms can visit the island edges is their average diffusion length towards the steps. It is evident that, on a compact island, the average distance to the nearest island border will be larger than on ramified islands of the same total size. Indeed, the formation of ramified islands has been shown to be responsible for the low-temperature 2D growth in Pt(111) homoepitaxy<sup>1</sup>. Our interest in island shapes, however, aroused from the fascination by the forms themselves rather than by their implications for multilayer growth. The question whether an island grows in a compact or ramified manner is basically determined by the amount of atomic diffusion that is allowed along the island edges and around its corners<sup>2</sup>. In the limit of thermal equilibrium, the shape of the island is determined by the relation of the free energies of the atomically different steps which form the island borders. The resulting form can be explained by the Wulff-construction [16]. In the other limit of completely forbidden edge diffusion, the atoms arriving laterally stick irreversibly at the places where they hit the aggregate. This gives rise to the fractal structures forming in the so-called diffusion-limited aggregation (DLA) process [17-19]. Though ramified islands with a fractal dimension of  $\approx 1.7$  as predicted by DLA have indeed been found in metal adsorption systems, these islands show significant deviations from DLA aggregates. First, they never have monoatomic armwidths, which shows that at finite temperature at least some processes of edge diffusion are activated in any real system [20, 21]. More strikingly, Ag islands that form in low-temperature aggregation on substrates of Pt(111), Ag(111), and the

---

<sup>1</sup> The main reason for 2D growth in that case, however, is not the short diffusion way towards the edges, but rather the existence of many kink sites in the edges which are absent for growth at elevated temperatures where compact islands form [14]. At these kink sites, the *interlayer* diffusion is strongly enhanced, providing the possibility for the atoms to descent from the ramified islands [15].

<sup>2</sup> Of course, the relevant measure is not the *absolute* value of the diffusivity, but its relation to the impinging flux of atoms. If edge diffusion is activated, but is so slowly that many new atoms arrive at the island edge before an atom can make a single step, we can regard edge diffusion as frozen in.

first ML of Ag on Pt(111) exhibit so-called dendritic patterns with trigonal symmetry and preferential growth of the arms in the crystallographic  $\langle \bar{1}\bar{1}2 \rangle$  directions instead of being randomly ramified. Using EMT, this behavior could be attributed to the anisotropic diffusion of atoms from (one-fold coordinated) corner sites towards the two different types of step edges always present on hexagonal close-packed surfaces.

Interlayer diffusion, the last type of atomic displacements treated in chapter 3, is the perhaps most determining parameter for whether a system in the kinetic regime grows two- or three-dimensionally. An adatom, approaching the upper edge of a step, normally experiences an increased energetic barrier  $E_s$  for stepping down than for diffusing laterally over the terrace. This additional activation energy is often called Schwoebel or Ehrlich barrier [22-24]. If this barrier is too high to be overcome at a given temperature and, hence, interlayer diffusion is prohibited, the adatom will be restricted to stay on its island no matter how often it visits the edges. Sooner or later, it will nucleate with other atoms into a new island on top of the existing one, leading to 3D growth.

In chapter 3.4, we present a method to determine the additional step edge barrier for interlayer diffusion  $\Delta E_s = E_s - E_m$  with the STM through a measurement of the nucleation rate on top of previously grown adlayer islands. This nucleation rate depends strongly on the adatom density on top of the adislands. The adatom density, in turn, is determined by the rate at which the adatoms diffuse over the island edge and get lost. Experimentally, compact 2D adlayer islands of well defined size are built via deposition of a submonolayer coverage at low temperatures and subsequent annealing [7]. After a second deposition of a submonolayer coverage, the nucleation on top of the preexistent islands and its dependence on the island size and temperature is examined. This experiment is a nice example for the relations mentioned above between the knowledge of the atomic processes involved in nanostructure formation and the

application of this knowledge. The way to learn more about the atomic processes (here, the quantitative determination of  $\Delta E_s$ ) is to make use of previously gained information and to perform an experiment on a purposefully nanostructured surface.

So far, we discussed kinetic processes that are responsible for the self-organization in MBE growth. Interesting structural properties, however, are not restricted to systems far from equilibrium (although, there, the variety of structures is larger). In chapter 4, we present two equilibrium (or near equilibrium) structures that can serve as an example. Both of them form within a respective layer, which is why we call them "embedded" nanostructures. The first is the morphology of the surface-confined alloy that forms when submonolayer coverages of Ag on Pt(111) are annealed to temperatures above  $\approx 550$  K and mix into the topmost Pt layer. The microscopic structure of this alloy consists of small Ag clusters embedded in the Pt layer (for low Ag coverages) or of small Pt inclusions in a Ag layer (for coverages near 1 ML). The second example are the strain-relief structures of the first ML of Ag on Pt(111) that build up in compact films grown at temperatures between 250 K and 550 K. In both cases, there are competing energetic contributions to the total energy that tend to drive the system into different directions. The properties of the system's ground state reflect a detailed balance between these contributions, which can lead to a complex overall structure. We will demonstrate this in particular for the case of the Ag/Pt alloy. Here, we find such an interplay between different effects on three levels. The first concerns the question why the alloy forms at all, and why it is restricted to the surface. A simple approach to understand binary systems is based on the balance of surface and interface energies. If for a given system the interface energy is negative, the two materials can in principle lower their energy by intermixing. A considerable amount of strain, i.e., different atomic radii, may suppress the miscibility in the bulk and can restrict the alloy to the surface. This simple picture, however, cannot explain why the intermixing in our system stops

at the formation of small clusters. In the case of a negative interface energy and principle miscibility in the first substrate layer, there is no reason why the alloying is not complete<sup>1</sup>. It was demonstrated by Tersoff [25] that both of the two energetic contributions mentioned above can actually point into the opposite direction. Using a simplified model of a binary system that included only strain energy, he could show that strain may induce alloy formation in the first substrate layer (while intermixing becomes energetically unfavorable in deeper layers). If the strain turns out to be the reason for alloying, a *positive* interface energy can lead to domain formation in the intermixed layer.

We find an interplay of opposing energetic contributions a second time when we examine the microscopic structure of the alloy more closely in chapter 4.1. This structure undergoes a coverage-dependent transition from compact clusters of an average diameter of about 10 Å for coverages below 0.25 ML to elongated, meandering stripes forming a labyrinthine pattern for coverages of 0.3 ML or above. The driving force for this behavior is again the strain that is still existent in the mixed system. (Though the elastic energy in the system is already lowered by the formation of the alloy, the Ag atoms in the topmost layer still disturb the Pt lattice). Here, the two effects that act against each other are the gain in free energy by the relaxation of elastic energy due to the formation of domain boundaries, and the energy cost due to the long-range effective repulsion between these boundaries. The relation between these two energetic contributions is different for unidirectional or two-dimensional domain-boundary structures, and it changes with the amount of Ag dissolved in the Pt matrix layer. It is hence possible that, at a critical coverage, the total energy for the "striped" phase drops below that of the "disk" phase, which drives the transition observed for Ag/Pt(111).

---

<sup>1</sup> These structures are the real equilibrium state of the system and are not due to a kinetically hindered, incomplete mixing process. This will be demonstrated in chapter 4.1.



A third group of different energetic effects is important for the formation of the mesoscopic structure of the alloyed surface. (We here refer to "mesoscopic" as occurring on the length scale of typical substrate terraces, i.e., of about 1000 Å. The structures that form on the terraces are smaller and can thus still be considered as "nanostructures"). Upon annealing of the surface alloy to 900 K, round islands with a preferential diameter of 150-300 Å form on the terraces. These islands, as well as the terraces, consist microscopically of the structures described above. The reason for the formation of this superstructure is -once again- related to the not yet completely relieved strain. On this level, the system can lower its energy by the relief of strain at step edges. However, the formation of steps is generally disfavored. The energetic compromise found by the system is to increase the total length of its steps by island formation (and thus to guarantee an efficient relief of strain for these islands), but to minimize the energetic cost of step formation by optimizing the ratio of surface area to perimeter length for each respective island. A further energetic factor, the effective repulsive step-step interaction, is responsible for the homogenous distribution of the resulting structures on the surface.

The second example of structure formation in equilibrium systems which is treated in chapter 4 concerns the superstructure of dislocations that form in compact first monolayer Ag films grown on Pt(111). (As we have seen, the "real" equilibrium state of submonolayer coverages is formed by the surface alloy. We now treat the ground state of the (metastable) system with still well separated substrate and adsorbate phases). The structure of the dislocation network itself is not our primary interest. It consists of pairs of partial dislocation lines separating regions of fcc and hcp stacking. The two lines run perpendicular to the close-packed atomic rows and permit unidirectional strain relief along these rows. Three classes of dislocations (along the three  $\langle \bar{1}\bar{1}2 \rangle$  directions) allow for elastic relaxation into all directions. The interesting fact in our context is that the appearance and disappearance of the dislocations in the first ML can be tuned by a

controlled preparation of the system. Dislocation formation in this system requires a minimum island size. Below this critical size, the islands can efficiently relieve their strain at the edges, and pseudomorphic growth of the 2D islands is observed. Above the critical size, a dislocated morphology becomes energetically favored. Interestingly, the dislocation network can be lifted by the presence of second ML material on top of the Ag monolayer. The reason for this structural transition is again related to a detailed balance between different energetic factors [26], being first the gain in elastic energy due to introduction of misfit dislocations, second the loss in binding energy as a part of the atoms in the dislocations has to shift out of registry, and third the chemical potential of Ag atoms on top of the first layer. Such an adatom gas exists in the presence of second ML material, as for the temperatures where we find the dislocations there is always a certain amount of Ag evaporation from the steps. Using EMT, we show that already a very low density of this adatom gas can drive the structural transition, as the first two of the mentioned energetic factors nearly cancel each other in our system.

In the last part of the present thesis, we treat an alternative way of nanostructure formation. As mentioned in the beginning, self-organized growth has the disadvantage of depending on statistics. In the case of island populations grown with MBE, this statistics gives rise to a typical distribution of the island sizes found on the surface that scales for different growth conditions [27, 28]. In the case of Ag islands on Pt(111), the characteristic variation as a function of average island size was measured to be rather large,  $\sigma^* = 0.55$ .

A promising route to form island populations with better defined sizes is to lift the restriction imposed by MBE of depositing single atoms, and to use directly size-selected nanoclusters instead. One can hope that the aggregates that form upon deposition of such objects from the gas phase will maintain the same sharp size distribution. In a normal cluster deposition experiment, however, the energy that is released during the impact is sufficient to disintegrate at least parts of the

clusters or to create even substrate damage or implantation. One has thus to guarantee a non-destructive softlanding in order to ensure that the nanoclusters maintain their individual characteristics. A promising way to achieve this has been proposed by Cheng and Landman [29, 30], who studied in detail the deposition dynamics of Cu nanoclusters on Cu(111) by molecular-dynamics simulations and proposed controlled softlanding via energy dissipation in a rare-gas buffer layer. In chapter 5 we demonstrate that this approach is indeed feasible. We study the deposition of size-selected  $\text{Ag}_n$  clusters ( $n = 1, 7, 19$ ) with varying kinetic energies (20 - 100 eV) onto the bare Pt(111) surface and into a previously adsorbed Ar buffer layer which is subsequently evaporated to land the clusters with zero kinetic energy onto the surface. By controlled annealing experiments, we demonstrate that the buffer layer can efficiently protect the surface from sputter defects. Further, we show that in the latter case the size distribution of the aggregates that form on the substrate is significantly sharper than in the former case (the former leading to a size distribution equal to that obtained in MBE-growth). The findings indicate that soft-landing of clusters through application of rare-gas buffer layers for efficient energy dissipation may indeed be a future possibility to create monodispersed island populations on surfaces. The experiments, however, show as well that it can be dispensable to employ such a rather complicated technique. By lowering the kinetic energy per atom in the cluster under a threshold of 1 eV per atom, the same non-destructive landing behavior with a comparably sharp size distribution could be obtained.

The main chapters of the present thesis consist of articles that were published during the experimental work. These articles are presented in their original form, except for editorial changes like renumbering of figures and tables or the update of the bibliography. For each chapter, an additional introduction will set the articles in the context of other work done in the field or will give supplementary information to that provided by the publications.

## 2 Experimental

The aim of the present thesis was to study some of the relevant processes involved in metal epitaxy in their pure form, i.e., without the interference of other atomic species than the two metals examined. The appropriate way to do so is to make use of an ultra-high vacuum (UHV) apparatus. The UHV chamber built up during this work is equipped with standard surface analysis tools: quadrupole mass spectrometer, LEED-system, and Auger-electron spectrometer with cylindrical mirror analyzer. A sputter gun is mounted for sample cleaning. The typical cleaning procedure of the Pt(111) crystal consisted in repeated cycles of flash annealing to 1200 - 1400 K, Ar ion sputtering at  $T \approx 900$  K ( $E_{Ar} \approx 1000$  eV, giving a sputter yield of  $\approx 1$  [31]), and oxygen exposure at  $T \approx 900$  K ( $p_{O_2} \approx 5 \cdot 10^{-8}$  mbar). Material can be evaporated either by an MBE Knudsen cell (for materials with a low melting temperature and a high vapor pressure) or by an electron beam evaporator. The silver films studied in this thesis were exclusively grown with the Knudsen cell. The STM was used for the calibration of the deposition flux.

The main analysis tool is the variable-temperature STM [32-34]. It consists of two components, the STM itself and a manipulator that carries the sample and permits temperature control. The sample is mounted on a holder that is thermally coupled to a liquid-He flux cryostat. The coupling is made by a copper braid to combine a maximum of thermal conductivity with a minimum of external vibrations imposed on the sample holder. The sample holder itself is mounted by pulling and pushing screws to a Cu block which serves as a massive support. This set-up guarantees mechanic stability and leaves only the small sample holder to be cooled via the braid. For heating of the sample a filament is mounted closely to the back side of the crystal. The sample can be heated either by radiation or by electron bombardment from the home-made W/Re (3 - 6 % Re) filament. The temperature is measured by a NiCr/Ni thermocouple spot welded

to the rim of the hat-like shaped sample and a commercial temperature controller [35]. Calibration of the temperature measurement was performed outside of the chamber with an identical thermocouple (including as well a similar UHV feedthrough) for two thermodynamic equilibrium temperatures, that of boiling liquid  $N_2$  and a water-ice mixture. The absolute accuracy and reproducibility was determined to be about  $30\text{ }\mu\text{V}$ , corresponding to  $\pm 1\text{ K}$  at  $77\text{ K}$ . Temperature control in the cryogenic region is achieved by applying the full cooling power and regulation of the temperature by radiative heating. The obtained stability is  $0.1\text{ K}$ . The whole manipulator is mounted on a rotatable flange. By turning the manipulator the sample can be brought in front of all preparation and analysis tools in the chamber. This makes sample transfer dispensable and permits full temperature control during any phase of an experiment.

The second component of a variable-temperature STM is the microscope itself. The type of STM normally used for studies at varying temperatures is the "beetle" STM [36]. Its geometry of three supporting piezo tubes fixed to a metal head with the central scanning piezo tube (the central piezo is laid out as a "single tube scanner" [37]) is appropriate for variable-temperature applications as thermal contractions and dilatations of the support and scan piezos cancel each other to a first approximation, leading to reduced thermal drift problems. Measurements are done by putting the STM on a circular triple helix Mo-ramp surrounding the sample. For the coarse approach of the tip, as well as for lateral movement over the sample, an inertial drive is used, i.e., triangular pulses are applied to the external piezos, leading to alternate bending and sliding over the ramp.

The constructive part of this thesis focused on ways to increase the resolution of the original STM [33] by better vibration isolation and damping. The conceptual changes of the original design of the manipulator are shown in

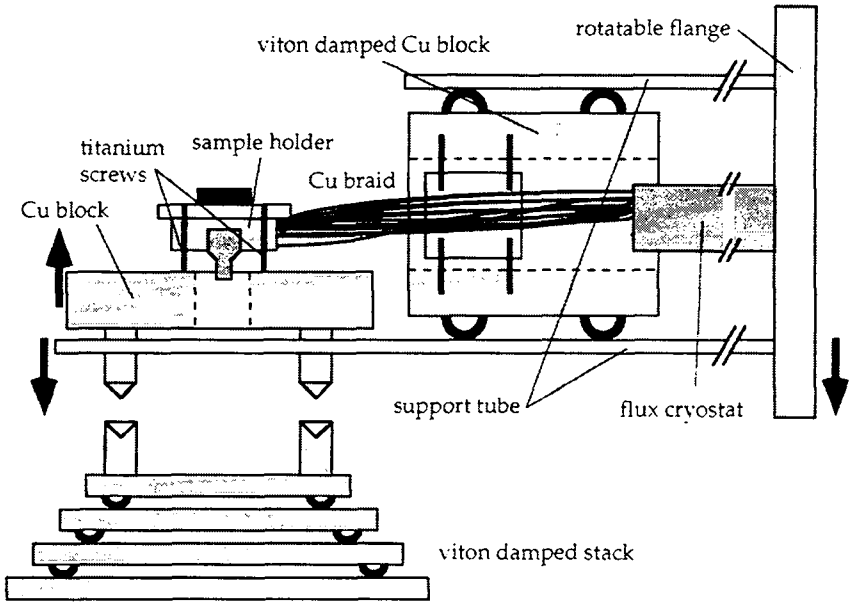
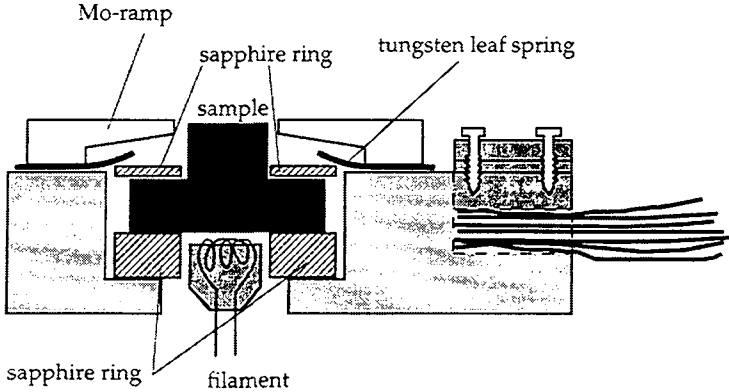


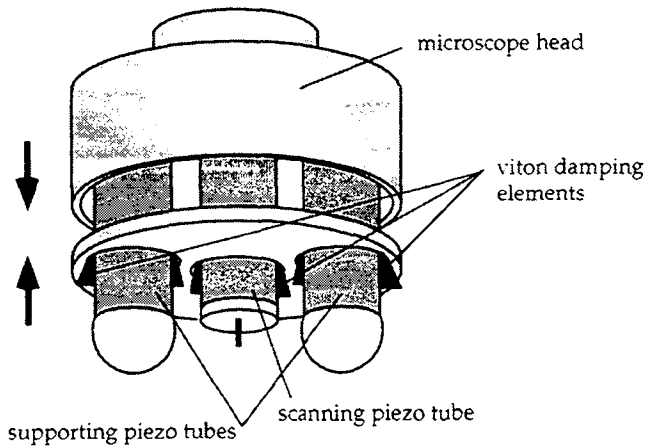
Fig. 2.1: The changes of the original concept of the manipulator included the possibility to decouple the Cu block with the sample holder from the support parts during STM measurements and the damping of vibrations transferred by the Cu braid to the sample.

Figure 2.1. By lowering the support tube, the Cu block with the sample holder can now be set down onto a viton damped stack and be decoupled from the rest of the manipulator during STM measurements. The main source of vibrational perturbations that rests is the mechanical connection to the cryostat via the braid. Following an idea of Bott et al. [38], a massive Cu block was attached to the braid in order to decrease the amplitudes of the transferred vibrations. The copper block itself rests vibrationally isolated by viton "U"s in the support tube. The braid is not directly attached to the Cu block, but is clamped by a piece of Teflon which is held by stainless steel screws in order to preserve cooling power. A vertical cut through the sample holder is shown in Figure 2.2. The sample is



**Fig. 2.2:** The sample is clamped between two sapphire rings for electrical isolation. This design permits effective cooling of the sample through the Cu sample holder, and isolates the sample thermally during flash annealing.

electrically isolated from the holder by thin rings of sapphire. Sapphire combines a high thermal conductivity at low temperatures ( $60 \text{ W}/(\text{cmK})$  @  $40 \text{ K}$ , facilitating an effective cooling of the sample) with a low conductivity at high temperatures ( $0.4 \text{ W}/(\text{cmK})$  @  $300 \text{ K}$ , permitting to heat only the sample during flash annealing). The use of the fragile sapphire rings renders clamping of the crystal to the holder with the help of screws less suitable. Instead, the upper ring is pressed by tungsten leaf springs [38], which solves as well the problem of sample loosening after several heating and cooling cycles, caused by different thermal expansion coefficients of the materials. To obtain compatibility with future Kerr-effect measurements, magnetic materials were avoided in the vicinity of the sample. Especially, the stainless steel screws on which the holder was originally mounted were replaced by screws made of titanium. The higher thermal conductivity of the titanium ( $22 \text{ W}/(\text{cmK})$  versus  $15 \text{ W}/(\text{cmK})$  @  $300 \text{ K}$ ) did not



**Fig. 2.3:** The STM-head with two of the outer piezos and the central single tube scanner. Small pieces of viton, clamped between the metal plate that can be screwed under the STM and the piezo tubes, efficiently damp vibrations of the piezo tubes.

significantly increase the attainable minimum temperature of the sample of about 25 K.

The design of the new microscope (Fig. 2.3) was motivated by an analysis of the vibrations of the beetle-type STM. It turned out that the vibrational modes with the lowest eigenfrequencies are those of a bending of the piezo tubes. By using tubes with a diameter of 6.4 mm (instead of 3.2 mm as in the original STM) the lowest eigenfrequency of the microscope could be increased from 2 kHz to 5.5 kHz [39]. A further improvement of the vibrational behavior was achieved by damping the vibrations of the piezo tubes by small pieces of viton clamped between the tubes and a metal plate that can be screwed under the head of the microscope (Fig. 2.4). Finally, the whole experiment was moved into the silent acoustic environment of a separate room and mounted on a commercial pneumatic suspension system [40]. These changes resulted in a vertical stability



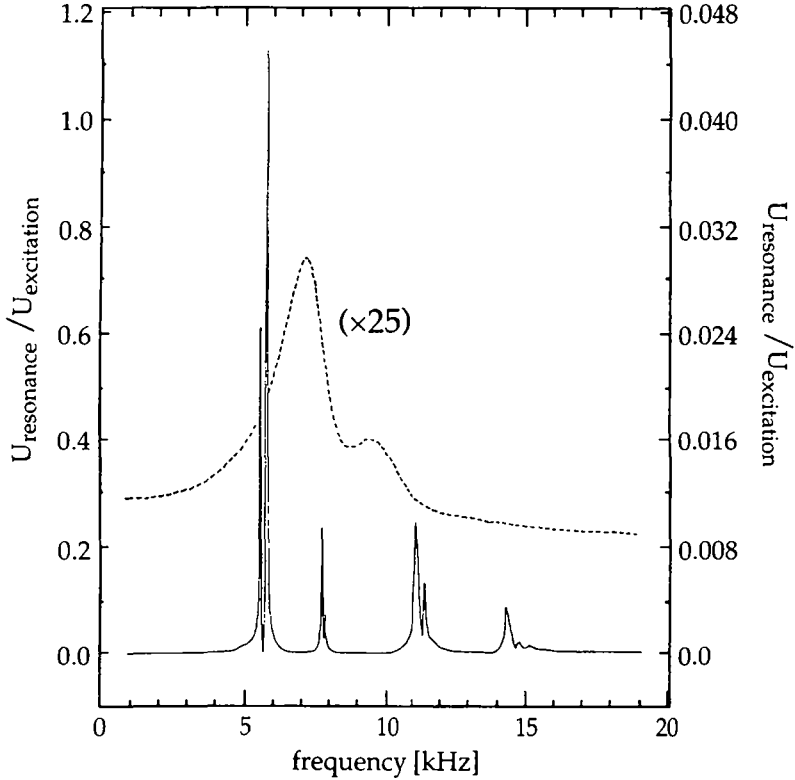


Fig. 2.4: The vibrational behavior of the outer piezo tubes of the STM with (dashed line, right scale) and without (full line, left scale) the viton damping elements. Note the different scales. The curves show the piezoelectric signal at an electrode during excitation of the opposite electrode, normalized to the input signal.

better than  $0.02 \text{ \AA}$ , permitting to resolve the atomic structure of close-packed metal surfaces (Fig. 2.5).

Three different electronic feed back control and data acquisition systems were used during the experiments: i) a home-built electronics that is similar to the original Besocke beetle-type control unit [41]; ii) a commercial STM control

unit developed by RHK Technology [42]; iii) a home-built electronics that was developed at the Fritz-Haber-Institut in Berlin [43] and at the University of Ulm [44]. The latter two control systems showed a much better signal to noise ratio than the first. Further, they are equipped with 16-bit A/D converters for data acquisition (the Besocke-type electronics allows only for data treatment with 8-bit precision). This permits a high resolution of the absolute topographic height with, simultaneously, a sufficiently large dynamic range to cope with typical experimental problems like inclined scanning planes or vertical drift. In the case of i), the problem of the smaller dynamic range is normally circumvented by applying a high pass filter with a cutoff frequency of 33 Hz to the data before representation and storage. The resulting image is a kind of differentiated signal and emphasizes the relative changes in height of neighboring points. The images recorded in this differential mode appear as if the surface was illuminated from the left.

All images shown in this thesis were obtained in the constant current mode, in which the distance between the sample and the tip of the STM is adjusted during the scanning motion to keep the tunneling current constant. Even though this mode is often called "topographic", the STM does of course not image the geometric positions of atoms or their nuclei, but reflects the electronic properties of the surface. In the first quantitative STM theory, Tersoff and Hamann showed that the lines of constant current followed by the STM tip correspond to contour plots of constant surface local density of states at the Fermi level [45, 46]. Even though this theory is too approximate to explain the enhanced corrugations found with atomically resolving STM-tips [47], it gives still a good idea of the interpretation of images obtained with larger barrier widths (i.e., for small tunneling currents and not too small tunneling bias). In most cases of the present thesis, however, especially when structures of monoatomic height are examined, we can interpret the STM images as revealing the actual topography of

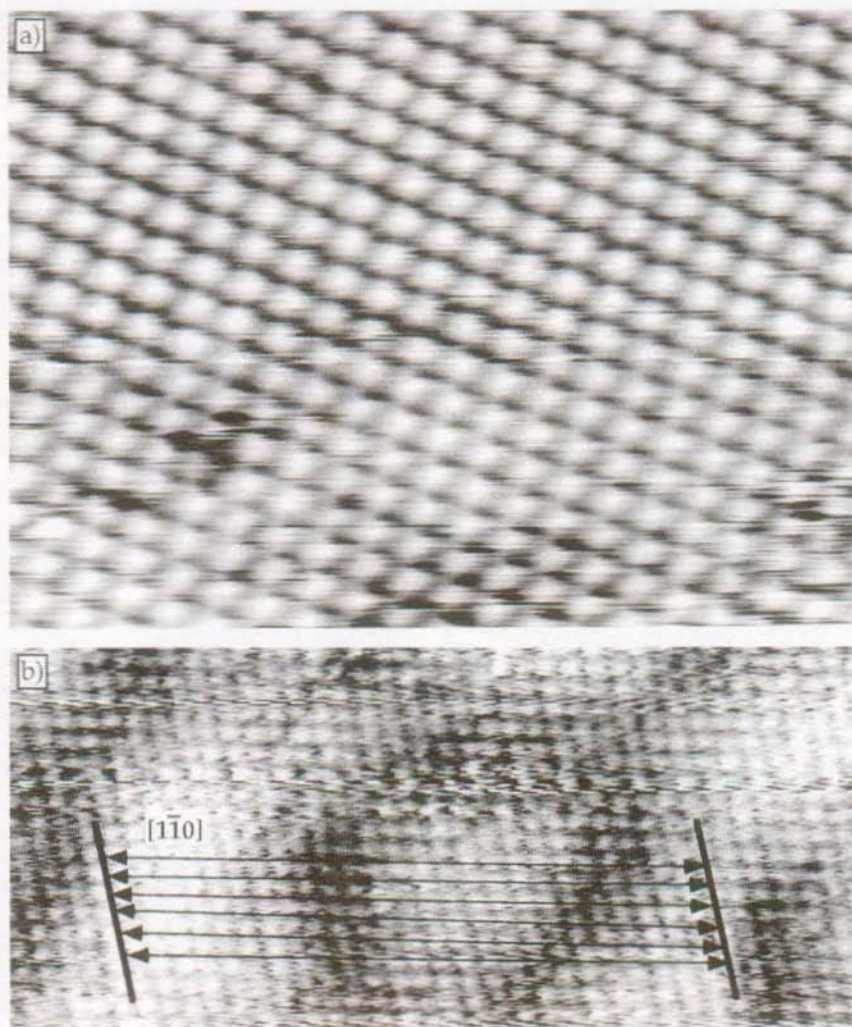


Fig. 2.5: Atomically resolved close-packed metal surfaces. The images are not compensated for lateral drift, which obscures the hexagonal symmetry. a) First monolayer of Ag on Pt(111). b) Third monolayer of Ag on Pt(111) with partial dislocations in the strain relief structure. The corrugations are about  $0.25 \text{ \AA}$ .

the surface. A case where we have to be careful with this simple approach is discussed in chapter 4.3. It is not evident that the imaging of partial dislocations as depression really corresponds to the actual positions of the atoms on bridge sites. There, the geometric interpretation of the STM image will be corroborated by EMT calculations.

The last part of this thesis deals with a cluster deposition experiment. To perform this experiment a secondary-ion cluster source was attached to the STM chamber. This source provides a steady flux of mass-selected and energy-filtered metal clusters under maintenance of UHV conditions at the place of the sample [48]. It consists of a primary ion source of CORDIS-type (cold reflex discharge ion source), the Ag target, an electrostatic lens system to extract the charged portion of the particles created in the sputter process, an energy filter (Bessel-Box), and finally a quadrupole mass filter. The source has three differential pumping stages to guarantee UHV conditions in the analysis chamber. A gate valve was mounted between this cluster source and the STM chamber to have the possibility of separating the two vacuum systems. The set-up of the combined experiment is shown in Figure 5.1.

The concept of combining two different apparatus rose several experimental problems. First, the differential pumping stages of the cluster source are equipped with mechanical pumps which had to be switched off during the STM measurements. This resulted in the necessity to bake out the source after every deposition. More problematic was the direct mechanic connection of the two apparatus making the pneumatic vibration damping system of the STM chamber ineffective. Even though the cluster source was installed on rubber damping elements, this resulted in a significantly reduced stability of the STM during the measurements.

During the cluster deposition experiments, Ar was used as a sputter gas in the cluster source. This ensured that rests of the sputter gas passing the

differential pumping stages belonged to the same atomic species as the atoms in the buffer layer. Ar was chosen for the buffer as it is the lightest of the rare-gases that forms multilayer films on the Pt(111) substrate at the lowest attainable temperature of 25 K [49]. The buffer layers were grown by flooding the whole STM chamber with the gas. The impact energy of the clusters, which left the quadrupole mass filter with a fixed kinetic energy of 95 eV, was regulated by applying a counterpotential to the sample.

### 3 Diffusion

The best method to learn about atomic diffusion processes would be to study the motion of the atoms directly. However, a generally non-negligible interaction of any probe with the studied system will restrict this approach to only a few singular cases. A rather direct technique to study atomic motion is field ion microscopy [50, 51]. But the normal way to apply this technique, too, is to take separate measurements at distinct times to exclude any influence of the high electric field on the atomic displacements. One has to use random-walk theory to infer information on the atomic motion between the moments of measurement. In the case of STM, the presence of the tip can substantially influence atomic motion, which has recently been shown for Pt(111) and Ag(110) [52, 53]. Our method to obtain knowledge of the diffusion processes has thus to make use of static properties of the system. We use the saturation density of the islands that form in the process of nucleation of atoms to stable clusters (and which are not affected by the STM measurement) to infer quantitative information on the activation energies and prefactors of the atomic diffusion processes. The link that connects island densities with diffusion parameters is nucleation theory.

#### 3.1 Nucleation theory

The physical idea behind nucleation theory is quite straightforward. Atoms deposited onto the substrate will diffuse around until two of them meet and form a cluster. This cluster can be stable or not, depending on the bonding strength between the atoms and temperature. For every system, however, it is possible to find a temperature below which such a dimer is stable. For the sake of

simplicity, we will discuss the case of stable dimers<sup>1</sup>. During the first phase of island growth, stable clusters form by encounter of two diffusing atoms. This stage is called "nucleation" regime. Upon further deposition, it becomes more likely for atoms to attach to existing stable islands than to find another diffusing atom and to form a new stable cluster. This stage characterizes the transition into the "growth" regime. At a certain coverage, no new stable clusters form anymore. All atoms that are deposited onto the surface find stable clusters within their diffusion length. The density of islands has reached its "saturation" value. It is obvious that this saturation density is related to the diffusivity of the atoms.

Mathematically, this relation is established by a set of coupled rate equations [12]. These equations describe the changes in the density of monomers and stable clusters within the framework of the mean-field approximation, which assumes a constant density of adatoms all over the surface of the substrate. The relatively complicated problem of solving the diffusion equation to obtain the exact local density of adatoms (which decreases near the edges of the clusters as they are sinks for the adatoms) is hidden in the capture numbers  $\sigma$  of the rate equations. In a simple form, for stable dimers and the neglect of island coalescence, these equations read

$$\frac{dn_1}{dt} = F - 2\sigma_1 D n_1^2 - \sigma_x D n_1 n_x - F(Ft - n_1) - 2F n_1, \quad (1)$$

$$\frac{dn_x}{dt} = \sigma_1 D n_1^2 + F n_1. \quad (2)$$

---

<sup>1</sup> There is no intrinsic difference in the physics of nucleation theory if the dimer is not stable. At a given temperature and for a given system, there is always a "critical" cluster which itself is not stable but will become stable upon incorporation of another atom. The discussion given above for monomers as critical clusters will remain the same. Further, "stable" refers to the time scale of the deposition. There is always a certain decay rate for clusters of any size. But if the impinging flux of diffusing atoms to the cluster is much higher than the rate of dissociation of atoms from the cluster, we can regard the cluster as stable.

Here,  $n_1$  and  $n_x$  signify the densities of adatoms and stable clusters,  $F$  is the impinging flux of deposited atoms onto the surface,  $\sigma_1$  and  $\sigma_x$  are the capture numbers of adatoms and stable clusters, and  $D = D_0 \exp(-E_m/kT)$  is the diffusivity of the adatoms. The second and third terms of Equation 1 describe the decrease of monomers due to encounter of two atoms and capture of one atom by a stable cluster, respectively. The first term in Equation 2 is the increase of stable clusters due to a meeting event of two atoms. The last terms in both equations describe deposition directly on top of atoms or stable islands. Equations of this kind can easily be generalized for larger clusters having a non-zero probability to decay (with  $i$  being the number of atoms in the largest cluster that can decay on the time scale of the experiment -the "critical" cluster- this leads to  $i+1$  coupled equations) or to include other phenomena like island coalescence.

The equations in their general form (i.e., without the restriction to the case of stable dimers) can be integrated under the assumption of local thermal equilibrium (detailed balance) between adatoms and the critical cluster. In the case of formation of 2D-islands, complete condensation of the deposited material, and no coalescence this leads to

$$n_x \propto \left(\frac{D}{F}\right)^{-\chi} \exp\left(\frac{E_i}{(i+2)kT}\right), \quad (3)$$

which is the normally given version of the main result of nucleation theory. Here,  $i$  and  $E_i$  denote the number of atoms in the critical cluster and its total binding energy, and  $\chi = i/(i+2)$ . Equation 3 predicts an Arrhenius behavior of the saturation island density. It can be used to determine the activation energy of terrace diffusion  $E_m$ . Three further aspects are important for the application of Equation 3.

1) With the size of the critical cluster  $i$  and the binding energy  $E_i$ , there are other free parameters in the theory. For an unequivocal determination of  $E_m$  one has thus to work in the low-temperature range where the dimer is stable and



thus  $i = 1$  and  $E_i = 0$ . There are three ways to determine up to which temperature the dimer is stable. First, direct inspection of the sizes of stable islands in the nucleation regime for a given temperature. Second, deposition at a temperature where dimers are surely stable and a subsequent annealing experiment. At a certain temperature, the island density will start to decrease and the mean island size will increase due to the onset of dimer and trimer decay (Ostwald ripening). Third, examination of the dependence of the saturation island density on deposition flux as predicted by Equation 3. The last method, however, can not be applied if we want put nucleation theory itself on the test as it relies on a prediction of this theory.

2) For the integration of the rate equations, steady state conditions are assumed. This assumption holds only for  $D/F > 10^5$ . If the diffusion of adatoms is too slow, a large supersaturation of adatoms is formed during the deposition, and a part of them is still left after having stopped the flux. The rate equations then have to be integrated under different starting conditions. This effect is called "post-nucleation" [54]. It decreases the island densities found in the experiment below the predictions of Equation 3.

3) If one is interested in the preexponential factors  $D_0$ , the proportional factor omitted in Eq. 3 has to be known. This factor is related to the capture numbers  $\sigma$ . There are different ways to treat these quantities. The simplest approach is to assume them as constants. A second possibility is to scale them like the diameters of the clusters as seen by a diffusing adatom. This geometric concept, however, neglects the requirement to approximate the solution of the diffusion problem mentioned above and is hence not well suited to a mean-field description. The best results are obtained within the lattice approximation, in which the diffusion equation is solved for a population of islands sitting on the sites of a lattice. This gives a proportional factor  $\eta(\theta, i)$  that varies slowly with coverage  $\theta$  and is  $\approx 0.2$  at a coverage of 10% [12].

A different method to treat the rate equations is to integrate them numerically. This can be done in a self-consistent way [55], which does not rely on further assumptions on the capture numbers and automatically includes effects like slow atomic diffusion. However, if applied with caution, the less exact way to determine the activation energies of terrace diffusion with Equation 3 gives nearly the same results as the mathematically demanding approach via a self-consistent solution of the rate equations.

#### Nucleation theory as a tool to determine interlayer diffusion

The information given in chapter 3.4 concerning the approach to use nucleation theory for the determination of the activation energy of interlayer diffusion is rather concise. Here, a more detailed description is given. The idea follows the concept of a critical island size for layer-by-layer growth put forward by Tersoff et al. [56].

We want to infer information on the interlayer diffusion from the nucleation of stable clusters on top of islands. The nucleation rate  $\omega$  per surface cell can generally be written (see e.g. Eq. (6) of Ref. [11]):

$$\omega = \gamma_i a^{-4} D n_1^{i+1}. \quad (4)$$

Here,  $n_1$  is the number of adatoms per surface cell of area  $a^2$ ,  $D = C_m a^2 v_m \exp(-E_m/kT)$  is the intralayer diffusivity (with  $v_m$  being the attempt frequency and  $C_m$  being a symmetry factor of order unity), and  $\gamma_i$  is a proportional factor which is of order unity in the case of stable dimers. In our case,  $n_1$  is a function of the position on the island. The adatom density on round shaped islands under impinging flux  $F$  of atoms from the gas phase can be calculated with the diffusion equation

$$\frac{dn_1}{dt} = D\nabla n_1 + a^2 F.$$

Under steady state  $dn_1/dt = 0$ . For radial symmetry (no angular dependence of  $n_1$ ) this leads to

$$-a^2 F = D \left( \frac{1}{r} \frac{\partial}{\partial r} \left( r \frac{\partial n_1}{\partial r} \right) \right),$$

which can be solved with the ansatz  $n_1 = B + Cr^2$ , yielding

$$n_1 = B - \frac{a^2 F}{4D} r^2. \quad (5)$$

The constant B is determined by the boundary condition for the adatom density at the island edge. Here, the quantity of interest, the diffusivity over island edges  $S$ , enters into the calculation. Under steady state, the flux onto the island equals the diffusion over the island edges:

$$\pi R^2 F = n_1(R) \frac{2\pi R}{a} S,$$

$R$  is the island radius and  $S = C_s v_s \exp(-E_s/kT)$  is the rate at which the atoms jump over the island edge per length  $a$  ( $a$  being the interatomic spacing and  $C_s$  is a symmetry factor of order unity). Solving for  $n_1(R)$  and substituting in Eq. 5 for  $r = R$  gives B as the density of adatoms in the center of the island. Finally, with the definition  $\alpha = S/(D/a^2) = Sa^2/D$ , we get the adatom density as a function of distance  $r$  from the island center (see Fig. 3.1):

$$n_1(r) = \frac{Fa^2}{4D} \left( R^2 + \frac{2a}{\alpha} R \right) - \frac{Fa^2}{4D} r^2. \quad (6)$$

Now, we can integrate the local nucleation rate per surface cell (Eq. 4) over the island area to get the total rate  $\Omega$  of nucleation on top of the island of radius  $R$ :

$$\Omega = \int_0^R [\omega(r) 2\pi r] dr$$

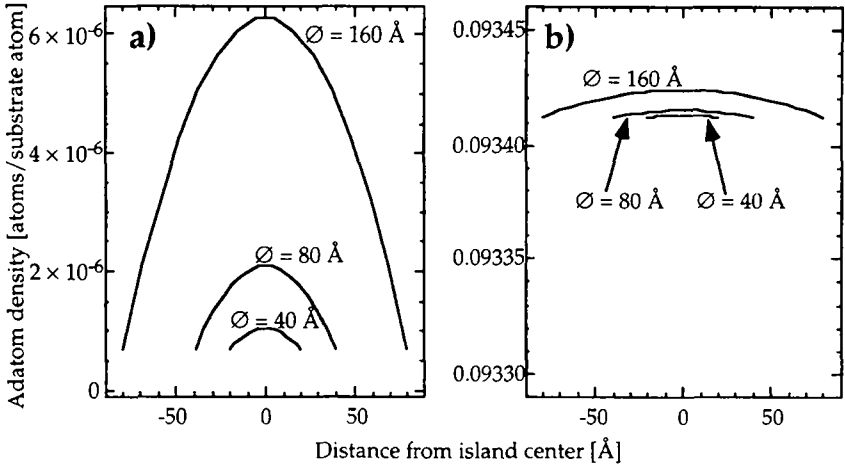


**Fig. 3.1:** Adatom densities on top of circular islands as a function of radial distance from the island center. The densities are calculated with equation 6 for a) Ag/Ag islands/Pt(111) and b) Ag/Ag islands/Ag(111), using  $Fa^2 = 1.1 \text{ ML/s}$ ,  $T = 70\text{K}$ , and interlayer and intralayer diffusivities as determined in chapter 3.4. The adatom density shows a strong dependence on the ratio of  $(E_s - E_m)/kT$ , becoming more uniform over the island for higher Schwoebel barriers and lower temperatures.

$$\begin{aligned}
 &= \frac{\pi\gamma_i D}{i+2} \left(\frac{F}{4D}\right)^{i+1} a^{2i-2} \left[ \left(R^2 + \frac{2a}{\alpha}R\right)^{i+2} - \left(\frac{2a}{\alpha}R\right)^{i+2} \right] \\
 &= \frac{\pi\gamma_i F^2}{48D} \left[ \left(R^2 + RL_a\right)^3 - (RL_a)^3 \right] \quad (* \text{ for } i = 1, L_a = 2a/\alpha).
 \end{aligned} \tag{7}$$

Equation 7 is the result found by Tersoff et al (Eq. 3 in [56]). We can now calculate the fraction  $f$  of islands with a nucleated second-monolayer cluster on top. This fraction varies with time as

$$\begin{aligned}
 \frac{df}{dt} &= \Omega(1-f) \\
 \Rightarrow f &= 1 - \exp\left[-\int_0^T \Omega(R(t)) dt\right].
 \end{aligned} \tag{8}$$

The integration of  $\Omega$  describes the increase of the sizes  $R$  of the previously grown islands during the second deposition of duration  $T$ . There are two limiting cases how to treat this integral.

First case: All the material of the second deposition impinges at the preexistent islands. No nucleation of new islands occurs between them. In this case, the original island density  $\rho$  stays constant. With  $N$  = island size [atoms],  $N_0$  the average size of the previously grown islands,  $T$  being the time of the second evaporation, and  $\theta_0$  and  $\theta_1$  the total coverages during first and second deposition, respectively, one has

$$\rho = \frac{\theta_0}{N_0} = \frac{\theta_0 + \theta_1 \frac{t}{T}}{N(t)} = \theta_0 \frac{1 + \frac{\theta_1}{\theta_0} \frac{t}{T}}{N(t)} \quad (* \text{ constant during second deposition})$$

$$\Rightarrow N(t) = N_0 \left( 1 + \frac{\theta_1}{\theta_0} \frac{t}{T} \right). \quad (9)$$

What we can measure in the experiment is the island radius  $R$  *after* the second deposition.

$$N(T) = \frac{\pi R^2}{a^2} = N_0 \left( 1 + \frac{\theta_1}{\theta_0} \right).$$

This can be used to substitute  $N_0$  (to which we do not have direct access in the experiment) in Equation 9. This leads to a formula  $N(t)$  of the size of an island as a function of time during the second evaporation that depends only on the total duration of the second deposition  $T$ , the total coverages of both depositions, and the measured radius of an island after this deposition  $R(T)$ . Using  $N(t) = \pi R(t)^2/a^2$ , we can solve for  $R(t)$  and finally get

$$R(t) = R(T) \sqrt{\frac{1 + \frac{\theta_1}{\theta_0} \frac{t}{T}}{1 + \frac{\theta_1}{\theta_0}}} \equiv R(T) \sqrt{\Delta}.$$

The nucleation rate  $\Omega$  becomes (with  $R(T) = R$ )

$$\Omega(t) = \frac{\pi\gamma_1 F^2}{48D} \left[ R^6 \sqrt{\Delta}^6 + 3R^5 L_a \sqrt{\Delta}^5 + 3R^4 L_a^2 \sqrt{\Delta}^4 \right] \quad (\text{for } i = 1 !),$$

and

$$\int_0^T \Omega(t) dt = T \frac{\theta_0 + \theta_1}{\theta_1} \frac{\pi\gamma_1 F^2}{48D} \left[ \left( \frac{R^6}{4} + \frac{6}{7} R^5 L_a + R^4 L_a^2 \right) - \right. \\ \left. - \left( \frac{R^6}{4} \left( \frac{1}{1 + \theta_1/\theta_0} \right)^4 + \frac{6}{7} R^5 L_a \left( \frac{1}{1 + \theta_1/\theta_0} \right)^{7/2} + R^4 L_a^2 \left( \frac{1}{1 + \theta_1/\theta_0} \right)^3 \right) \right]. \quad (10)$$

The result of Equation 10 can now be substituted in Eq. 8, which gives  $f(R)$ , the theoretic expectation of the fraction of covered islands after the second deposition as a function of island radius  $R$ . It should be emphasized that this result is valid for monomers as the critical cluster. For practical purposes, it is appropriate to use similar coverages for the first and second evaporation, which makes Eq. 10 a little nicer.

Second case: Only the material that lands directly on top of the preexistent islands increases their size during the second deposition. The material that is deposited between the islands nucleates there and does not contribute to the growth of the preexistent islands. The islands then grow like

$$\frac{dN}{dt} = Fa^2 N \quad \Rightarrow \quad N(t) = C \exp[Fa^2 t].$$

With  $T$  total time and  $\theta_1$  total coverage of the second deposition, the integration constant  $C$  can be determined. Again, what is measured is the radius of the With the relation between island size in atoms  $N(t)$  and island radius  $R(t)$ , the island radius in case 2 changes with time as

$$R(t) = R(T) \exp \left[ \frac{\theta_1}{2} \left( \frac{t}{T} - 1 \right) \right].$$

Nucleation rate and integral over time of this rate become (for  $i = 1$ )

$$\Omega(t) = \frac{\pi\gamma_1 F^2}{48D} \left[ R^6 e^{3\theta_1 \left(\frac{t}{T} - 1\right)} + 3R^5 L_a e^{(5/2)\theta_1 \left(\frac{t}{T} - 1\right)} + 3R^4 L_a^2 e^{2\theta_1 \left(\frac{t}{T} - 1\right)} \right],$$

$$\int_0^T \Omega(t) dt = \frac{\pi\gamma_1 F^2}{48D} \left[ \frac{R^6 T}{3\theta_1} (1 - e^{-3\theta_1}) + \frac{6R^5 L_a T}{5\theta_1} (1 - e^{-(5/2)\theta_1}) + \frac{3R^4 L_a^2 T}{2\theta_1} (1 - e^{-2\theta_1}) \right].$$

Again, this substituted in Equation 8 gives  $f(R)$  as the theoretic expectation of the probability of second monolayer nucleation on top of islands after the second deposition as a function of radius  $R$ .

### 3.2 The effect of strain on surface diffusion and nucleation

It is well established that the strain resulting from lattice mismatch in heteroepitaxy can have strong impact on the film morphology for thermodynamic reasons. The increase in strain energy with increasing film thickness often induces an instability in growth mode where two-dimensional growth is succeeded by three-dimensional growth above a critical thickness [57]. As a second effect the strain energy in general causes a pseudomorphic film at a certain thickness to change to disregistry, where part of the strain is relieved by the introduction of misfit dislocations (see e. g. Refs. [58, 59]).

In most cases thin films are grown far from equilibrium, hence their morphology is governed by kinetics rather than by thermodynamics. In the kinetic growth regime 3D growth results if nucleation and island growth on top of existing islands sets in prior to coalescence of these islands. This is determined, first, by the mean free path of a diffusing adatom on top of islands with respect to their size and form, i.e., whether and how often it visits the island edge, and second, by the rate for the adatom to descend the edge with respect to its visiting rate. In homoepitaxy, if no reconstruction is involved, these quantities are

independent of layer thickness. Therefore, the mean free path on top of an island and on the terrace below are identical. The latter determines the distance between islands and thus their maximum size before coalescence. Thus the islands grow never bigger than the mean free path of an adatom on top of them. Hence in homoepitaxy each adatom can reach the descending edge at least once, and therefore solely the activation barrier to descend the edge determines the morphology, whereas surface diffusion is less important.

In heteroepitaxy, as we will demonstrate in the present letter, this is in general quite different. Here, due to the inherent strain, surface diffusion can strongly alter from layer to layer and thus play the dominant role in determining the film morphology. Strain, if isotropic, is simply a variation of the in-plane lattice constant. It is shown that surface diffusion is rather sensitive to that parameter. If strain is anisotropic, i.e., if dislocations have formed, this is found to have a strong impact on adatom mobilities as well.

Our STM study of surface diffusion on strained Ag layers grown on Pt(111) reveals a drastic layer dependence of adatom mobilities manifested in layer-dependent island densities. The first Ag layer grows pseudomorphically, it is thus under an isotropic compressive strain of 4.3% [59]. This leads to a decrease of the Ag surface diffusion barrier to only 60 meV compared to 97 meV measured for self-diffusion on unstrained Ag(111). While an influence of strain on diffusion has been proposed some years ago in a theoretical study of Ga on GaAs(001) [60], there was no direct experimental evidence of this important effect. Calculations with effective-medium theory demonstrate that the decrease of the diffusion barrier on the pseudomorphic Ag monolayer is indeed due to strain; the electronic coupling from the substrate even weakens the effect. The calculations indicate that, in general, surface diffusion depends rather sensitively on compressive or tensile strain. Computations for a laterally strained Ag(111)-slab show that at moderate variations of the lattice parameter ( $\pm 2\%$ ) the diffusion



barrier scales nearly linearly with the nearest-neighbor distance, decreasing with compressive strain and increasing with tensile strain. This can be understood in an intuitive way. Lattice compression moves the adatom out so that it feels a less corrugated potential energy surface, while expansion has the inverse effect.

The experiments were performed with a variable-temperature STM (25K-800K) operating in UHV [61]. The Ag films on Pt(111) are prepared by deposition of Ag at 450 K and subsequent annealing to 800 K. The first monolayer grows pseudomorphically<sup>1</sup>, while the higher layers (2-3 ML) relax via the formation of periodic arrays of dislocations which transform into weakly modulated incommensurate films at larger thickness (4-20 ML) [59, 62, 63]. Very thick films (> 40 ML) show no modulation and have the Ag(111) interplanar lattice constant and symmetry as characterized by He-diffraction [62]. STM images revealed that both the pseudomorphic Ag layer on Pt(111) and the Ag(111) surface consisted of extended flat terraces which were free of dislocations. For the study of nucleation kinetics, submonolayer coverages have been deposited (flux  $1.1 \times 10^{-3}$  ML/s) subsequently onto these layers at various temperatures. Island densities are given in islands per Pt substrate atom, i.e., in ML. They were obtained on extended terraces and corrected for lateral drift.

The strong layer dependence of nucleation kinetics becomes evident from inspection of Figure 3.2. It shows nucleation on the substrate (a), the first (b), and second (c) Ag layer, as well as on a 50-ML-thick Ag layer which has adopted Ag(111) geometry (d). We will now briefly describe the concept of relating island densities to diffusion [13]. In all four cases nucleation of islands takes place at the time of deposition. The resulting island density is stationary under isothermal

---

<sup>1</sup> The experiments were performed on films with a nominal coverage of more than one monolayer. This assured that nucleation on top of the first monolayer could be studied without the influence of defects originating from alloy formation (see chapters 4.1 and 4.2) or from the dislocation network of the not yet completed first monolayer (see chapter 4.3).

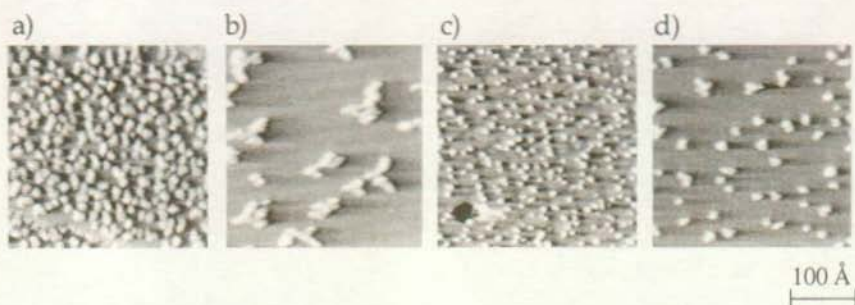


Fig. 3.2: STM images showing the nucleation of submonolayer coverages of Ag on Pt(111) (a), 1 ML Ag/Pt(111) (b), 2 ML Ag/Pt(111) (c), and on Ag(111) (d), respectively [(a) saturation island density  $N_X = 1.7 \times 10^{-2}$  islands per Pt(111) surface atom,  $\Theta = 0.12$  ML; (b)  $N_X = 6.6 \times 10^{-4}$ ,  $\Theta = 0.05$  ML; (c)  $N_X = 1.6 \times 10^{-2}$ ,  $\Theta = 0.03$  ML (note that the mean island size  $\Theta/N$  is 2, i.e., saturation is not yet reached for this case); (d)  $N_X = 3.8 \times 10^{-3}$ ,  $\Theta = 0.03$  ML; (a) and (b)  $T = 65$  K, (c) and (d)  $T = 60$  K; for all images, deposition flux  $R = 1.1 \times 10^{-3}$  MLs $^{-1}$ , size  $307 \times 307$  Å $^2$ ]. All STM images are taken isothermally to deposition.

conditions where it is imaged after deposition. At the beginning of deposition the density of nuclei steadily increases as a function of coverage (nucleation regime) until it becomes more probable that diffusing atoms attach to existing islands rather than create new ones. In this growth regime the island density stays nearly constant in a wide coverage range of  $\Theta = 0.05 - 0.20$  ML until it eventually decreases due to coalescence. Its maximum, the saturation island density, is determined by the ratio of the diffusivity to the deposition flux and therefore a measure for the adatom mobility. Except for Fig. c) all images in Fig. 3.2 show the surface after an island density close to saturation has formed, thus the mean island distance can be regarded as estimate for the mean free path of a diffusing adatom.

The island density shows an oscillatory behavior with layer thickness. It decreases by a factor of 26 when going from the Pt substrate to the pseudomorphic

first layer. The density then attains again the substrate value on the second layer. In this discommensurate layer the strain is relieved in a trigonal dislocation network which becomes visible as dark lines that include small triangles where they cross each other [59]. [Note that in Figure 3.2c the island density is not yet at saturation, which implies an even higher saturation density, i. e., lower mobility than suggested from the figure.] Nucleation on Ag(111) again leads to a slight decrease in island density (see Fig. 3.2d). Already from this set of STM images, which was depicted at 60 K - 65 K, it can be concluded that there is a strong influence of layer thickness on the adatom mobilities. However, care has to be taken when drawing conclusions on kinetic parameters from experimental data for a single temperature. As will be shown below, the strong layer dependent effect, manifest in Fig. 3.2, can even be reversed when going to higher temperatures.

In order to get quantitative insight in the diffusion and nucleation of Ag on these layers, we have measured the saturation island density as a function of temperature for the three cases of an isotropic substrate. The result is shown in Arrhenius representation in Fig. 3.3. For Ag on Pt(111) it has been demonstrated recently that application of mean-field nucleation theory [12] yields reliable information on the energy barrier and prefactor for surface diffusion ( $E_m = 157 \pm 10$  meV,  $v_0 = 1 \times 10^{13 \pm 0.4} \text{ s}^{-1}$ )<sup>1</sup> [13]. With these values the experimental island densities are exactly reproduced for all temperatures investigated, either upon integration of rate equations [13] or by kinetic Monte-Carlo simulations with these parameters (we applied the same Monte-Carlo code as in Ref. [15]). This gives us confidence in applying the same procedure also to the two other cases, i.e., Ag/1MLAg/Pt(111) and Ag/Ag(111). They equally show an Arrhenius

---

<sup>1</sup> A determination of  $E_m$  that takes into account the influence of small D/F values at low temperatures (see remark No 2 on page 26) finds 168 meV as a better value of the activation energy of terrace diffusion in this system.

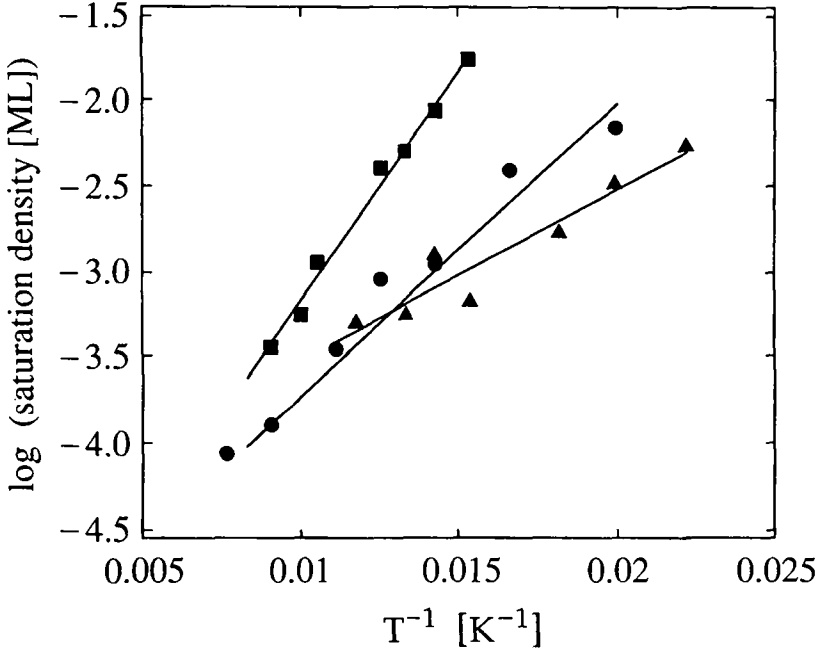


**Fig. 3.3:** Arrhenius plot of saturation island densities derived from STM for nucleation of Ag on Pt(111) (squares), on 1 ML Ag adsorbed on Pt(111) (triangles), and on Ag(111) (circles), respectively.

behavior of the saturation island density (see Fig. 3.3). A prerequisite for adequate application of nucleation theory is the knowledge of the critical cluster size ( $i$ ), and, respectively, that of a stable cluster ( $i+1$ ). (Clusters of size  $\leq i$  are unstable with respect to dissociation on the time scale of deposition.) Annealing experiments as well as the absence of sharp bends in  $\log_{10}N_x$  vs.  $(1/T)$  plots [13] show that dimers are stable (and immobile), i.e.,  $i = 1$ , in all three cases for the temperatures for which island densities are shown in Fig. 3.3. In this case the terrace diffusion can be directly deduced from the Arrhenius plot of saturation island densities without knowledge of dissociation energies [12].

For Ag diffusion on the isotropically strained first layer on Pt(111) we find  $E_m = 60 \pm 10$  meV and from the intersection of the line fit with the ordinate  $v_0 = 1 \times 10^{9 \pm 0.6} \text{ s}^{-1}$ . Compared to the substrate this is a rather low barrier, which explains the drastic decrease in island density at 65 K evident from Fig. 3.2b. For Ag self-diffusion on Ag(111) we obtain  $E_m = 97 \pm 10$  meV for the diffusion barrier with the corresponding attempt frequency  $v_0 = 2 \times 10^{11 \pm 0.5} \text{ s}^{-1}$  [1]. Therefore, at low T, the island density on the thick Ag(111) layer is in between that on the first layer and on the Pt substrate (see Fig. 3.2d). In the presence of dislocations (Fig. 3.2c), on the other hand, the island density is higher than on unstrained Ag(111), which means that a network of dislocations can confine diffusing adatoms and thereby strongly increase the island density, as discussed in more detail below. Note that with the barriers, also, a change in prefactor can go hand in hand. From Fig. 3.3 it is seen that this leads to crossing at  $T = 85$  K. From this temperature on, the ratio of island densities of the strained and unstrained case is inverted.

The most conspicuous and probably unexpected effect uncovered by the STM experiment is the low barrier for Ag diffusion on the pseudomorphic Ag layer compared to unstrained Ag(111). Two effects are conceivable to cause the observed lowering. It may either be due to the 4.3 % compressive strain or an effect of the electronic adlayer-substrate coupling. To decide which one is dominant we performed EMT calculations [64, 65]. For this purpose we considered a Ag atom adsorbed on a  $6 \times 6$  cell of a five-layer slab. The three upper layers are free to relax. The adatom is pulled over this surface, allowing its position to relax freely in a plane perpendicular to the vector of displacement, in order to find the minimum of total energy in course of the displacement. The

---

<sup>1</sup> The error for  $E_m$  is predominantly due to scatter of the data. The error of  $v_0$ , comes from the uncertainty of  $\eta(\Theta)$  in Eq. (2.15) of Ref. [12], [we assumed  $\eta(\Theta_{\text{saturation}}) = 0.20 \pm 0.04$  see Fig. 6c for  $i = 1$  in that reference] and from the error in slope, i.e., in  $E_m$ .

diffusion barrier  $E_m$  is then determined as the difference in total energy between the transition state (bridge site) and the preferred adsorption site (fcc-hollow).

The results of this calculation are summarized in comparison with experiment in Table 3.1. Regarding absolute values, it is seen that the EMT underestimates diffusion barriers, which is well known from other systems as, e.g., for Pt/Pt(111) [15]. However, the order of diffusion barriers is in accordance with experiment; the barrier is highest for Ag/Pt (80 meV), lower for Ag self-diffusion (67 meV), and substantially decreased for diffusion on the first pseudomorphic layer (50 meV). In order to distinguish between the effect of strain and the presence of the substrate, we calculated Ag diffusion on a Ag(111) slab which is under 4.3% compressive strain. (This has been achieved by reducing the lateral dimensions of the slab by 4.3% compared to the EMT equilibrium value for Ag; as above, the three uppermost layers were free to relax.) The result is that in the absence of electronic Ag-Pt coupling the effect is even more pronounced; the barrier is lowered to 41 meV. We can thus safely conclude that strain is the reason for the decrease in diffusion barrier on the first Ag layer, which is compressed into registry with the Pt(111) substrate.

|                   | $E_m$ (meV)<br><i>STM</i> | $E_m$ (meV)<br><i>EMT</i> | $E_b$ (eV)<br><i>EMT</i> |
|-------------------|---------------------------|---------------------------|--------------------------|
| Ag/Pt(111)        | $157 \pm 10^*$            | 80                        | 2.529                    |
| Ag/1MLAg/Pt(111)  | $60 \pm 10$               | 50                        | 2.374                    |
| Ag/Ag(111)        | $97 \pm 10$               | 67                        | 2.400                    |
| Ag/Ag(111) s=4.3% | —                         | 41                        | 2.380                    |

**Table 3.1:** Barriers for Ag surface diffusion as function of Ag layer thickness on Pt(111) as obtained from STM compared to calculations with EMT (s denotes compressive strain). \* See footnote on page 36.

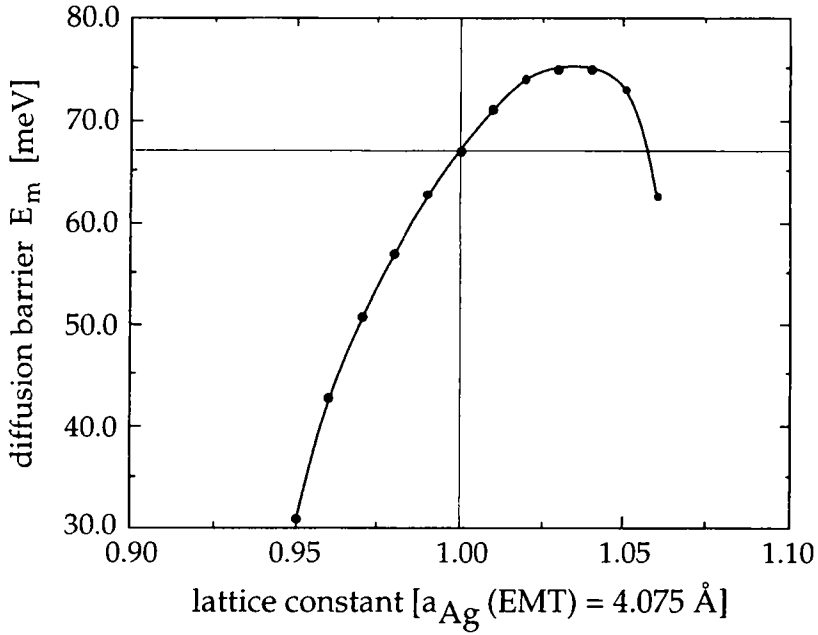


**Fig. 3.4:** Barrier for Ag self-diffusion on a Ag(111) slab as a function of tensile or compressive strain as calculated with EMT.

The general sensitivity of surface diffusion on compressive and tensile strain is illustrated in Fig. 3.4. It shows Ag diffusion barriers on differently strained Ag(111) slabs, again calculated with EMT. Small strain of  $\pm 2\%$  affects the diffusion barrier almost linearly; for tensile strain it is increased, for compressive strain decreased. The barrier has its maximum of 75 meV at 3.5% tensile strain. It drops upon further increase of the lattice constant. For compressive strain, migration becomes increasingly fast; the barrier attains half of the unstrained value at 4.8% compression. Looking at the binding energies for the adsorbed Ag atoms ( $E_b$ ), listed in Table 3.1, we estimate that the decrease of diffusion barrier due to compressive strain is mainly caused by a smaller binding energy in the hollow site. As expected, for tensile strain the binding energy in the hollow is increased, which leads to the increase in  $E_m$ . At high tensile strain ( $> 3.5\%$ ) the

transition state drastically decreases its energy, which explains the bending of the curve and the second decrease in  $E_m$ . This can be understood by the increasing softness of the layer with increasing lattice constant. Thus atoms in the bridge configuration, which corresponds to the transition state, can relax more efficiently.

For nucleation of Ag on a regular array of dislocations, we have seen in Fig. 3.2c that the island density is strongly increased with respect to the unstrained and the homogeneously strained case. Further, we find that only few of the nuclei form directly on dislocations. For increasing temperature, nucleation substantially differs from that on isotropic surfaces. The island density asymptotically approaches a minimum at 110 K, where one island forms per unit cell of the dislocation network. Fig. 3.5 (a) and (b) show nucleation at 90 K and 110 K with an average of 1.3 and 1.1 islands per superstructure unit cell. Note that, again, only very few of the islands form on dislocations. The majority sit on the hexagons of the unit cell which are pseudomorphic with fcc stacking [59, 63]. From this we conclude that the dislocations constitute a rather effective repulsive barrier for adatoms to cross, which confines them to the pseudomorphic domains. At higher temperatures this confinement artificially increases the island density even if diffusion on the homogeneously strained parts of the surface may be fast. A similar effect has recently been observed for Ni nucleation on the dislocation network of Ni on Ru(0001) [66].

This shows that the influence of dislocations on diffusion and nucleation is substantial; in our particular case they are repulsive, even though they have a lower density and thus an increased diffusion barrier. There are a variety of possible ways for dislocations to influence diffusion and nucleation. It has been shown for Ni, Fe, and Co on Au(111) [67] that the elbows of the herring bone reconstruction can act as traps. In contrast, recent results for Al on this surface indicate that this is not the general rule [68]. Whether a dislocation acts as sink or



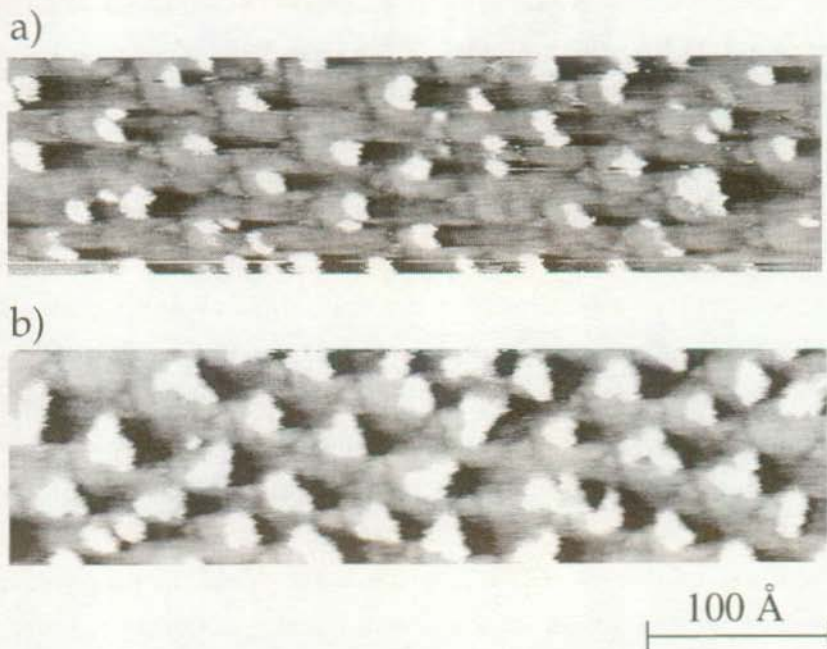


Fig. 3.5: STM images showing the influence of dislocations on nucleation of Ag on 2 ML Ag/Pt(111), (a)  $T = 90$  K,  $N_x = 1.3$  per unit cell of superstructure,  $\Theta = 0.03$  ML, (b)  $T = 110$  K,  $N_x = 1.1$  per unit cell of superstructure,  $\Theta = 0.12$  ML (image size  $450 \times 120 \text{ \AA}^2$ ).

repulsive wall for diffusing adatoms depends on both the binding energy and the diffusion barrier when crossing the dislocation and has to be investigated for the particular case. For Pt/Pt(111), e.g., the barrier between adjacent fcc sites basically stays constant whereas the total energy increases upon crossing a dislocation [69]. Even if the change in total energy is small it is feasible to lead to drastic changes in diffusivity because atoms have to make several successive jumps in unfavorable directions to overcome a dislocation. No matter how dislocations affect diffusion and thereby nucleation, there is no question as to their strong

influence, as it has been observed, to our knowledge, in every case investigated so far.

While we have demonstrated the impact of misfit strain on surface diffusion and nucleation for a particular model system, its implications for heteroepitaxial growth in the kinetic regime are of general significance. It is generally true that the adatom mobility on an isotropically strained layer will be modified relative to the strain-free surface. To the extent that the kinetics is simply dominated by strain effects<sup>1</sup>, this work indicates that compressive strain will decrease and tensile strain will increase diffusion barriers. Modified adatom mobilities and thus altered nucleation densities on successive layers due to strain can substantially effect the growth morphology. An enhanced adatom mobility on top of a certain layer, in general, promotes its smoother growth while the inverse effect will drive the system towards rough three-dimensional growth. These effects might be used to shape the growth mode of an heteroepitaxial system on pure kinetic grounds. The nucleation rate is also critically influenced through strain-induced formation of a dislocation network. These dislocations can act as heterogeneous nucleation centers or as repulsive barriers. Their influence is not limited to heteroepitaxy. Even in homoepitaxy, for surfaces that have intrinsic tensile stress and thus reconstruct, the presence of dislocations can influence the growth morphology. For Pt/Pt(111) the large increase of the nucleation rate due to the dislocation confinement is thought to give rise to an anomalous, perfect 2D growth at 650 K [70]. More than 150 undamped oscillations are seen in the specular He intensity, where a much faster decay of oscillations was expected without the reconstruction. The concept of layer-dependent adatom mobilities and island densities caused by strain seems to be of general validity and

---

<sup>1</sup> Without detailed calculations, such as those presented here, it is not possible to predict with confidence if a given system is dominated by strain or by electronic coupling.

constitutes, in addition to the barrier for interlayer diffusion, an essential ingredient for the kinetic modeling of film growth.

### 3.3 Anisotropic corner diffusion as origin for dendritic growth on hexagonal substrates

In the "classical" diffusion-limited aggregation (DLA) computer models, clusters are formed as randomly diffusing particles stick irreversibly to the perimeter of a growing aggregate [17, 18]. These models always produce *randomly ramified* aggregates, no matter whether they are carried out on a lattice or not (off-lattice DLA) [19]. Nonequilibrium aggregation processes in nature, however, quite often result in *dendritic* patterns which are characterized by preferred growth directions [71, 72]. Despite a considerable theoretical effort, the relationship between ordered and randomly ramified patterns is not yet solved [73, 74]. Both objects have a fractal dimension close to 1.7 [75, 76], but their different shape is evident for the unaided eye (compare e.g. Figs. 3.9A and 3.9C). It is generally accepted that the key to dendritic growth is anisotropy [77]. This can either be linked to the symmetry of the aggregating particles themselves, which is then amplified to the overall pattern shape as the aggregate grows (a well known example for this is the snowflake), or it can be due to the symmetry of the underlying substrate. Examples for this latter case are given in Figure 3.6, where we observe dendritic growth for two-dimensional metal aggregation on three hexagonal close-packed substrates.

In order to reproduce dendritic structures basically two approaches have been followed to modify the hit and stick mechanism in DLA models. One is the introduction of curvature dependent sticking probabilities [78] and the second noise reduction, where atoms are only attached if the approached site has been visited  $m-1$  times before [79]. Both mechanisms are, however, irrelevant for low

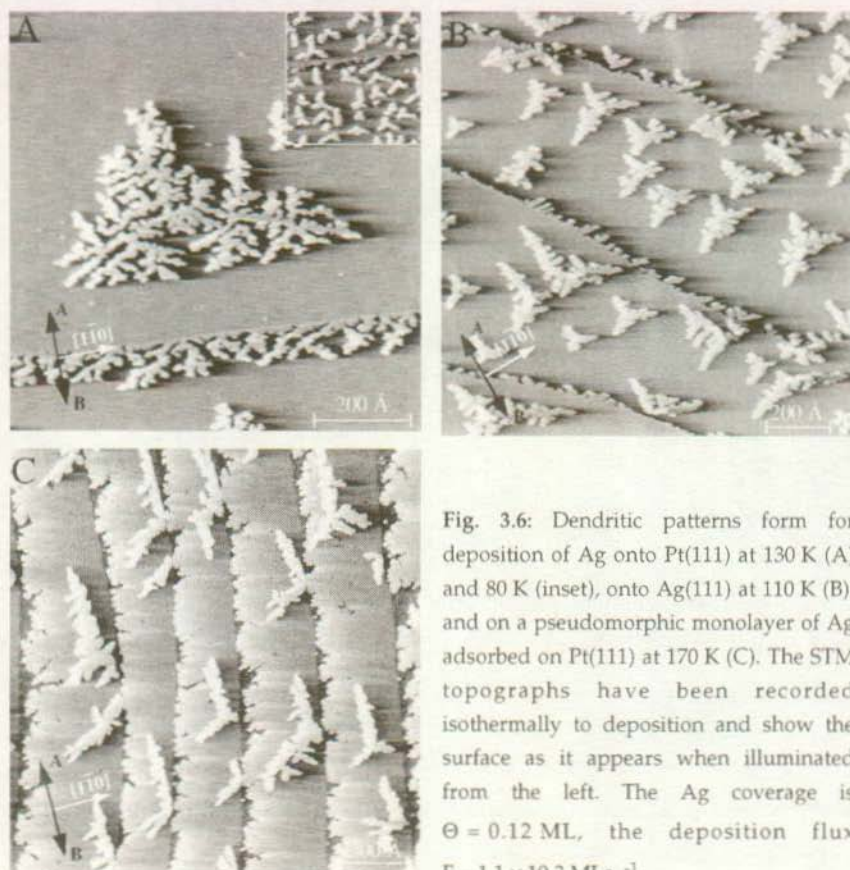


Fig. 3.6: Dendritic patterns form for deposition of Ag onto Pt(111) at 130 K (A) and 80 K (inset), onto Ag(111) at 110 K (B), and on a pseudomorphic monolayer of Ag adsorbed on Pt(111) at 170 K (C). The STM topographs have been recorded isothermally to deposition and show the surface as it appears when illuminated from the left. The Ag coverage is  $\Theta = 0.12$  ML, the deposition flux  $F = 1.1 \times 10^3$  MLs $^{-1}$ .

temperature metal epitaxy, since there the sticking probability is 1 and independent of curvature.

Already in the first metal deposition experiments studied with the STM (at 300 K), ramified growth and irregular island shapes were reported [80-82]. In particular, the Au aggregates on Ru(0001) have been considered as an example for classical DLA clusters because of their fractal dimension [82]. However, it had been realized later that their branch width (100 - 200 Å) points to a considerable

amount of edge diffusion [20, 83-85]. Similarly, the first results reported for lower temperature, showing ramified islands for homoepitaxy on Pt(111), were also interpreted as the physical realization of the hit and stick mechanism [14].

The first time dendrites have been reported, and their distinction to randomly ramified aggregates was made clear, was for the aggregation of Ag on Pt(111) [7, 76]. These results have inspired kinetic Monte-Carlo simulations which reproduced the randomly ramified islands obtained in the experiment at very low deposition flux [86]. Since they assume a hit and stick mechanism and neglect the specific substrate symmetry (which both holds for aggregation of much bigger clusters [87]) they were unable to simulate dendritic growth. This also holds for those models that study metal nucleation on a square lattice [27, 28, 55]. On the other hand, simulations performed on a hexagonal lattice either focus on the shape of compact islands on Pt [15, 88], or they do not distinguish between the two types of close-packed steps present on a hexagonal substrate [83, 89]. There are close packed {111}-facets and more open {100}-facets (see model in Fig. 3.7), which have been called B- and A-steps, respectively [90].

Thus, to date, a realistic description of the atomic processes leading to dendritic growth in metal aggregation on hexagonal substrates was lacking. We will present here a microscopic model explaining dendrite formation and discuss the importance of the different relaxation processes at the island edge and their influence on the aggregate shape.

Patterns formed by the aggregation of Ag on three hexagonal close-packed metal surfaces, i.e., the (111) surfaces of Pt, Ag, and one Ag monolayer pseudomorphically adsorbed on Pt(111) [59], all have in common a clear dendritic shape (Fig. 3.6). The variable temperature STM images (for experimental setup see e.g. ref. [61]) show that their branches preferentially grow into three directions, which are rotated by  $120^\circ$  with respect to each other. They are the crystallographic  $\langle \bar{1}\bar{1}2 \rangle$ -directions which are perpendicular to A-steps, one of them has been

labeled A. For the first case of Ag/Pt(111) (Fig. 3.6A) the trigonal symmetry of the aggregate is best seen from its triangular envelope, but also the longest central branches clearly point into the preferred growth directions. Notice also that the material attached to the straight substrate step in the lower part of the image does not grow perpendicular to the edge (which would be the B-direction since this step is a {111}-facet, i.e., of B-type) but instead in two of the A-directions forming angles of  $\pm 30^\circ$  with respect to the step. At 80 K islands are too small to branch more than once and the growth anisotropy leads to equally oriented Y's (inset Fig. 3.6A). For Ag/Ag(111) (Fig. 3.6B) the preferred growth in three directions is clearly seen from the central branches of the aggregates. The trigonal symmetry of the aggregates on one pseudomorphic Ag layer is even more pronounced. Their shape resembles very much that of needle crystals, which are the extreme case of anisotropic growth [91]. These examples strongly suggest that dendritic growth is common for low temperature metal aggregation on hexagonal close-packed metal surfaces. In fact also Pt islands formed at low T have dendritic shapes with preferential growth in A-direction [21].

To analyze the atomic process responsible for the formation of dendrites on hexagonal surfaces, we will distinguish between two diffusion processes that can take place at the island edge. Depending on whether an adatom starts from a site which is laterally *two-* or *one-fold* coordinated to the island, i.e., whether the initial site is an edge or a corner, we will call its displacement *edge-* or *corner-*diffusion, respectively<sup>1</sup>. For corner diffusion the final coordination can be 1 or 2. For edge diffusion the final coordination is 2. The case where an edge atom (2-fold coordinated) goes to a corner (1-fold) becomes important at higher temperatures, and should be treated separately.

---

<sup>1</sup> This important difference has first been realized by Zhang et al. in Ref. [89].

It turns out that this distinction is rather useful since these processes have quite different effects on the aggregate's shape. Edge diffusion leads to a thickening of the aggregates' branches [20, 83-85]. Closer inspection of the dendrites (Fig. 3.6) indeed reveals that the branches become thicker in going from images (A) to (C) (notice the different scale). From the narrow branches for Ag on Pt(111) ( $2 \pm 1$  atoms wide) in Fig. 3.6A we can deduce that edge diffusion is practically frozen in (at 130 K and the applied deposition flux) [20]. Edge diffusion is active for Ag/Ag(111) at 110 K since branches are  $8 \pm 1.5$  atoms wide (Fig. 3.6B) [20]. It is even more involved in the case of Ag/1MLAg/Pt(111) leading to  $18 \pm 3$  atoms wide branches (Fig. 3.6C). From the fact that dendritic growth occurs in all examples shown in Figure 3.6, independent from the amount to which edge diffusion is involved, we can argue that it is very unlikely to be the origin of dendritic growth.

In order to get insight into the relaxation processes at the aggregate perimeter we have calculated diffusion barriers with effective-medium theory (EMT) [65]. The results show that for all three cases where we found dendritic growth in the STM experiment, corner diffusion to an A-step has a much lower barrier than displacement from a corner to a B-step (Fig. 3.7 and Table 3.2). This asymmetry can be rationalized from simple geometric reasons. From inspection of the model (Fig. 3.7) it becomes evident that displacement from a corner to an A-step can be done via an hcp-hollow site without losing the coordination to the heptamer, whereas for diffusion towards a B-step the hcp-site is situated too close towards the island. Thus the adatom has to walk almost over an on-top site, which is much more costly in energy.

For some systems like Pt(111) [15] and Au(111) homoepitaxy, the corner asymmetry is less pronounced in the EMT-calculations and the direction is even inverted, i.e., displacement to B-steps is slightly preferred (Pt:  $E_{Ac}/E_{Bc} = 212 \text{ meV}/173 \text{ meV}$ , Au:  $E_{Ac}/E_{Bc} = 146 \text{ meV}/101 \text{ meV}$ ). This inversion is due to

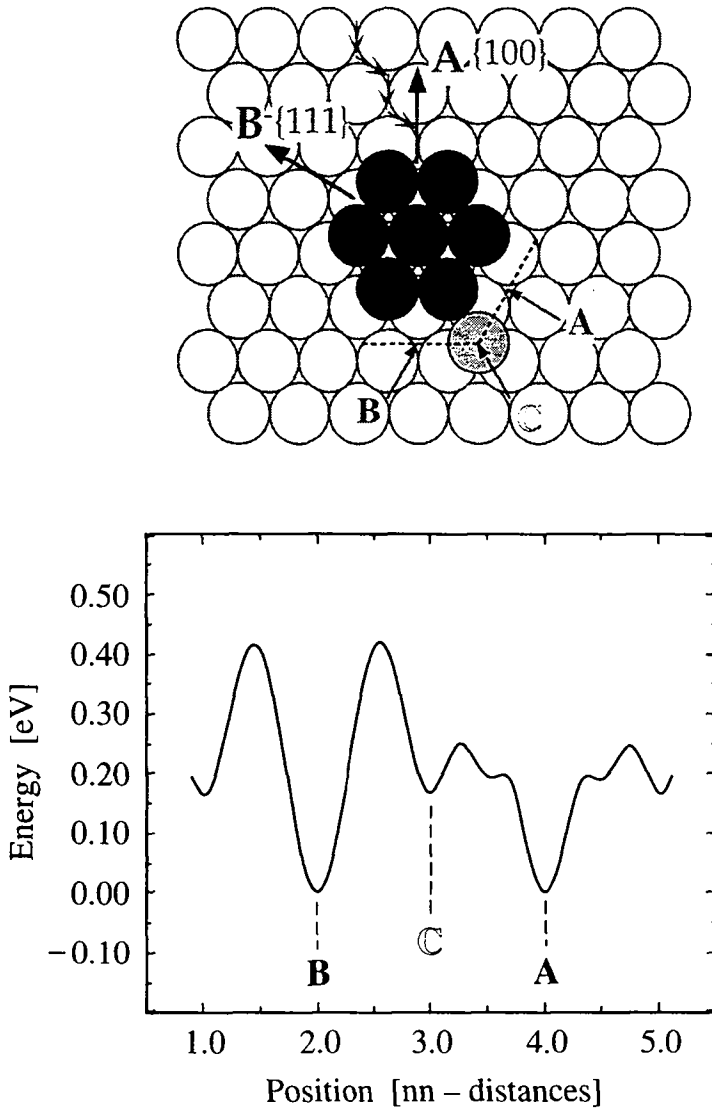


**Fig. 3.7:** Difference in total energy of a Ag adatom diffusing around a Ag heptamer on Pt(111) as calculated with EMT (A- and B-directions are indicated in the ball model). The diffusion processes with the lowest barriers evidently are that from a corner (C) and the hcp-site close to it to an A-step.



|                               | $E_m$ [meV]         | $E_m$ [meV] | $E_{Ac}/E_{Bc}$ | $E_{Ae}/E_{Be}$ | $E_{Aec}/E_{Bec}$ |
|-------------------------------|---------------------|-------------|-----------------|-----------------|-------------------|
| Ag diffusion<br>on substrate: | STM                 | EMT         | EMT             | EMT             | EMT               |
| Pt(111)                       | 157±10 <sup>1</sup> | 80          | 80/248          | 187/389         | 244/415           |
| Ag(111)                       | 97±10               | 67          | 73/139          | 222/300         | 260/330           |
| 1MLAg/Pt(111)                 | 60±10               | 50          | 39/165          | 167/354         | 231/356           |
|                               |                     | $E_m$ [meV] | $E_{Ac}/E_{Bc}$ |                 |                   |
|                               |                     | KMC         | KMC             |                 |                   |
| Pt(111)                       |                     | 160         | 160/500         |                 |                   |
|                               |                     | 120**       | 160/320*        |                 |                   |

**Table 3.2:** Energy barriers for the most relevant atomic diffusion processes involved in metal aggregation on hexagonal substrates for the systems studied in Fig. 3.6 ( $E_m$  terrace diffusion,  $E_{Ac}$  corner to A-step,  $E_{Bc}$  corner to B-step,  $E_{Ae}$  and  $E_{Be}$  A- and B-edge diffusion,  $E_{Aec}$  and  $E_{Bec}$  denote diffusion from A- and B-edges to corners). The experimental values for terrace diffusion have been obtained by the analysis of the saturation island density as a function of  $T$  at a critical cluster size of 1 [13]. (\* in Fig. 3.9D,  $E_{Bc}$  has been lowered; \*\*  $E_m$  has been lowered for 130 K in order to account for dimer instability at this temperature, see text.)

tensile stress inherent in these systems leading to a strong contraction at the island edge, which facilitates the diffusion from corner to B-steps. Easier diffusion to B-steps is similarly expected for adsorbates with significantly smaller lattice constant than the substrate.

It is therefore important to notice that there is a second anisotropy which generally holds for hexagonal close packed surfaces. An atom that diffuses towards an A-step close to a corner does this via the hcp-site located between the two fcc-sites at the corner and the A-step (ball model Fig. 3.7). Already at this point, it feels the two-fold coordination at the step and has a much lower barrier

<sup>1</sup> See remark on page 36

to go there than to diffuse to the corner site (see asymmetry in activation energy around the hcp-site and the flashes indicating an approaching atom in Fig. 3.7). On a B-step, the decision whether the atom goes to the corner or the step is made much earlier so that it is not guided to the step.

For Ag aggregation, both these asymmetries give a significant preference in populating A-steps. It is important to note that both diffusion processes, i.e., corner to A-step and that from the hcp-site to an A-step, have an activation energy comparable to, or even below, that obtained for terrace diffusion. Therefore, relaxation towards A-steps is active as soon as nucleation and aggregation set in, and the classical hit and stick DLA cluster do not form. The barriers for the more difficult corner process (corner-to-B step), and those for edge diffusion, as well as to escape from an edge to a corner (see Table 3.2), are significantly higher, which implies that these processes will be completely frozen in at low temperatures.

Let us now see how this specific preference for A-steps decides on the shape of the growing aggregate in a growth scenario (Fig. 3.8A). For symmetry reasons we start from a tetramer which is bound by two A- and B-steps. Atoms impinging at corners adjacent to an A-step, as well as those approaching the A-step at the two neighboring hcp-sites, will end up at the A-step, which significantly increases the probability of attachment there. Once the atoms are at A-steps, they form a protruding tip (e.g. atom 1 in Fig. 3.8A) and thus have a slightly higher capture rate than straight steps (this is known as "tip-effect" or Mullins Sekerka instability [18, 92]). Atoms arriving at such an atomic "tip", can diffuse back and forth between the two corner sites but they cannot escape from there, since this would be diffusion to the adjacent B-steps, which is frozen in. If a second atom arrives at the respective free corner, a new A-step is formed, which then again collects very effectively diffusing atoms and growth in the A-direction proceeds. If the atom arrives such that a linear chain in the close packed direction would be formed

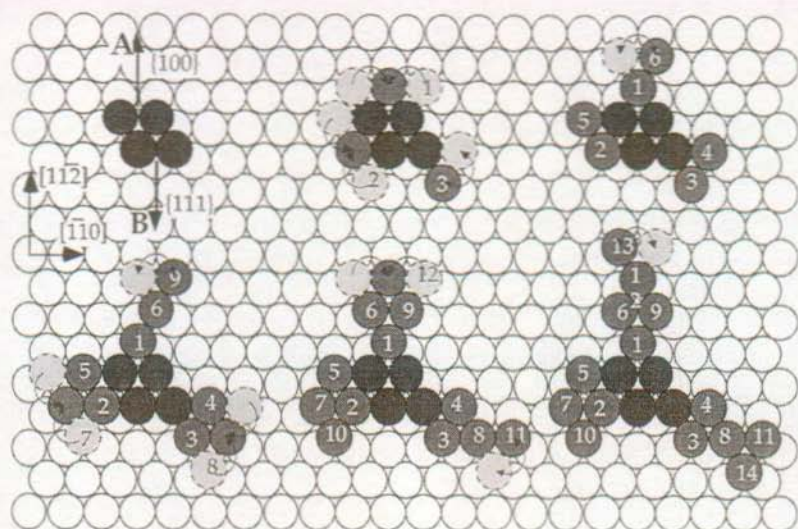
(atoms 1, 6, and 9), the EMT calculations suggest (Fig. 3.8B) that these chains can relax with a low energy barrier to a more compact form which also ends with an A-step.

Therefore, growth of "Y"s occurs as A-steps effectively capture atoms, which then form tips that are traps for attaching atoms due to the frozen corner-to-B diffusion. Atoms attached there thus stay until a partner arrives to form a dimer which provides new A-steps. Direct attachment to B-steps leads to statistical deviations from this behavior. However, it also creates new A-steps which can be the origin for a new branch in the preferred A-directions.

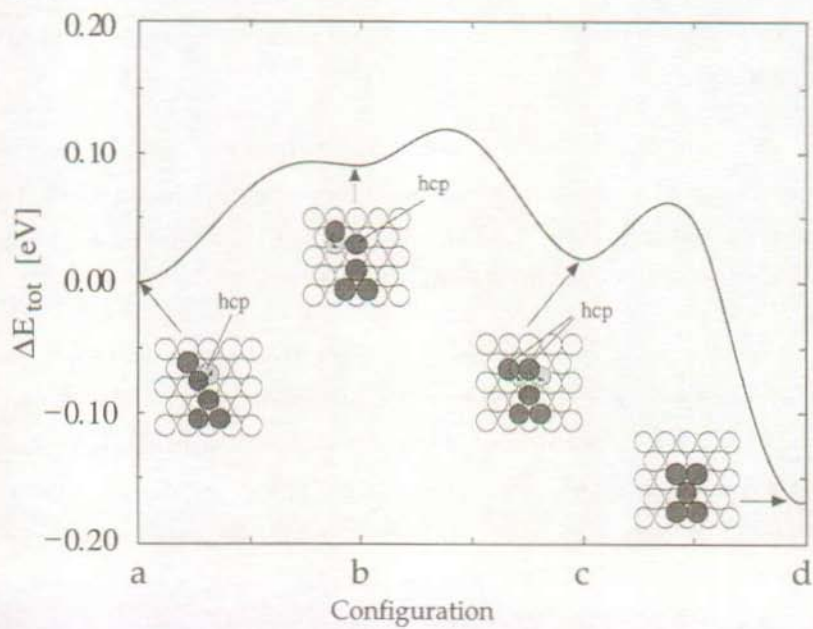
To test these ideas we performed kinetic Monte-Carlo (KMC) simulations [15] for Ag/Pt(111) on a hexagonal lattice where we distinguish between A- and B-directions. Activation energies on surfaces are often underestimated by the EMT. However, the EMT generally gives a good idea on the energetic hierarchy of different diffusion processes. Therefore, as a first input for the KMC we use the EMT activation energies scaled by a common factor of 2, since then the barrier for terrace diffusion equals the experimental value of  $E_m = 160$  meV [13]. All prefactors have been set to the experimental value for terrace diffusion of  $1 \times 10^{13} \text{ s}^{-1}$  [13]. Using  $E_m = 160$  meV in a KMC simulation precisely reproduces the experimental island densities at temperatures up to 110 K, where dimers are stable and immobile. In our simulations done at 130 K we used  $E_m = 120$  meV as an effective barrier for terrace diffusion which then also accounts for the dimer

**Fig. 3.8 (next page):** Scenario showing how dendritic "Y"s with branches in A-direction grow on a hexagonal surface if corner diffusion towards A-steps is active while that towards B-steps is frozen in (A). Movements from the possible initial sites of impingement (light gray) leading to the same final adsorption site have been marked by bent arrows. The energy diagram in B shows the instability of atomic chains via a collective relaxation of both atoms.

(A)



(B)



instability or mobility. This way, we again get the experimental island density at 130 K and thus the correct lateral impinging rate of atoms to each island.

The KMC simulations nicely illustrate the influence of the different processes on the island shape (Fig. 3.9). The hit and stick case, where terrace diffusion and jump down from island tops are the only atomic displacements allowed, gives the classical randomly ramified DLA fractals where the substrate symmetry is not visible in the overall cluster shape (Fig. 3.9A). Turning on corner diffusion towards A-steps induces a marked change towards trigonal symmetry with branches predominantly growing into A-direction (Fig. 3.9B). However, the aggregates form monoatomic chains along  $\langle 1\bar{1}0 \rangle$  and the Y-shaped islands experimentally observed at 80 K cannot be reproduced (see inset Fig. 3.9B). If we introduce further the collective relaxation of these chains, we can improve this. The scaled EMT barrier of  $E_{\text{coll}} = 240$  meV (see Fig. 3.8B) is too high for the process to happen sufficiently frequently at 80 K; but choosing  $E_{\text{coll}} = 160$  meV, we get a strikingly good agreement with the experimental island shapes at 130 K and 80 K (Fig. 3.9C and inset).

We want to point out that the important time scale for all relaxation processes at the island edge is the lateral impinging rate of diffusing atoms. The observed island shapes at 80 K set an upper limit of 160 meV for the barriers of the corner-to-A process and the collective relaxation of the  $\langle 1\bar{1}0 \rangle$ -chains.

Speeding up these processes by reducing their energy barriers in the simulations would not significantly change the morphology of the obtained islands (Fig. 3.9, B-D). Similarly, we find that the experimentally observed island shapes at 130 K (Fig. 3.6A) set a lower limit of 320 meV for the barrier of the corner-to-B process. The scaled EMT barrier of 500 meV freezes this process completely even at 130 K. In Fig. 3.9D, we show the result of a simulation using  $E_{\text{Bc}} = 320$  meV at 130 K. This gives an even better agreement with the experimentally observed islands. There is still strongly preferred growth

perpendicular to the A-steps, however, now the simulated islands bear some of the randomness characteristic of the experiment with occasional growth of the branches perpendicular to B-steps.

In general, the growth direction of the aggregate's branches is largely determined by corner diffusion. It decides whether randomly ramified or dendritic patterns will evolve, and determines the orientation of the latter. The branch width, on the other hand, is determined by edge diffusion, which has much less influence on their growth direction. Finally, compact islands can only be formed if atoms can leave the two-fold coordination at edges and diffuse around corners, a process which has a slightly higher barrier than edge diffusion (see Table 3.2).

In conclusion, we presented STM experiments at low temperature showing dendritic growth for diffusion limited metal aggregation on three different hexagonal surfaces. The mechanism giving rise to the trigonal symmetry has been identified using EMT energy calculations and kinetic Monte-Carlo simulations. The key process is the preferential diffusion of atoms from one-fold corner sites towards A-steps. In addition to this anisotropy in corner diffusion there is a preferred diffusion towards A-steps for atoms approaching an island. Both processes significantly increase the population of these steps and thereby promote trigonal dendritic growth.

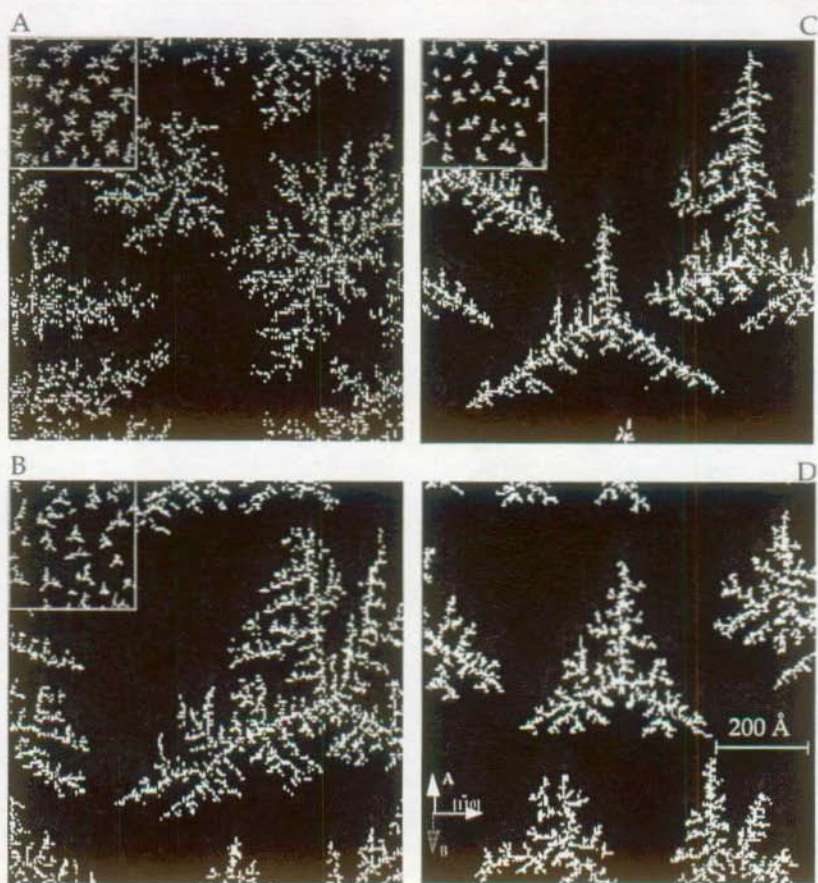


Fig. 3.9: KMC simulations of the STM experiments for Ag/Pt(111). As in Fig. 3.6A, the scale is the same for figures and insets, they correspond to growth temperatures of 130 K and 80 K, respectively. Coverages and deposition rates are as in the experiment. For hit and stick, classical DLA fractals result (A). The key process for dendritic islands is diffusion from corner to A-steps (B). Close-packed chains that occasionally form in (B) are no longer observed when a small atomic row is allowed to relax (C). Best agreement with experiment is obtained when corner to B-step diffusion is introduced (D).

### 3.4 Interlayer mass transport in homoepitaxial and heteroepitaxial metal growth

The ultimate goal in epitaxial growth is the controlled fabrication of atomically thin films with smooth abrupt interfaces. In the thermodynamic limit the growth morphology is determined by the balance of the interfacial energies involved [93]. In most cases, thin films are grown under experimental conditions far from equilibrium. Film growth and the resulting morphology will then be governed by kinetic effects. If the interlayer mass transport is sufficiently fast to allow atoms to leave the tops of growing two-dimensional islands as fast as they arrive, the growing layer will be completed before second-layer nucleation sets in and smooth layer-by-layer growth results. This is in general a delicate balance between several factors like the deposition rate, the density, size and shape of adlayer islands, the adatom diffusion barrier, and finally the activation barrier for an adatom to descend at the edges of adatom islands. The step-edge barrier  $E_s$  accounts for the fact that the diffusion barrier of an adatom over the edge of a step is different from that on the terrace [22-24]. Usually it is harder to step down from an upper terrace than to remain on the same level, i.e.,  $E_s > E_m$ , with  $E_m$  being the barrier of terrace diffusion.

Many microscopic details of the growth kinetics have recently been revealed by studies of Ag and Pt homoepitaxy on their (111) surfaces [56, 94-98]. Here, the kinetic effects could be studied in their pure form, as structural misfits and electronic inhomogeneities are absent. Both systems were found to grow in a multilayer (3D) growth mode at 300 K which was attributed to the limited interlayer mass transport at this temperature, ascribed to relatively large barrier heights for an adatom to descend a step edge. While the lateral diffusion barrier  $E_m$  governing the intralayer mass transport has been quantitatively determined for numerous metal systems [50, 51], quantitative measurements of the step-edge barrier  $E_s$ , though first postulated nearly 30 years ago, are rare [99, 100].

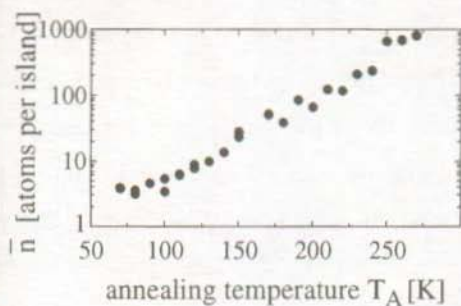


In this letter we present a general method for the quantitative determination of the interlayer mass transport in epitaxial growth. The method is based on the measurement of the nucleation rate on top of previously grown adlayer islands as a function of island size and temperature. The additional step edge barrier  $\Delta E_s = E_s - E_m$ , i.e., the barrier for an adatom to descend the step edge minus the surface diffusion barrier, as well as the corresponding attempt frequency  $\nu_s$  can be determined with high accuracy. This approach is applied to Ag homoepitaxy and heteroepitaxy on the (111) surfaces of Ag and Pt. In the homoepitaxial system, the additional step edge barrier is found to be  $\Delta E_s = 120$  meV. In the heteroepitaxial case,  $\Delta E_s$  is substantially lowered to  $\Delta E_s = 30$  meV. This dramatic decrease of the step edge barrier is likely to be associated with the preferential strain relief at the edges of heteroepitaxial islands facilitating the descend of an adatom.

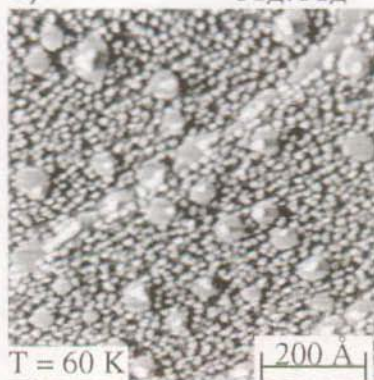
Figure 3.10 illustrates the method. Two-dimensional adlayer islands of well-defined size are built via evaporation of a submonolayer coverage at low temperatures and subsequent annealing [Figs. 3.10(a) and (b)], as described in detail in Ref. [7]. After a second evaporation of a submonolayer coverage the

**Figure 3.10** (next page): The STM image (a) and the graph (b) illustrate the building of 2D Ag islands on Pt(111) with defined sizes via deposition of 0.1 ML silver at 40 K and subsequent annealing. In (a) the annealing temperature was 230 K. The STM images (c)-(f) show the subsequent growth step in which 0.1 ML Ag are deposited (flux =  $1.1 \times 10^{-3}$  ML/s) on the previously grown islands. In (c) and (d), Ag is evaporated onto Ag islands on Pt(111) at temperatures of 60 K (c) and 85 K (d), respectively. In (e) and (f), Ag is evaporated onto Ag islands on Ag(111) at temperatures of 70 K (d) and 130 K (f), respectively. The STM images are measured isothermally at the temperatures of the second evaporation step. All images are taken in differential mode, which means that the derivative of the lines of constant tunnel current is recorded.

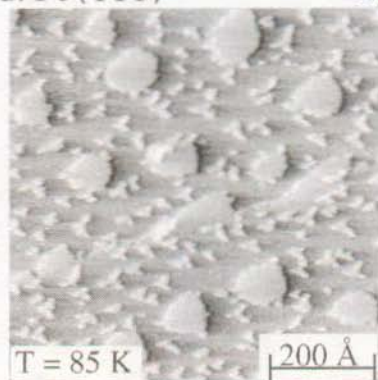
a) Size-tailored 2D – Ag islands



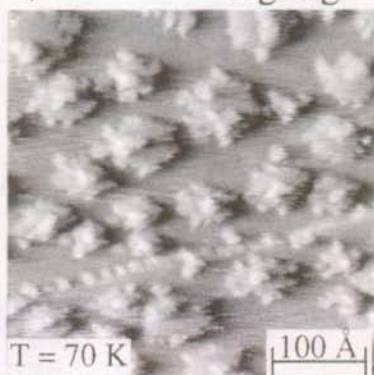
c) Ag/Ag – island/Pt (111)



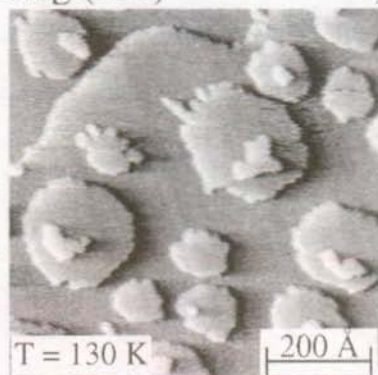
d)



e) Ag/Ag – island/Ag (111)



f)



nucleation on top of the preexistent islands and its dependence on the island size and temperature is examined [Figs. 3.10(c) - (f)]. The quantitative description of the experiment is based on nucleation theory and follows the idea of a critical island size for layer-by-layer growth [56]. In the absence of stable clusters, the adatom density on top of a compact island of radius  $R$  is a function of the distance from the island center and obeys the diffusion equation. Under steady-state conditions, the incident atom flux onto an island equals the step-down diffusion from the island at its perimeter. The coefficient for step-down diffusion  $S = C_s v_s \exp[-E_s/kT]$ ,  $C_s$  being a symmetry factor of order unity, enters thus via the boundary condition for the adatom density on top of an island. Knowing the spatial dependence of this adatom density, one can calculate the rate  $\Omega$  at which a stable cluster nucleates on top of an island of radius  $R$  by integrating the local nucleation rate over the area of the island. This leads to equation (3) of Ref. [56] which reads

$$\Omega = \frac{\pi \gamma D}{i+2} \left( \frac{F}{4D} \right)^{i+1} a^{2i-2} \left[ \left( R^2 + \frac{2a}{\alpha} R \right)^{i+2} - \left( \frac{2a}{\alpha} R \right)^{i+2} \right]. \quad (1)$$

Here,  $F$  is the incident atom flux,  $D = C_m a^2 v_m \exp[-E_m/kT]$  ( $C_m$  being a symmetry factor similar to  $C_s$ ) is the terrace diffusion coefficient,  $a^2$  is the area of the surface unit cell, and  $i$  denotes the size of the critical cluster. For  $i = 1$ ,  $\gamma$  is of order unity.  $\alpha = a^2 S/D = (v_s/v_m) \exp[-\Delta E_s/kT]$  is the quotient of the coefficients for step-down and terrace diffusion.

The fraction  $f$  of islands on which a stable cluster has nucleated increases during the second evaporation as  $df/dt = \Omega(1-f)$  which leads to

$$f = 1 - \exp \left[ - \int_t \Omega(R) dt \right]. \quad (2)$$

The integral describes the growth of the preexistent islands during evaporation time  $t$  and has to be treated differently for two limiting cases: i) All of the material impinging during the second evaporation causes an increase in the size of the

previously grown islands. No nucleation occurs between the islands [realized for Ag/Ag(111), see Figs. 3.10(e) and (f)]. ii) The mean diffusion length of the adatoms during the second evaporation is much smaller than the distances between the preexistent islands. Nucleation occurs on the terrace, and only the material which lands on top of an island causes its growth [realized for Ag/Ag/Pt(111), see Figs. 3.10(c) and (d)]. Hence, for the cases i) and ii), the increase of the island radius  $R$  of an island during the second evaporation has to be described differently. Knowing the coverage of both evaporations and the density of the preexistent islands, one can directly calculate the fraction of covered islands as a function of island radius  $R$  after the second evaporation.

Equation (2) predicts that the probability of finding second monolayer nucleation on top of the previously grown islands will rapidly change from nearly 0 for small islands to nearly 1 for large ones. The critical radius  $R$  at which this transition takes place depends strongly on temperature, as  $\Omega$  is a function of  $\alpha$  which varies as  $\exp[-\Delta E_s/kT]$ . One can thus separate the influence of the attempt frequencies  $\nu_s/\nu_m$  from the additional activation barrier  $\Delta E_s$  by measurements at various temperatures.

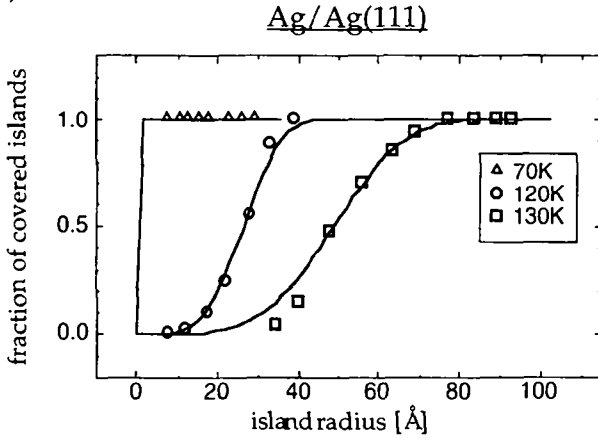
We applied this method to Ag/Ag(111) homoepitaxy and Ag/Pt(111) heteroepitaxy. The experiments were performed with a variable temperature STM mounted in UHV which operates in the temperature range from 25 to 800 K [61]. The Pt(111) crystal was cleaned by repeated cycles of Ar ion sputtering (750 eV) at 800 K and subsequent annealing at 1200~K. The Ag(111) surface was prepared by epitaxial growth of 50 monolayer thick Ag films on the Pt(111) surface [101]. The Ag submonolayers were evaporated with a Knudsen cell at a background pressure better than  $2 \times 10^{-10}$  mbar. The 2D Ag islands were grown by evaporation of 0.1 ML Ag at 40 K and subsequent annealing. This yields a population of compact 2D islands with a relatively sharp size distribution [Figs. 3.10(a) and (b), see Ref. [7] for details]. For the present study we have tailored

islands of average radii ranging from 10 to 100 Å. This size range assures that  $\Delta E_s$  is independent of the island size. Only for small clusters with less than about 50 atoms (i.e., typical radii  $<10$  Å) has the additional step-edge barrier theoretically been found to be size dependent [102].

The STM data in Fig. 3.10 show the expected behavior. At low temperatures, the onset of second monolayer growth takes place on many of the relatively small islands, whereas at higher temperatures the tops of even much bigger islands are devoid of nucleated clusters [Figs. 3.10(c)-(f)]. In Figure 3.11, the experimental data are compared with the theoretical predictions of Eq. (2). The island radii have been corrected for the increased imaging width due to the finite curvature of the scanning tip. The values of the attempt frequencies and activation barriers for terrace diffusion,  $\nu_m$  and  $E_m$ , and the size of the critical cluster  $i$  were determined independently by measurements of the saturation island density as a function of temperature for both systems, Ag/Ag(111) ( $E_m = 97$  meV,  $\nu_m = 2 \times 10^{11} \text{ s}^{-1}$ ,  $i = 1$  for  $T < 150$  K) and Ag/1MLAg/Pt(111) ( $E_m = 60$  meV,  $\nu_m = 1 \times 10^9 \text{ s}^{-1}$ ,  $i = 1$  for  $T < 90$  K) [13, 103]. Hence, the attempt frequency  $\nu_s$  and the additional step-down activation energy  $\Delta E_s$  are the only free parameters in the fits. It is important to note that the data for one single temperature can always be described by various combinations of  $\nu_s$  and  $\Delta E_s$ . The measurement of the temperature dependence of the step-down diffusion coefficient, however, allows to distinguish between the influence of the attempt frequency and the activation barrier. The values obtained from the fits in Fig. 3.11 are  $\Delta E_s = 120 \pm 15$  meV and  $\nu_s = 1 \times 10^{(13 \pm 1)} \text{ s}^{-1}$  for the system Ag/Ag-islands/Ag(111) and  $\Delta E_s = 30 \pm 5$  meV and  $\nu_s = 1 \times 10^{(9 \pm 1)} \text{ s}^{-1}$  for the system Ag/Ag-islands/Pt(111). The experimental error is mainly caused by the inaccuracy of the island radii which can be determined with a precision of about 5 Å.

The step-edge barriers as determined in our experiment have to be interpreted as effective ones, resulting from the different pathways an adatom can

a)



b)

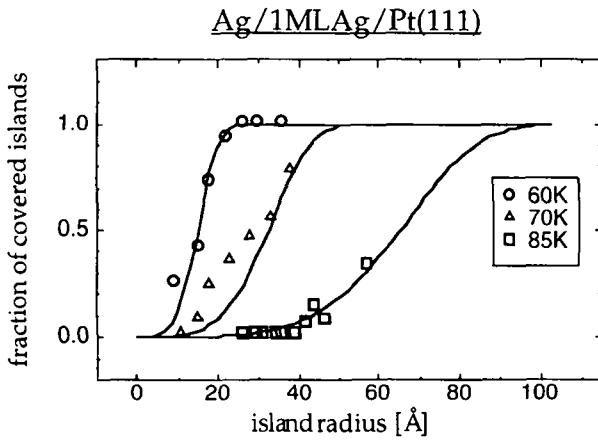


**Figure 3.11:** Quantitative evaluation of the nucleation probability for Ag on two-dimensional Ag islands on Ag(111) (a) and Pt(111) (b). The fraction of covered islands is shown as function of island radius and deposition temperature (flux =  $1.1 \times 10^{-3}$  ML/s).

use to descend. Theoretical studies show that the activation energy of interlayer diffusion on fcc(111) metal surfaces depends strongly on the atomic processes involved [15, 102, 104, 105]. For these surfaces, exchange processes are energetically

preferred with respect to direct hopping over the step edge, which has also been confirmed by field ion microscopy studies of the Ir(111) surface [90]. The theoretical studies reveal that, in particular, close to kink sites at the B-type steps, the lower atoms can easily be pulled outside, facilitating this exchange mechanism. Hence, at low temperatures, only those of the possible atomic processes with the lowest barrier should be thermally activated. As the size tailored 2D islands in our experiment have a relatively high density of kinks (as evidenced by the fuzzy STM imaging of the island perimeters), the measured step-down activation barriers are likely to correspond to the kinetically favored exchange processes at kink sites. For this process Li and DePristo [102] calculated an additional step-edge barrier of only 50 meV for the homoepitaxial Ag(111) system, which is about a factor of two below our experimental value. This difference is, however, not too surprising as embedded atom and effective-medium calculations usually underestimate diffusion barriers due to the incomplete account of the coordination at surfaces. In a very recent analysis of the occupancy of open layers as a function of coverage, developed for homoepitaxy, Meyer et al. found  $\Delta E_s = 150 \pm 20$  meV for Ag/Ag(111) from experiments at 300 K [98, 106], which is in fair agreement with our measurement.

The step-down activation energy in the heteroepitaxial system Ag/Ag-islands/Pt(111) is drastically lowered. This barrier of only 30 meV can easily be overcome, which is the reason for the perfect wetting of the first Ag monolayer on Pt(111) down to temperatures as low as 80 K. In this system, the Ag-islands in the first monolayer grow pseudomorphically on the substrate and are thus under a substantial compressive strain of 4.3% [59]. The pseudomorphic islands preferentially relief their strain at the edges where the Ag atoms are free to expand laterally. A second major difference to the homoepitaxial case is the different binding energy for an Ag adatom on the Pt(111) surface. While in homoepitaxy both, upper and lower terrace are energetically on the same level, in the case of Ag/Pt(111) the upper Ag terrace is about 170 meV higher in energy

than the lower Pt terrace [107] (see Fig. 3.12). Both effects may bend the step potential close to the step edge accounting for the substantial decrease in the step-edge barrier. It is difficult to decide a-priori which of the two, the strain relief at edges or the electronic adlayer-substrate coupling, is the dominating effect. We have, however, recently studied quantitatively the influence of lattice strain and electronic adlayer-substrate coupling for the Ag/Pt(111) system by effective-medium calculations [103]. In these calculations, strain effects clearly dominate the electronic adlayer-substrate coupling. It is thus most likely that the preferential strain relief at the edges of the pseudomorphic Ag-islands is the origin of the dramatic lowering of the step-edge barrier.

For the homoepitaxial Ag/Ag(111) system, the additional step edge barrier is found to be comparable to the lateral adatom diffusion barrier, which explains the rough growth morphology experimentally observed below 400 K [96]. This seems to be a general trend for homoepitaxial growth on fcc(111) metal surfaces where  $\Delta E_s$  has always calculated to be of the same order as  $E_m$  [15, 102, 104, 105]. Without affecting the intralayer diffusion, smooth growth morphologies at low temperatures can thus only be obtained via enhancement of the interlayer mass transport. This can be done either by increasing the visiting frequency of the adatoms at the step-edge or by lowering the step-edge barrier. The latter has been demonstrated by Esch et al. [95] to be effective in the oxygen mediated layer-by-layer growth of Pt/Pt(111). The reduction of the barrier height for the motion of Pt adatoms across oxygen-covered step edges can be understood in the light of the drastic barrier lowering observed for the compressively strained Ag islands on Pt(111). Pt islands on Pt(111) are under tensile stress. Chemisorption of an electronegative adsorbate (like oxygen) at the island edge weakens the bond between the core and the edge atoms of the Pt island accompanied by an outward relaxation of the edge atoms [108]. This lateral expansion at the edges of the islands should facilitate exchange diffusion processes and correspondingly lower their barriers. The specific lowering of the step-edge barrier via step decoration



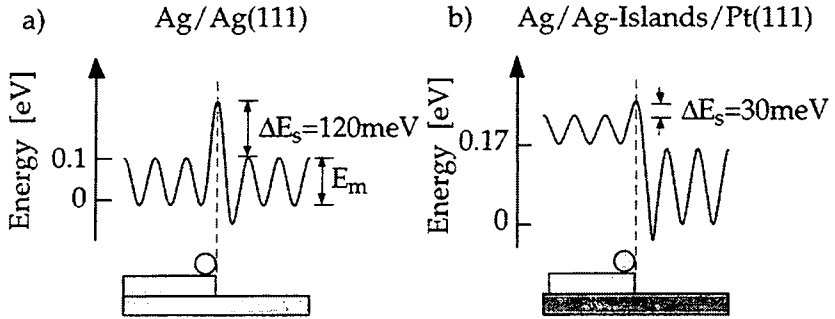


**Figure 3.12:** Potential energy diagram characterizing the interlayer and intralayer diffusion in Ag homoepitaxy (a) and heteroepitaxy (b) at the (111) surfaces of Ag and Pt. The intralayer diffusion barriers are from Refs. [101] and [13], the difference in binding energy in case (b) from Ref. [107].

with electronegative surfactants should be a general phenomenon, which might be applied to grow smooth homoepitaxial and heteroepitaxial metal films at low temperatures.

In conclusion, we have described an experimental method for the quantitative determination of the effective activation barrier of interlayer mass transport in epitaxial growth. The concept is based on nucleation theory and uses variable temperature STM. We have determined the effective additional activation barriers as well as the corresponding attempt frequencies for step-down diffusion in Ag homoepitaxy and heteroepitaxy on the (111) surfaces of Ag and Pt. On the pseudomorphic Ag-islands on Pt(111), the step-edge barrier is found to be substantially lowered with respect to the homoepitaxial system. This lowering is related to relaxation effects at the edges of the compressively strained islands. It is suggested that the lowering of the potential barrier observed for the descend of a Pt adatom across an oxygen-covered Pt step has the same microscopic origin.

## 4 Equilibrium and embedded nanostructures

In this chapter we deal with equilibrium structures of the system Ag/Pt(111). As already mentioned in the introduction, the "real" equilibrium in this system is formed by the surface-confined alloy of the two materials, and submonolayer coverages of Ag on top of the Pt(111) surface (chapter 4.3) are metastable. However, the structures addressed here can all be explained with the help of total energy arguments, which is the reason to unite them in one chapter. In chapter 4.2, the expression "embedded" should not be taken too literally. Although we treat the surface alloy, the interesting aspect there is its mesoscopic structure which is formed by islands on terraces.

One driving force involved in the formation of all structures treated in this chapter is strain. In the case of the alloy, strain is responsible for the development and the morphology of the surface alloy. Ag/Pt(111) is not a unique example for this behavior. Another interesting system is Cu and Ag codeposited on Ru(0001) [109]. The large lattice mismatch of Cu and Ag (13%) makes the two metals immiscible in the bulk. On Ru(0001), having an intermediate lattice constant, the two subsystems can relieve their strain by forming an alloy. As in the case of Ag/Pt, the resulting structure depends on the relative concentration of the two components.

In the case of Ag films on top of Pt(111) the strain is relieved by dislocation formation. Strong relaxation effects in the substrate make dislocation formation energetically favorable already in the first monolayer. The total energy of the pseudomorphic film, however, is not much higher than that of the dislocated structure. A similar case is Au/Ni(111) where two different structures with nearly the same total energy were found [110]. There, a moiré pattern transforms upon annealing into a structure with triangular dislocation loops. In contrast to that

case, however, the transformation between pseudomorphic and dislocated structures is not energetically hindered at 300 K for Ag/Pt(111).

#### **4.1 Stability of Disk and Stripe Patterns of Nanostructures at Surfaces**

Competing interactions give rise to a variety of complex structures at surfaces. In particular, the interplay between short-range attractive and long-range repulsive forces can lead to the formation of domain patterns of equally sized domains (islands), arranged into a regular, periodic pattern [111-118]. Such complex domain structures have been observed in different environments such as amphilic monolayers at the air-water interface [111-113], thin ferrimagnetic garnet films [114], and strained adlayers at crystal surfaces [115]. These systems are governed by long-range interactions of different physical origin: electrostatic or magnetic dipole forces and elastic interactions. For surface systems interacting via dipole interactions, the stability and phase diagram of the resulting domain structures has been investigated by theory [116-118] and computer simulation [119]. One of the intriguing results of these studies is that the phase diagram can comprise two basic domain morphologies: a two-dimensional array of compact domains (e.g. disks or squares) and a quasi one-dimensional arrangement of striped domains. The existence of disk and stripe phases and the transition between these phases has also been observed experimentally, e.g. in Langmuir monolayers [111-113].

Recently, it was proposed [120] that the formation of complex domain patterns observed on strained crystal surfaces governed by elastic forces [115, 121-123] could likewise be described in terms of long-range repulsive interactions. In fact, the theoretical description of the dipolar and elastic interactions turns out to be virtually identical [121, 122]. This is due to the fact that in both cases the

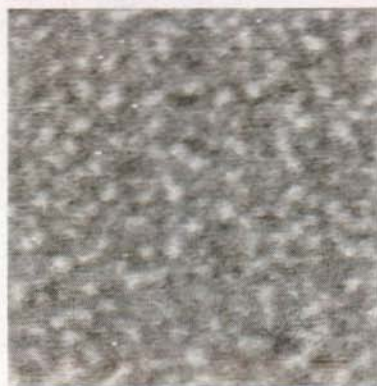
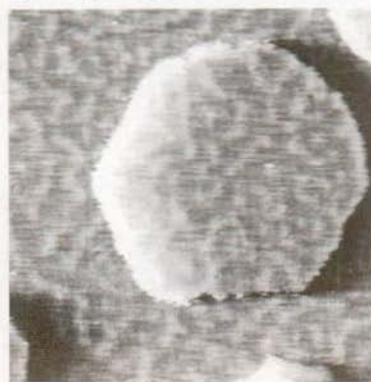
"effective" repulsion between domain boundaries scales as  $1/r^2$ , where  $r$  is the separation between these boundaries.

As a consequence of this formal analogy, it is interesting to explore whether both, stable disk and striped domain morphologies, can actually be observed in strained surface systems in a similar way as in dipolar systems. In fact, a transition from a compact to elongated island shape was recently observed for strained Ag islands grown on Si(001) [124]. Although no particular arrangement of the Ag islands was reported, the shape of a *single* island can by itself be regarded as a manifestation of the role of *effective* long-range interactions: the competition between the creation of domain boundaries (island edges) and the long-range interaction between them determine the island shape.

Here, we report the first observation of stable disk and striped domain shapes and patterns for a strained surface system, namely Ag embedded in the topmost layer of Pt(111). The embedded Ag nanostructures are prepared either by growing submonolayers of Ag at 300 K on Pt(111) followed by annealing at 700 K or by directly depositing Ag at 700 K. Both procedures lead to the formation of a two-dimensional "mixture", consisting of Ag clusters dissolved in the topmost Pt layer ( $\Theta_{\text{Ag}} < 0.5 \text{ ML}$ ) and Pt clusters inside a Ag matrix layer ( $0.5 \text{ ML} < \Theta_{\text{Ag}} < 1 \text{ ML}$ ), respectively [125]. (The presence of small clusters at elevated temperatures was recognized in an earlier He-scattering study by Becker et al. [126], but the underlying mixing transition was misinterpreted as a fragmentation of Ag islands into small clusters adsorbed *on top* of the Pt(111) surface). Once formed at elevated temperatures, this surface-confined mixture is stable upon recooling to room temperature. The stability of the embedded clusters was attributed to the balance of the strain relaxation (due to of the 4.3 % lattice misfit between Ag and Pt) and the line tension associated with the total Ag-Pt boundary length [25, 120].

The shape of the embedded Ag nanostructures and their relative arrangement have been studied by scanning tunneling microscopy (STM) and thermal energy atom scattering (TEAS) as a function of coverage and temperature. The two types of experiments were performed in separate ultrahigh vacuum (UHV) systems and on different samples. In both cases, the sample was processed in the same way: the Pt(111) surface was cleaned and characterized in situ, and a submonolayer amount of Ag was evaporated onto the Pt(111) surface by means of a Knudsen cell. Depending on the preparation procedure (see above), the sample was kept at 700 K during or heated to 700 K after Ag deposition in order to form the surface-confined Ag-Pt mixture.

The STM topographs presented in Fig. 4.1 clearly show the different morphology of the Ag-Pt surface layer as a function of the Ag coverage. The images have been recorded at 400 K after annealing to  $T > 700$  K. At low coverage (Figs. 4.1a and b,  $\Theta_{Ag} < 0.25$  ML), the embedded Ag atoms aggregate into small disk-shaped islands, about 10 Å in diameter, which appear as bright dots ( $\sim 0.6$  Å high) within the darker Pt surface. At higher Ag coverage (Figs. 4.1c and 1d,  $\Theta_{Ag} > 0.3$  ML), the islands have an elongated shape and are arranged into a striped "labyrinthine" pattern. Obviously, the relative arrangement of the Ag disks or stripes is far from being perfectly hexagonal or one-dimensionally striped. Nevertheless, there exists a certain degree of local order in that neighboring islands are separated preferentially by a distance of roughly 30 Å. This residual order of the island arrangement becomes more evident in the He-diffraction spectra shown in Fig. 4.2c. For the stripe as well as for the disk configuration (not shown here) the diffraction profiles exhibit broad diffraction features at a parallel wave vector transfer  $|Q| \approx 0.2 \text{ Å}^{-1}$ . These features are most pronounced for low surface temperature and indicate a lateral periodicity on the surface of  $D = 2\pi / |Q| \approx 30 \text{ Å}$ . This value is in good agreement with the average distance between embedded Ag islands extracted from the STM images.

$\Theta = 0.08 \text{ ML}$  $\Theta = 0.22 \text{ ML}$  $\Theta = 0.30 \text{ ML}$  $\Theta = 0.55 \text{ ML}$ 

100 Å

 A horizontal scale bar with vertical end caps, indicating a length of 100 Å.

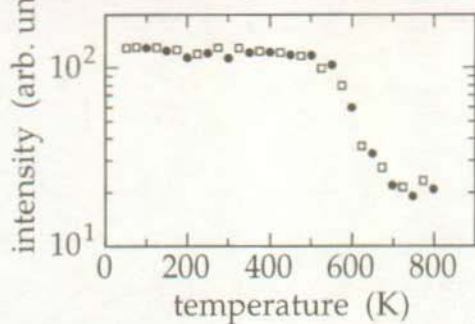
**Figure 4.1:** Constant-current STM topographs ( $225\text{\AA} \times 225\text{\AA}$ ) of a Pt(111) surface after deposition of submonolayer amounts of Ag annealed at elevated temperatures ( $T > 700\text{K}$ ), and imaged at 400 K: (a) Ag-coverage:  $\Theta_{\text{Ag}} = 0.08 \text{ ML}$ , annealing temperature:  $T = 700\text{K}$ ; (b)  $\Theta_{\text{Ag}} = 0.22 \text{ ML}$ ,  $T = 850\text{K}$ ; (c)  $\Theta_{\text{Ag}} = 0.30 \text{ ML}$ ,  $T = 800\text{K}$ ; (d)  $\Theta_{\text{Ag}} = 0.55 \text{ ML}$ ,  $T = 850\text{K}$ . Note that in taking (b) and (c) a high-pass filter was used which enhances the contrast for steep changes of the tip-height. (a) and (d) are regular gray-scale images of the tip-height.

The STM topographs in Fig. 4.1 are remarkably similar to the patterns obtained in a recent computer simulation of a dipolar lattice gas for similar coverages [119]. They should also be compared to the disk and stripe arrangements observed in Langmuir monolayers [111-113], in which, however, the structures occur on a much larger, mesoscopic length scale.

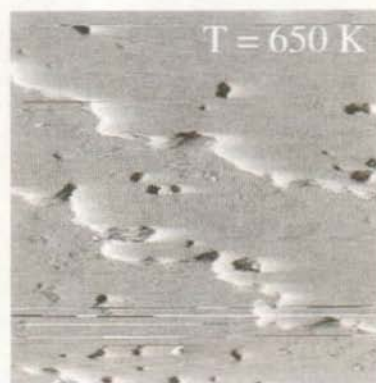
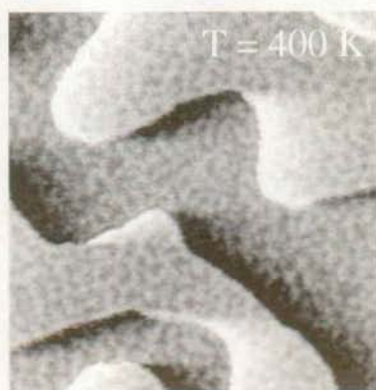
In the following, we will demonstrate that the transition from a disk to a stripe pattern with increasing coverage can be explained in a simple, straightforward way. We have shown in a recent letter [120] that the formation and the variation of the strain-induced pattern can be described within a simple analytical model based on the energy balance between the free energy  $\gamma$  associated with the creation and elastic relaxation of a domain boundary and the long-range effective repulsion  $\propto \sigma/r^2$  between these boundaries. We emphasize that this model does not explicitly include effects due to the presence of corners or kinks along the boundary, nor does it account for the thermal disordering of the domain pattern. Therefore, the model can only provide a qualitative description of the general behavior.

**Figure 4.2** (next page): Intensity (peak height) of the specularly reflected He-beam (a), He-diffraction spectra (c), and STM topographs ( $450\text{\AA} \times 450\text{\AA}$ ) of the Ag-Pt(111) mixture for  $\Theta_{\text{Ag}} = 0.5\text{ML}$  (striped phase) taken at different temperatures. Open and filled symbols in (a) correspond to measurements taken during increasing and decreasing the surface temperature, respectively. The He-diffraction profiles in (c) were recorded along the  $[11\bar{2}]$ -direction, using a He-beam energy of 21.6 meV and fixed total scattering angle ( $\vartheta_i + \vartheta_f = 90^\circ$ ).

a)  $Q_{Ag} = 0.5 \text{ ML}$

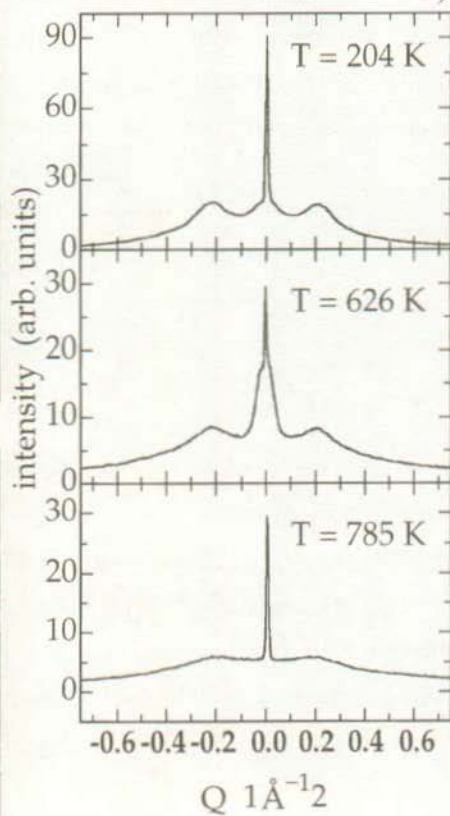


b)



100 Å

c)





The excess free energy per unit area gained by formation of a perfectly regular domain pattern can be expressed as [120, 127]<sup>1</sup>:

$$\Delta F = \alpha \frac{\gamma \cdot \Theta}{\ell} + \frac{\alpha}{2} \cdot \frac{\sigma \cdot \Theta}{\ell} \left( \frac{1}{(D - \ell)^2} + \frac{1}{\ell^2} \right), \quad (1)$$

where  $\ell$  and  $D$  characterize the domain width and separation, respectively, and  $\alpha$  denotes the number of nearest-neighbor domains. For a stripe pattern  $\alpha = 2$ , for a checkerboard array  $\alpha = 4$ , and for a hexagonal arrangement of hexagon-shaped disks  $\alpha = 6$ . The main difference between the 2D arrangement of disk-like domains (squares or hexagons) and the 1D arrangement of stripe domains is the variation of  $\ell$  and  $D$  with coverage  $\Theta$ : for the minimum energy configurations the domain size  $\ell(\Theta)$  and the periodicity  $D(\Theta)$  for the stripe pattern are given by

$$\ell(\Theta) = c_1 \sqrt{1 + \frac{\Theta^2}{(1 - \Theta)^2}}, \quad D(\Theta) = c_1 \sqrt{\frac{1}{\Theta^2} + \frac{1}{(1 - \Theta)^2}}, \quad (2)$$

while for the disk pattern the result becomes

$$\ell(\Theta) = c_2 \sqrt{1 + \frac{\Theta}{(1 - \sqrt{\Theta})^2}}, \quad D(\Theta) = c_2 \sqrt{\frac{1}{\Theta} + \frac{1}{(1 - \sqrt{\Theta})^2}}. \quad (3)$$

The proportionality constants  $c_1 = \sqrt{-3\sigma_1 / 2\gamma_1}$  and  $c_2 = \sqrt{-3\sigma_2 / 2\gamma_2}$  are given by the ratio between the relaxation energy and the strength of the repulsive interaction per unit length of a boundary. The indices 1 and 2 take into account that these values will, in general, be different for the stripe and disk configurations, e.g. due to the surface anisotropy. In Fig. 4.3 we have plotted the excess free energy  $\Delta F$  obtained after substituting the minimum energy configurations (2) and (3) into (1). The relative position of the two curves

---

<sup>1</sup> In the original publication Equation 1 was erroneously written as

$$\Delta F = \alpha \frac{\gamma \cdot \Theta}{D} + \frac{\alpha}{2} \cdot \frac{\sigma \cdot \Theta}{D} \left( \frac{1}{(D - \ell)^2} + \frac{1}{\ell^2} \right).$$

determines whether the disk or stripe phase will be energetically preferred. Three different scenarios are possible: if  $c_1 \ll c_2$  the stripe pattern will be stable for all coverages. If  $c_1 \gg c_2$  only the disk pattern will be observed. In the intermediate regime, where  $c_1 \approx c_2$ , the two curves can cross such that for low coverage the disk pattern is energetically stable while at higher coverage the stripe pattern is preferred. In this case, the model would predict a transition from the disk to the stripe phase via an intermediate coexistence region, the composition of which is given by the "lever rule" for binary systems (see e.g. chapter 11 in [128]). Note that the present model does not include the possibility for a continuous transition from a compact to an elongated shape of an individual island. This is, however, what appears to occur in the real physical system (see e.g. Fig. 4.1c). We, therefore, believe that the model does not correctly describe the Ag/Pt(111) patterns in the 2D-1D transition regime. We emphasize that due to the particular shape of the two curves in Fig. 4.3, the present model predicts that the opposite sequence, namely a transition from a stripe to a disk phase with increasing coverage cannot occur for coverages  $\Theta < 0.5$  ML. Note, however, that symmetrically above 0.5 ML a similar transition from the striped phase to a hole ('anti-disk') phase is expected. Since the different shape of the two curves in Fig. 4.3 is due to the different scaling of  $\ell$  and  $D$  with the coverage  $\Theta$  for the 1D stripe and 2D disk patterns (Eqs. 2 and 3, respectively) the disk to stripe transition in this simple model can be understood on purely geometric grounds.

Until now we have demonstrated the *existence* of disk and stripe domain shapes and patterns in the Ag-Pt(111) system without considering the *stability* of these patterns. To learn whether the observed structures are true equilibrium patterns (as expected from theory and simulation [116-123]) or merely the result of surface kinetics, we have studied the thermal stability of the embedded Ag island structure. The experimental results are summarized in Fig. 4.2 for the striped morphology.

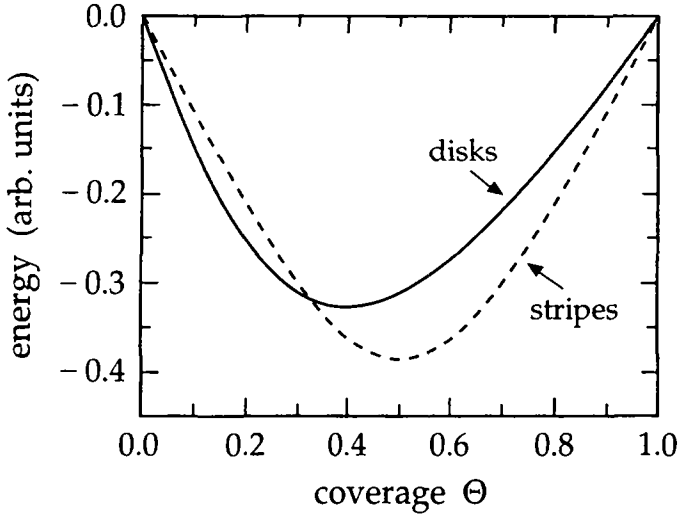


**Figure 4.3:** Excess free energy as a function of coverage after formation of regularly ordered domain patterns of 2D and 1D symmetry, corresponding to a disk-phase (solid line) and stripe-phase (dashed line), respectively. The excess free energy for each coverage is calculated according to (1) for the minimum energy configurations of a perfectly ordered disk phase and stripe phase as given by (2) and (3). The parameters are  $c_1 = 1.22$  ( $\sigma_1 = 1$ ,  $\gamma_1 = -1$ ) for the stripe-phase and  $c_2 = 1.64$  ( $\sigma_2 = 1$ ,  $\gamma_2 = -1.8$ ) for the disk-phase which was modeled as a checkerboard array of square domains ( $\alpha = 4$ ).

The intensity of the specularly reflected He-beam ( $Q=0$ ) as a function of the temperature is shown in the top panel of Fig. 4.2. It provides a measure of the scattering factor of the *individual* islands and is, therefore, sensitive to changes of the island shape as well as to the number of surface defects [129]. The sharp intensity drop at a surface temperature  $T \sim 550$  K marks the beginning of the disordering of the striped domain pattern. The onset of the deterioration of the domain structure is also revealed in the He-diffraction spectra shown in Fig. 4.2c: for  $T > 550$  K the intensity of the diffraction signatures at  $|Q| \approx 0.2 \text{ \AA}^{-1}$

continuously decreases with respect to the specular intensity and vanishes almost completely at around 700 K<sup>1</sup>.

A possible and likely scenario for the thermal disordering of the domain structure is the increased meandering of the stripes followed by the dissolution of the stripes into smaller structures. Both disordering mechanisms would be accompanied by a proliferation of the total length of the Ag-Pt domain boundaries, which would account for the observed strong decrease of the specular intensity above 550 K.

In addition to the specular intensity decrease and the disappearance of the diffraction satellites at  $|Q| = 0.2 \text{ \AA}^{-1}$ , another interesting feature is observed in the diffraction spectra during the disordering of the striped phase: in the transition region between 550 K and 700 K, a triangular-shaped foot develops underneath the specular peak, centered around  $Q = 0$  (see, for instance, the spectrum for  $T = 626 \text{ K}$  in Fig. 4.2b). We note that a very similar diffraction feature was observed in He-scattering from a Ni(110) surface covered with a monolayer of hydrogen [130]. The triangular peak was then attributed to atomic size defects, namely missing hydrogen atoms in an otherwise perfectly ordered adlayer. In the present case the same distinctive feature could arise from small Ag or Pt defects which are formed during the disordering of the striped phase.

This interpretation is supported by the STM studies. In Fig. 4.2b we present two STM topographs characterizing the morphology of the Ag-Pt(111) surface mixture for  $\Theta_{\text{Ag}} = 0.5 \text{ ML}$  at temperatures of 400 K and 650 K, respectively. At the higher temperature the labyrinthine pattern has completely disappeared in the

---

<sup>1</sup> The specular intensity curves discussed here should not be confused with the specular reflectivity measurements by Becker et al. in Ref. [126]. The TEAS measurements of Becker et al. characterize the *irreversible* embedding transition of the adsorbed Ag islands into the topmost Pt layer while the specular intensity curves reported here characterize the *thermal equilibrium* behavior of the already embedded Ag nanostructures.

STM topograph; the terraces are imaged completely flat, and no contrast arising from the different Ag and Pt imaging heights is seen<sup>1</sup>. We interpret this as evidence for a completely disordered 2D Ag-Pt phase at elevated temperatures. In such a phase Ag and Pt atoms are mixed randomly in a dense packing, and the surface appears flat in the STM. More information on the atomic structure of the disordered 2D mixed phase could be obtained from atomic resolution images, which we were not, however, able to obtain from this system at elevated temperatures. The thermal dissolution of the Ag cluster is preceded by a gradual disordering of the domain pattern. At temperatures around 600 K the meandering stripes of embedded Ag clusters are still visible in the STM images (not shown here) but are characterized by an increased interfacial width and large local fluctuations.

Both, STM observations and He-scattering measurements thus support a thermal disordering scenario in which the Ag stripes would disorder by forming small protrusions followed eventually by the dissolution into small Ag clusters or individual Ag atoms. This picture is also in agreement with the results obtained in the computer simulation of the thermal disordering of the striped phase in Ref. [119]. We would, therefore, expect the Ag-Pt striped phase to look similar to the "snapshots" of the Monte Carlo simulation shown in Fig. 3 of Ref. [119].

Finally, we emphasize that the disk phase undergoes a thermal disordering transition, too. In both cases, the variation of the He-specular intensity with temperature as well as the corresponding changes in shape of the He-diffraction spectra are completely reversible. This strongly suggests that both, the disk and

---

<sup>1</sup> The appearance of flat terraces in the STM is not related to the enhanced mobility of atoms and cluster at high temperatures. In the 650 K image in Fig. 4.2b) steps and defects (small holes in the Ag-Pt layer) are found to be "stable" on the time scale necessary to record an image.

stripe phase, are indeed equilibrium structures stable at lower and higher coverage, respectively, and for surface temperatures below 700 K.

We acknowledge fruitful discussions with Max G. Lagally, Bene Poelsema, Rolf Schuster, Ian Robinson, and Georg Rosenfeld.

## **4.2 Stress relief via island formation of an isotropically strained, bimetallic surface layer: the mesoscopic morphology of the Ag/Pt surface alloy**

Elastic strain, caused by crystalline mismatch, is well known to have a profound influence on the morphology of a coherent two-phase alloy. A precipitate-matrix misfit in such systems can drive a nearly random spatial phase distribution into a highly ordered domain structure [131]. The changes in morphology and spatial correlation occur on a mesoscopic length-scale due to the long-range nature of the strain-induced elastic interactions between precipitates.

In recent years it has been realized that surface stress can have very similar effects on the surface morphology [120, 132]. For example the intrinsic tensile stress of the Au(111) surface, caused by the reduced number of nearest neighbors of the surface atoms, drives this surface into a herringbone reconstruction, with a mesoscopic domain width of  $\approx 150 \text{ \AA}$  [133, 134]. Similarly, externally imposed stress may lead to the same phenomena: Upon O-adsorption on Cu(110) there form striped arrays of the (2x1) O/Cu(110) structure spontaneously on the clean Cu-surface [115]. Whereas in these examples the surface structure constitutes a patchwork of domains with either anisotropic or even intrinsically different stress tensors in the different domains, similar effects have also been observed at surfaces which do not form different surface domains. For example on Pd(110) a regular arrangement of islands was found even though no obvious difference between the surface on the islands and the terrace exists [127].

Marchenko [135] and Alerhand et al. [136] pointed out that in the case of anisotropic surface domains, i.e., different stress tensors in the different domains (far away from the steps), the elastic stress can be released very effectively by the formation of domain boundaries. Domain boundaries here refers to boundaries between any kind of surfaces patches, as there are for example steps or walls between different domains. The elastic relaxation energy diverges logarithmically with the distance between the domain boundaries and hence eventually compensates for the energy necessary for the formation of an isolated domain boundary. This model, however, is not applicable when no difference of the stress tensor between neighboring domains exists, as it is the case with Pd(110) [127]. Here the elastic repulsion of the steps is proportional to the inverse of their squared distance [137]. As this repulsion results in a positive contribution to the surface free energy for all step distances, the authors introduced a negative formation energy for an isolated step to stabilize such regular arrangements of islands. Assuming an effective local relaxation of surface stress at step edges, this seems very reasonable but at the same time opens new questions, e. g. how roughening of the surface is prevented.

In this paper we present scanning tunneling microscopy (STM) results on the formation of islands on an *isotropically* stressed surface, the surface alloy of Ag/Pt. Depositing Ag on the Pt(111) surface at coverages below one monolayer and slight annealing to temperatures above 620 K results in the formation of a surface alloy: Pt and Ag intermix in the first layer and form a uniform surface layer, consisting of small Ag clusters ( $\approx 10 \text{ \AA}$ ) embedded in the Pt surface [125]. The intermixing is restricted to the first layer. As pointed out by Tersoff, the simple framework of surface and interface energies of the two respective species is not sufficient to explain the observed results, i.e., the miscibility at the surface with the bulk solubility tending towards zero [25]. What is neglected in this simple picture is the difference between the stress due to the lattice misfit of a simple Ag monolayer and that of the intermixed layer. Indeed, Tersoff proved

that there occurs mixing in the surface layer despite of a positive interface energy between the two species: The strain fields of the deposited atoms tend to separate these atoms and mix them into the surface layer. Intermixing into deeper layers is strongly unfavorable. The positive interface energy between the two species leads to clustering, as observed in the experiment.

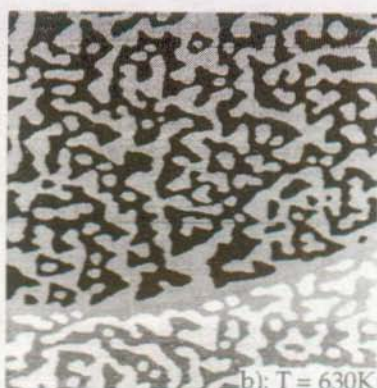
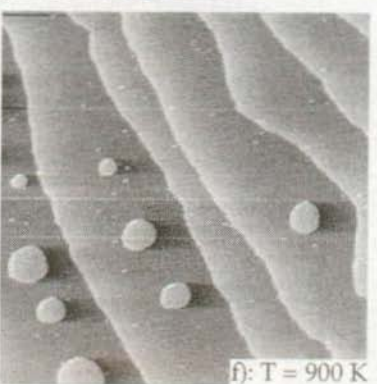
Due to the lattice mismatch of Ag and Pt (nearest neighbor distances:  $d_{\text{Ag}} = 2.89 \text{ \AA}$ ;  $d_{\text{Pt}} = 2.77 \text{ \AA}$ ), this uniform surface mixture is expected to be under considerable stress, which might render this surface unstable against relaxation, at least on large length scales. In this paper we show that careful annealing of the (already microscopically intermixed) surface leads to the formation of islands on the larger terraces. We followed the process of their formation by scanning tunneling microscopy (STM): In the course of the annealing large islands break apart into smaller ones. This rather stable arrangement of round islands shows a peaked width distribution with an average island diameter of 150-300  $\text{\AA}$ , slightly depending on the terrace width, which indicates an interaction between island and terrace steps. As there is no difference of the surface structure in the islands and on the terraces, the main elastic interactions of the steps are supposed to follow the above  $1/l^2$  law, where  $l$  is the distance between the steps. Compensation of that step repulsion and their formation energy has to be sought in a very efficient relief of strain perhaps due to lateral relaxation of the islands.

The experiments were performed with a variable temperature UHV scanning tunneling microscope as described in [34]. The Pt(111) surface was prepared by subsequent cycles of Ar-sputtering, annealing in oxygen atmosphere, and flash annealing to 1200 K. Ag was evaporated from a Knudsen cell with a Boron nitride crucible at a rate of 1 monolayer (ML) per 900 s. After annealing of the sample to the respective temperatures, the STM images were recorded at 400 K.



Fig. 4.4a) shows the Pt surface after deposition of 0.55 ML Ag at 400 K and annealing to 550 K for 100 s. The Ag forms triangular islands on the terraces. From previous work the Ag is known to occupy fcc sites [63]. The straight island edges are running along the close packed  $[1\bar{1}0]$  directions. The preference of B-type steps [90] (forming {111} microfacets) leads to the triangular appearance of the islands in Fig. 4.4a). The Pt-steps are wetted by Ag. Additionally a few white spots are resolved, probably representing mobile and metastable Ag clusters as discussed in [138]. Besides Fig. 4.4b) all STM images shown in this paper are high pass filtered and hence appear as illuminated from the left hand side. The colors in these images do not correspond to absolute heights, rather to relative heights of neighboring patches, where the brighter color corresponds to ascending of the STM tip. The feature in Fig. 4.4a), marked with A corresponds to a Ag seamed ascending step edge (upon going from left to right), whereas B marks an Ag island on the Pt surface. These identifications of the features were made in more detail in [125]. In STM images (not shown), depicting the absolute heights of the

**Fig. 4.4** (next side): STM topographs of the Ag/Pt(111) system with  $\theta_{\text{Ag}} = 0.55$  ML after annealing to different temperatures. The STM images were taken at 400 K; a) annealing at 550 K for 100 s formed triangular shaped Ag-islands on the terraces; A marks an Ag-seamed upward step, B marks a Ag island on a Pt terrace. b) additional annealing at 630 K for 100 s started the mixing of the Ag into the Pt surface. c) after subsequent annealing to 750 K for another 100 s the intermixing was completed (the inset ( $225\text{Å} \times 225\text{Å}$ ) reveals the microscopic morphology of the Ag-Pt surface alloy). d) further annealing at 850 K for 100 s caused meandering islands of the Ag/Pt mixture with finger like protrusions. e) another annealing for 100 s at 900 K leads to the final structure, round intermixed islands on large terraces, which are also homogeneously mixed. f) These islands exist only on terraces above a critical width of  $\approx 400\text{Å}$ . The image sizes are  $2300\text{Å} \times 2300\text{Å}$ . All images except b) are high pass filtered (see text).

a):  $T = 550 \text{ K}$ b):  $T = 630 \text{ K}$ c):  $T = 750 \text{ K}$ d):  $T = 850 \text{ K}$ e):  $T = 900 \text{ K}$ f):  $T = 900 \text{ K}$

tip at constant tunneling current, the Ag is imaged approximately  $0.6 \text{ \AA}$  higher than the Pt. This holds true for all applied tunneling conditions ( $-0.5 \text{ V} \leq U_T \leq -1.5 \text{ V}$ ;  $1 \text{ nA} \leq I_T \leq 3 \text{ nA}$ ), and for the intermixed phase. As the true difference of the atomic radii amounts only to  $0.1 \text{ \AA}$ , this cannot be a purely geometric effect. Differences in the electronic structure, due to strain within the Ag patches, might be responsible for the observed imaging heights.[59, 125].

In Fig. 4.4b) after 100 s of annealing at 630 K the intermixing of Ag and Pt starts, most obvious from the changed island morphology, where the triangular islands have transformed into rather round ones. On a microscopic scale small amounts of (dark) Pt indentations of  $\approx 10 \text{ \AA}$  size have formed in the Ag islands. On the other hand, the Pt terraces reveal (bright) Ag-protrusions preferentially at the Ag wetted Pt step edges. As discussed in detail in [125], the intermixing process occurs very effectively at the step edges, where only intralayer mass transport is required. But also some interlayer mass transport is kinetically allowed as follows from detailed investigations of the intermixing of isolated Ag islands with the substrate Pt on large terraces (not shown here). They revealed higher cluster concentrations in the vicinity of the island perimeters. This holds true for both the Ag clusters mixed into the terraces and for the Pt clusters mixed into the Ag islands and implies that also the interlayer mass transport proceeds preferentially at the edges of the islands.

Additional annealing to 750 K for 100 s leads to complete intermixing of Ag and Pt in the top layer as can be seen from the inset in Fig. 4.4c). At 0.55 ML Ag the Ag-clusters (bright) in the topmost layer touch already and form a network with a typical thickness of  $\approx 10 \text{ \AA}$ . It should be noted that the intermixing can also be achieved by longer annealing at 630 K [125]. Meandering interconnected islands have formed on the terraces, sometimes including holes and round islands. Closer inspection reveals that the islands are surrounded by  $\approx 10 \text{ \AA}$  wide rims, imaged at the same height as the Ag clusters. They are therefore interpreted

as small Ag seams, wetting the island and step edges. The preferred distance between the islands is about 50-100 Å. In Fig. 4.4c) the islands cover still about 50 % of the terrace, as is expected from the deposited amount of Ag.

Upon subsequent annealing to 850 K for 100 s [Fig. 4.4d)] the meandering islands develop finger like protrusions, with a width of about 200 Å. Most of the holes in the meandering islands have disappeared, and the fraction of the surface covered by islands has considerably reduced, indicating effective mass transport of Ag and Pt towards the terrace edges.

Heating to 900 K for an additional 100 s leads to the final configuration of the intermixed surface [Fig. 4.4e)]. One ends up with fairly round shaped islands of an average diameter of 275 Å and a fairly narrow size distribution with a standard deviation of  $\pm 80$  Å. The STM images show no difference of the local morphology of the surfaces on islands and terraces. According to the former experimental results [125] and the theoretical considerations of Tersoff [25] the Ag mixes only into the topmost layer. The island edges are still seamed by a  $\approx 10$  Å wide rim of Ag. Annealing to higher temperatures does not change the overall morphology, even though at slightly higher temperatures considerable thermal desorption of Ag sets in. It is also worth mentioning that the same morphology is obtained by annealing half a monolayer of Ag on Pt(111) at 630 K for 100 min. The average width of the islands depends slightly on the width of the terrace, on which they are formed, with smaller terraces leading to smaller island sizes. However, the narrow width distribution with a standard deviation of about a quarter of the average width remains unchanged. In Fig. 4.4f) it can be seen that these islands form only on terraces with a critical width above  $\approx 400$  Å.

Why do these small homogeneously distributed islands form at all? There are no topological constraints, which could prevent the meandering islands in Fig 4.4 c) and d) from collapsing into large compact islands. Nevertheless, the meandering islands decay into smaller ones. Additionally, the area covered by

islands on a terrace reduces considerably during the first steps of the annealing sequence in Fig. 4.4. On smaller terraces these islands even dissolve completely. This substantial mass transport towards the step edges stops once the island structure has formed, and there is no obvious effect of further annealing. Only after 10 min annealing at 900 K, where already about 20 % of the Ag had desorbed, slight modification of the island density was found. Furthermore a formation of the islands due to condensation of a two dimensional gas of Ag and Pt atoms or small clusters upon the quenching from the annealing temperature to the observation temperature of 400 K can be ruled out: The same island morphology has been obtained with both procedures, stepwise annealing up to 900 K (for 100 s) and annealing at 630 K for 100 min. Assuming the equilibrium between the (solid) terraces and a two dimensional gas phase following the Clausius Clapeyron equation, the density of the two dimensional gas on the terraces should depend exponentially on the temperature. Hence also island density and size were expected to vary significantly between the two annealing procedures. Additionally, STM images recorded directly at 650 K do not reveal any hints for a mobile, dilute Ag-Pt phase on the terraces, which is further supported by the absence of detectable mobility of the steps of the surface alloy, even at 650 K [139].

From both of the above arguments, i. e., no evident influence of neither the further annealing nor the annealing procedure, we conclude that these islands constitute the *equilibrium* structure of this stressed surface layer on terraces above a critical width of  $\approx 400\text{\AA}$ . We do not want to claim that this morphology necessarily constitutes the absolute thermal equilibrium structure of the surface, which could e.g. consist of a stepped surface with terrace widths below the observed critical one. Such a rearrangement would require long range mass transport over several surface layers and might be kinetically suppressed up to the desorption temperature of Ag.

A clue for the understanding of the island structure can be found in their local distribution. They are more or less homogeneously spaced, indicating mutual repulsion. Also the concave step edge in Fig. 4.4f), bending away from the islands on the lower terrace substantiates this implication. A straightforward explanation is long range step-step repulsion, due to elastic stress in the crystal surface. As mentioned above such a repulsion between steps, which separate domains with no significant difference in their stress tensor, should decrease with  $1/l^2$ , where  $l$  is the separation between steps. This positive repulsion energy has to be compensated by a negative energy contribution to stabilize the island pattern. As the fairly round island shape indicates a tendency for the steps to shorten and hence a positive formation energy for an (isolated) step, such a contribution has rather to be sought in the effective relaxation of the islands themselves. Indeed, in recent reflection high energy electron diffraction (RHEED) investigations of the homoepitaxy of Cu on Cu(001) Fassbender et al. found a periodic oscillation of the in-plane lattice constant with the layer thickness, which was interpreted in terms of *lateral relaxation* of Cu islands at incomplete monolayers of Cu [140]. Such a relaxation effect, whose efficiency should increase with decreasing diameter of the islands, could overcompensate the step-step repulsion and the formation energy of a step for small island diameters and might therefore lead to the stabilization of the observed surface morphology. It should also be noted that the Ag seams, covering the step edges, signal an enhanced adsorption energy for Ag atoms at these step edges, which is also thought to considerably decrease the formation energy of the steps.

We showed that the observed mechanism, the spontaneous formation of islands, is effective for the relief of surface stress even in systems with isotropic surface domains. This is principally different from systems like the herringbone reconstruction on Au(111) or the striped arrangement of (2x1) domains on O/Cu(110), where long range elastic relaxations due to the anisotropy of the stress tensor in the different domains compensate for the elastic repulsion and

formation of the domain boundaries. In our case we reported on a system, where the relaxation of the domains themselves, depending on their lateral extent, is considered to compensate for the mutual step-step repulsion and the step formation energy. Such a lateral relaxation might also be the explanation for the observed formation of islands on the Pd(110) surface. It would then become unnecessary to introduce a negative step formation energy, which could furthermore solve the problem of surface roughening, expected to result from such a negative step formation energy.

The authors thank S. Narasimhan, E. Pehlke, H. Ibach and P. Zeppenfeld for fruitful discussions and comments.

### **4.3 Reentrant pseudomorphic growth in metal heteroepitaxy**

The structure of ultrathin films on substrates of a different material is determined by the atomic interactions at the interface and the structures of the two respective bulk phases. A lattice mismatch between film and substrate material leads to strain in the film until the overgrowth has adopted its bulk geometry through introduction of strain relieving defects. Frank and van der Merwe [141] were the first to address theoretically the strain relaxation in a heteroepitaxial system which they modeled by the Frenkel-Kontorova approach [142] of a one-dimensional chain of atoms coupled by elastic springs in a sinusoidal (substrate) potential. Later, two- and three-dimensional models based on elastic continuum theory were developed [143-145]. These "continuum" models predict either a critical misfit above which dislocations form in a complete monolayer, or vice versa a maximum film thickness for pseudomorphic growth which depends on the actual misfit of the system and the elastic material parameters.

Though heteroepitaxial metal films were believed to be well described by these theories, recently strain relief mechanisms were revealed that lead to deviations from the predictions [58, 59, 110, 146-148]. On hexagonal close-packed interfaces, for example, strain can easily be accommodated by fcc-hcp stacking faults, and the critical thickness is dropped to zero or just the first monolayer. These so called partial dislocations can arrange in a variety of structures, including unidirectional or trigonal dislocation networks [58, 59, 147] or even dislocation loops in the substrate [110]. Further, strong relaxation effects in the substrate can energetically stabilize such structures [148]. The resulting morphologies in these systems often vary from layer to layer, and for each respective layer sometimes metastable configurations exist apart from the energetically most favored one. However, despite of their structural variety, all these systems have one thing in common: the existence of a critical coverage above which, if not kinetically hindered, strain relieving defect structures form until the growing film has adopted its bulk geometry.

In this letter we demonstrate that even this qualitative prediction of elastic continuum theory can fail. In our example of the first monolayer of Ag on Pt(111) a dislocation network evolves when islands reach a critical size and accumulate a critical amount of strain. Surprisingly, this dislocation network completely disappears upon completion of the first monolayer and the beginning growth of the second. We attribute the maximum lateral size for pseudomorphic growth of two-dimensional islands to the delicate balance between edge relaxation and dislocation formation. The reentrant pseudomorphic growth upon monolayer completion can be explained by taking into account the chemical potential of an adatom gas present on top of the adlayer.

So far, experiments performed with STM, He-diffraction, LEED, and photoelectron diffraction (PED) reported the first monolayer of Ag to grow pseudomorphically on Pt(111) [59, 63, 101, 107]. With increased resolution,



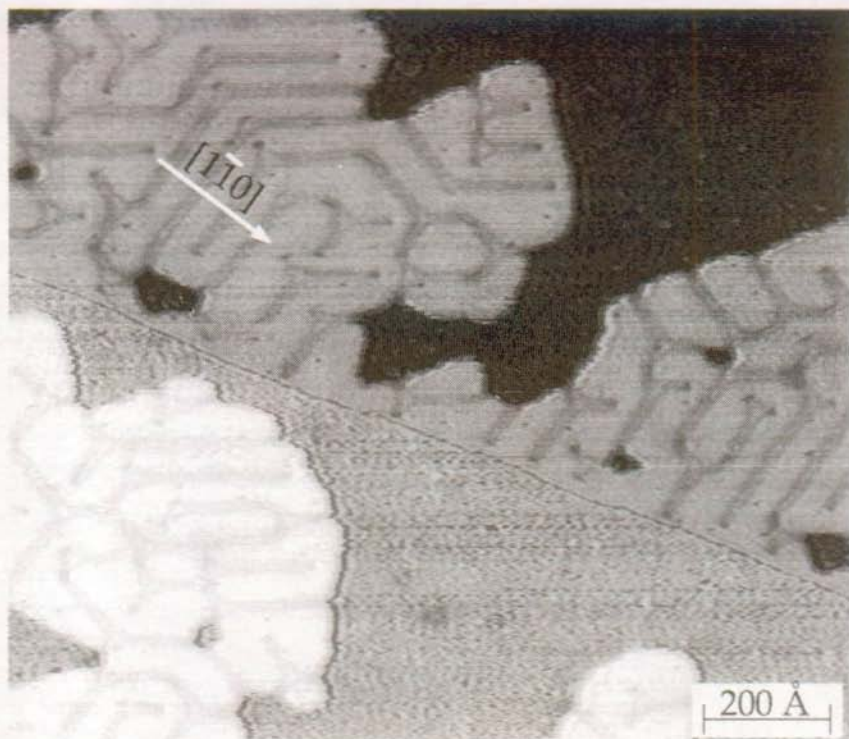


Fig. 4.5: The dislocation network in a first ML Ag-film growing from the steps of the Pt(111) substrate. Coverage 0.5 ML, deposition temperature 500 K.

however, the STM reveals a network of double lines, imaged with a depth of less than  $0.1 \text{ \AA}$  and running along the three  $\langle 11\bar{2} \rangle$  directions perpendicular to the closed packed atom rows as demonstrated in Fig. 4.5. In analogy to similar structures in the literature [58, 59, 147, 148], we infer that the double lines in Fig. 4.5 are two partial dislocations, forming "light" domain walls between fcc and hcp stacking as Ag on Pt(111) is compressively strained by 4.3%. With PED it was found that the first monolayer of Ag grows in fcc-stacking to the substrate. From this and the fact that the dislocations were never found to end at ascending

substrate steps we conclude that the small regions within the double lines have hcp-stacking. This is further corroborated by a recent theoretical study by Ratsch, Seitsonen, and Scheffler [149]. Using density-functional theory (DFT), they found a difference of the adsorption energy per Ag atom of 30 meV in favor of fcc stacking in this system. Where the structure is well ordered over a larger region, the double lines have an average spacing of 75 Å, corresponding to 26 Ag atoms on 27 Pt atoms in the closed packed direction perpendicular to the dislocations. This periodicity agrees well with a simplistic geometric picture where one would expect a  $\sqrt{3} \times 24$  unit cell for complete unidirectional strain relief. Note however that the mesoscopic order of the dislocations is very sensible to defects. Vacancies in the Ag film act as preferential ending points for the dislocations and can cause local variations from their average spacing. They further prevent the formation of large rotational domains.

We followed the dislocation formation as a function of island size and coverage. At 300 K, Ag is sufficiently mobile on the Pt(111) surface that film growth, even on very large terraces, proceeds from substrate step edges. In order to study the influence of island size, we prepared well defined two-dimensional Ag islands by depositing a submonolayer coverage of 10% at 50 K where Ag diffusion is nearly frozen in and subsequent annealing to 300 K. In an Ostwald-ripening process, compact islands form which are homogeneously distributed over the surface [7]. The average size of these islands can then be increased by further deposition of Ag at 300 K. Figure 4.6a shows that small islands grow pseudomorphically whereas on larger ones dislocations have formed. The transition occurs gradually at island diameters around 200 Å (Fig. 4.6b). (We here refer to island diameter as the lateral extension of an island perpendicular to a dislocation). It should be noted that this value is much larger than the average spacing of dislocations in a compact film. This indicates that for islands there must be an additional effective way for strain relief which can only be associated with the edges. For small island sizes, the compressive strain can be efficiently

relieved at the island edges through outward relaxation. But at larger sizes, the accumulated strain is too large and dislocations form. Note that, in contrast to semiconductor systems, in which dislocations evolve at the edges of (3-dimensional) islands where the strain field is maximal [150], here they intersect the islands in their centers.

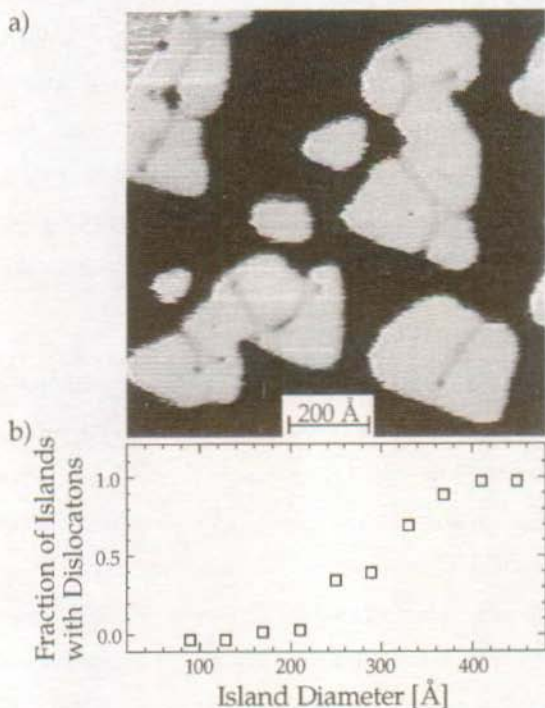
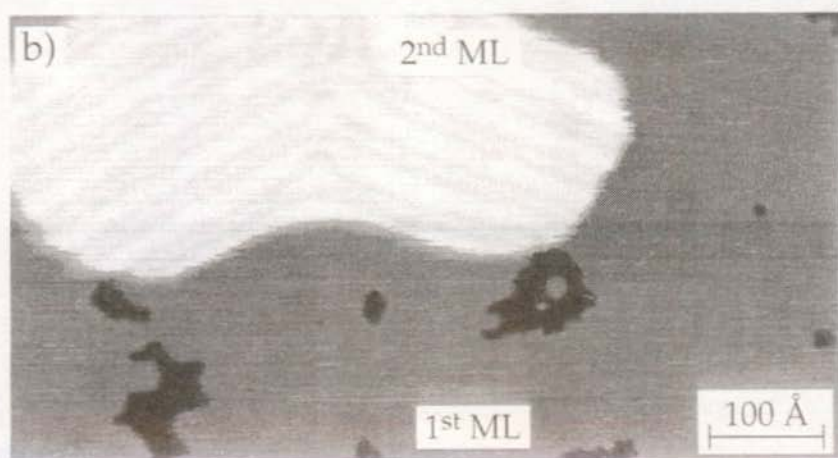
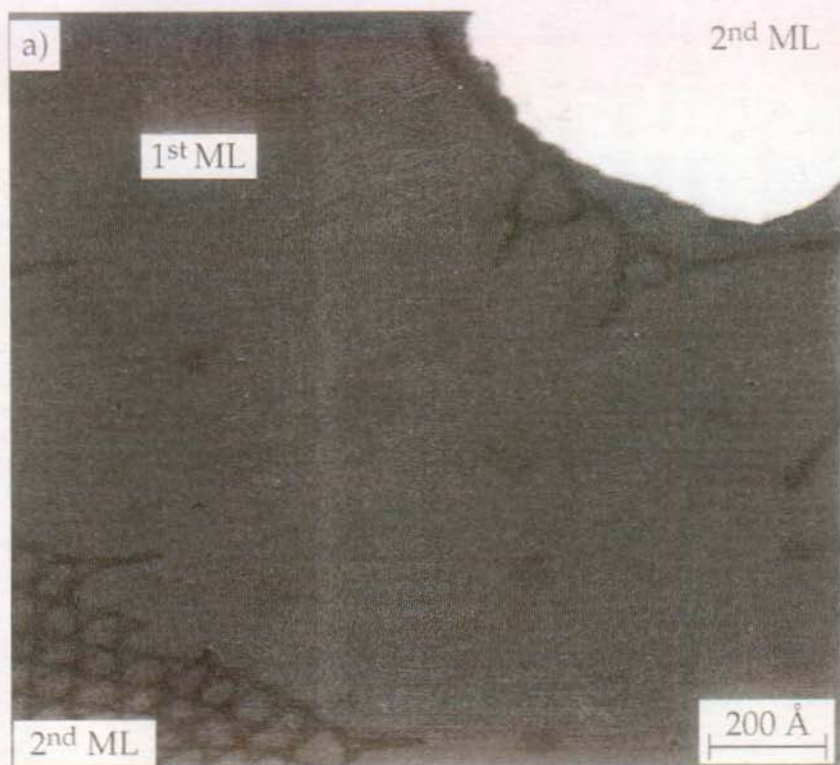


Fig. 4.6: A population of Ag islands on Pt(111) grown by deposition of 0.12 ML Ag at 50 K, subsequent Ostwald ripening, and post-evaporation of 0.25 ML at 300 K (a). Probability of dislocation formation as a function of island size as inferred from analysis of 180 islands (b).

The structures described so far are found in the whole submonolayer range. At coverages around 1 ML, however, the dislocation network in the first layer is lifted. Figure 4.7a shows a 1.4 ML film grown at 400 K after annealing to 800 K.

The equilibrium structure of the 2<sup>nd</sup> ML, a trigonal network of dislocation lines [59], can easily be distinguished from the 1<sup>st</sup> ML. Apart from a few defects induced by the direct vicinity of the 2<sup>nd</sup> ML, the 1<sup>st</sup> ML now is perfectly pseudomorph. Further information about this reentrant pseudomorphic growth can be gained from experiments in which 2<sup>nd</sup> ML islands are grown on a not yet completed 1<sup>st</sup> ML film. (As the first layers of Ag at 300 K grow in a layer-by-layer fashion, this can only be achieved by a multistage deposition process). In such systems, too, no dislocations are found in the 1<sup>st</sup> ML (Fig. 4.7b), which shows that not the completion of the first, but rather the presence of the second ML is the reason for the reentrant pseudomorphic structure.

This finding leads to an explanation of the effect. With the presence of 2<sup>nd</sup> ML material, a 2D adatom gas on top of the Ag film is established which is in equilibrium with the condensed phase. This adatom gas, which is absent without 2<sup>nd</sup> ML material, can shift the equilibrium situation of the film. In a theoretical study, Needs and coworkers [26] argued that three energetic factors have to be considered in determining whether or not a surface is stable against formation of dislocations. First, strain existent at an interface induces elastic energy in the film, which favors dislocation formation. Second, dislocations reduce the bonding energy to the substrate, as at least a part of the atoms in the overlayer has to shift out of registry, which disfavors their formation. Third, the formation of dislocations changes the total number of atoms in the overlayer. The energy changes associated with the transfer of atoms into or out of the surface layer have also to be considered. If the first two contributions are close to balance each other, the chemical potential of an adatom gas on top of the layer in question can hence be the determining factor. Evidently, it is this third aspect which is not accounted for in continuum theories of dislocation formation. Recently, it could be shown for Pt(111) homoepitaxy that an increased chemical potential of an adatom gas can induce a reconstruction of the normally pseudomorphic surface [151]. In our system under compressive strain, the inverse case is expected. Excess atoms from



the adatom gas can be incorporated into the light walls and lift the dislocation network.

We performed effective-medium theory (EMT) calculations<sup>1</sup> to support this conclusion. To study the strain relief mechanism via relaxation at the edges, we calculated the atomic equilibrium positions in a hexagonal Ag island with 61 atoms on a Pt(111) slab. In the calculations, very strong relaxation effects were indeed found to increase the lateral Ag-distances at the island edge to 2.2% above that of the Pt(111) lattice constant. This reduces the effective strain in the Ag at the edge to 1.7%. The lateral shift is accompanied by a downward relaxation of the edge atoms. The vertical difference between a corner atom and an atom in the island center is  $\approx 0.2 \text{ \AA}$ . The relaxation is not restricted to the outmost atoms. In the center of the rather small island, the interatomic Ag-distances were still 1.5% larger than the Pt(111) lattice constant, showing that the effective region for strain relief at the edges extends at least five atomic rows into the island. The relaxation in total is a collective effect of the atoms in the island and in the underlying substrate. The subsurface relaxation effects found here are similar to those discussed below for the case of the dislocation structure.

**Fig. 4.7:** Reentrant pseudomorphic structure of the first ML in the presence of second ML material. Either upon annealing to 800 K and thus creating a first ML film without vacancies (a) or on post-evaporation onto a not yet completed film at 300 K (b), the dislocations disappear.

---

<sup>1</sup> A description of the method is given in [64]; the parameters and computer code used can be found in [65].

Calculations concerning dislocation formation in compact films were carried out with rectangular slabs of  $3\sqrt{3} \times N$  periodicity, with  $N$  ranging from 10 to 50. The thickness of the slabs had to be chosen to comprise at least 20 layers, as strong relaxation effects influenced the subsurface Pt layers considerably to a depth of about 15 layers. To obtain the binding energy per Ag atom  $\epsilon_0$  in a film with dislocations, we first placed a  $3\sqrt{3} \times (N-1)$  Ag-layer (thus containing two partial dislocations) on top of a  $3\sqrt{3} \times N$  Pt-substrate. The total energy of the fully relaxed slab is then subtracted from that of the substrate alone and divided by the number of Ag atoms.<sup>1</sup> The same procedure is then repeated for a pseudomorphic Ag adlayer. Figure 4.8 shows that as soon as  $N > 18$ , dislocation formation is energetically favored. However, the structure with the highest Ag binding energy ( $\epsilon_0 = 2.998$  eV for  $N = 30$ ) is only 3 meV per Ag atom favored compared to that of a pseudomorphic Ag layer (i.e., the energy gain per unit cell is  $\approx 0.08$  eV if we take  $N$  to be 27, the experimentally determined average size of the superstructure). Note, however, that EMT doesn't account for the energetic difference between fcc and hcp sites found with DFT. This difference should drive the system closer towards energetic degeneracy and is responsible for the pair of partial dislocation lines running closely together in the real system whereas they relax towards maximum separation in EMT simulations.

---

<sup>1</sup> Far away from the Pt surface the Ag atoms have a potential energy of 0 eV. During adsorption the total energy of the system Pt-slab + Ag-atom decreases. We refer to binding energy as the difference in total energy of the system before and after adsorption; it is hence a positive value.



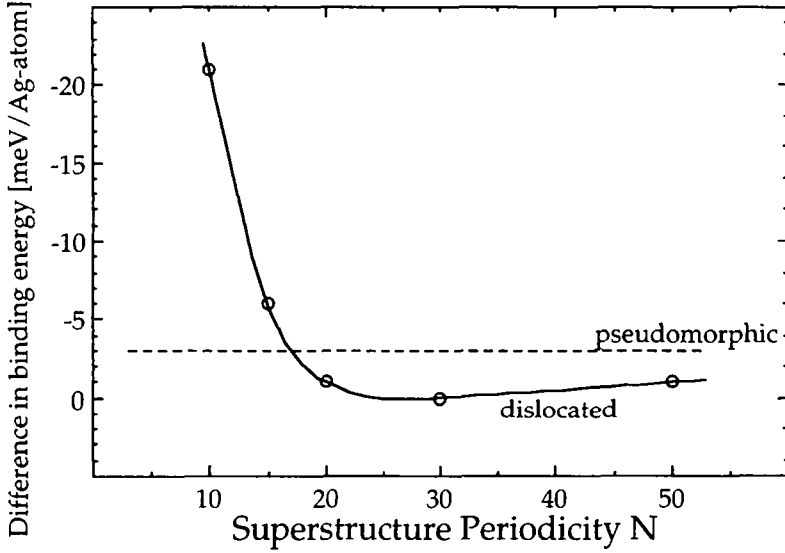


**Fig. 4.8:** Difference in binding energy per Ag atom between Ag adlayers of varying periodicity of the dislocation network and the ground state of the system [a  $(\sqrt{3} \times 29)$  Ag adlayer with two partial dislocations on a  $(\sqrt{3} \times 30)$  Pt(111) substrate; binding energy per Ag atom = 2.998 eV]. The binding energy of the pseudomorphic adlayer is given by the dotted line. As soon as  $N > 18$ , dislocation formation is energetically favored.

An isolated adatom on top of the 1<sup>st</sup> ML is found to be 0.62 eV weaker bound than an atom embedded in the reconstructed 1<sup>st</sup> ML, as calculated with EMT. Consequently, if such adatoms are incorporated into the reconstructed adlayer and the dislocation network is lifted, the system gains about 0.62 eV - 0.08 eV = 0.54 eV per  $\sqrt{3} \times 27$  superstructure lattice cell. Thermodynamically, we can attribute a chemical potential of  $\mu_g = \epsilon - kT \cdot \ln \left[ \frac{A}{N} \frac{2\pi m kT}{h^2} \right]$  to the (ideal) 2D gas of silver atoms on top of the 1<sup>st</sup> ML Ag film ( $\epsilon$  being the adsorption energy of the atoms on top of the first monolayer,  $m$  their mass,  $h$  Planck's constant, and  $N/A$  the density of the atoms). The free energy of the film, on the other hand,



increases by 0.08 eV per incorporated atom, i.e.,  $\mu_f = 0.08$  eV. (Here, we ignore entropy changes associated with the structural transition of the film). Equating chemical potentials for  $T = 300$  K leads to a critical density of 1 atom per  $(3700 \text{ \AA})^2$  at which Ag adatoms of the 2<sup>nd</sup> ML should be incorporated in the 1<sup>st</sup> ML. This density can easily be maintained by adatoms evaporating from the edges of 2<sup>nd</sup> ML islands.

A closer look at the equilibrium positions of the atoms as determined by EMT shows that the absolute height of the Ag atoms in the domain walls, though sitting on bridge sites, is reduced. The depth of the indentations corresponds well to the measured height of the dislocations, showing that not electronic effects but rather pure geometry is sufficient to explain the imaging of the STM. As put forward by Hwang et al. [148], the reason for this behavior lies in a very strong relaxation of the underlying substrate layers. Our EMT calculations reveal that below the dislocations, the first and second Pt layers are depressed by 0.14 and 0.15 Å, respectively. Though the relative distance between the first Pt layer and the Ag atoms on bridge sites is indeed increased, the absolute heights of the latter are reduced.

While we have observed reentrant pseudomorphic growth for a particular model system, its implications for heteroepitaxial growth are of general significance. It is useful to distinguish systems under tensile and compressive strain. In the latter case, strained epitaxial islands tend initially to grow dislocation free. The compressive strain can efficiently be relieved through outward relaxation at island edges, favoring pseudomorphic growth below a critical size. But as islands increase in size, the introduction of misfit dislocations will finally allow for a better elastic relaxation of the island's stress. Dislocation formation in compressively strained layers can, however, be suppressed by the application of an enhanced gas phase chemical potential if the energy gain due to strain relief and the energetic cost of dislocation formation are close to cancel each

other. High supersaturation might thus be used to grow pseudomorphic structures which are otherwise unstable.

In systems with tensile strain, the effect of an enhanced gas phase potential is inverse. Here, the presence of an adatom gas can drive an otherwise pseudomorphic system towards dislocation formation. Examples are the Pt(111) reconstruction during homoepitaxial growth [151] and the Ni monolayer structure on Ru(0001) [66], which is pseudomorphic at submonolayer coverages but becomes dislocated with the build-up of the second Ni layer. The effect of an enhanced adatom chemical potential favoring dislocation formation, however, makes it principally impossible to find a reentrant pseudomorphic behavior in systems under tensile stress.

The authors want to thank Jens Nørskov and his group for the possibility to use their EMT computer code.



## 5 Cluster deposition

In this chapter we study the possibility to use the controlled deposition of size-selected metal clusters to create monodispersed island distributions on surfaces. Our interest focuses on the dependence of the resulting structures on the deposition parameters like cluster size and impact energy. Further, we investigate the possibility to use rare-gas buffer layers for energy dissipation and soft-landing [29, 30]. So far, this possibility has only been examined with optical spectroscopic methods [152]. The experiments show that, first, cluster deposition is indeed a tool to create different types of island populations than obtained in MBE growth, and, second, rare-gas buffer layers protect the surface efficiently from sputter damage induced by the clusters and decrease the widths of the resulting island size distributions.

### 5.1 Controlled Deposition of Size-Selected Silver Nanoclusters

Nanostructure formation at surfaces has been studied extensively both because of the intrinsic interest in structures with reduced dimensions and because of potential technological applications. The most advanced techniques for the synthesis of nanostructured surfaces are atomic manipulation with scanning-probe methods [4-6] and self organized growth [7]. A promising alternative route is the controlled deposition of nanoclusters from the gas phase [29, 48]. The deposition of clusters on a solid substrate is characterized by number of important physical phenomena. When a cluster impinges on the surface, it must transfer its kinetic energy and the energy of condensation to the substrate crystal lattice to ensure efficient sticking. The energy dissipation depends primarily on the relation between cluster-surface and internal cluster binding strength and on the cluster impact energy. At high impact energies, the condensation energy is negligible, and a large amount of energy can be delivered to a localized region of

the surface during the collision, resulting in substantial cluster fragmentation, substrate damage, and even implantation. The extreme nonequilibrium conditions in energetic cluster surface collisions have been exploited to grow smooth films at low temperatures [153]. In contrast, the synthesis of nanostructured surfaces requires low kinetic energies to be released during the impact to ensure a nondestructive deposition in which the nanoclusters maintain their individual characteristics.

Despite considerable recent effort in studying cluster-surface interactions [48, 87, 154-158], the effect of the impact parameters on the result of the deposition process has not been characterized in situ on the microscopic scale to date. We now report the investigation of the deposition of size-selected  $\text{Ag}_n$  clusters ( $n=1, 7, 19$ ) of varying kinetic energy (1 to 14 eV per cluster atom) onto a Pt(111) substrate in ultrahigh vacuum (UHV). Deposition took place either onto the bare surface at 80 or 90 K or into a preadsorbed Ar buffer layer at 26 K, which was subsequently evaporated at 90 K.<sup>1</sup> The surface and cluster morphologies were characterized in situ in the same UHV chamber by variable-temperature scanning tunneling microscopy (STM)(Fig. 5.1) before and after annealing to 300 K. Our study was motivated by the hope of obtaining controlled soft landing through energy dissipation in a rare-gas buffer layer. This possibility was suggested by recent matrix deposition experiments which demonstrated that-size selected Ag clusters codeposited with rare gases do not fragment [152, 159], and by the molecular dynamics simulations of Cheng and Landman [30], who studied in detail the deposition dynamics of Cu nanoclusters on bare and rare-gas covered Cu(111).

---

<sup>1</sup> At temperatures below 100 K, silver dimers and larger clusters are stable on the Pt(111) surface (see for example [13]).

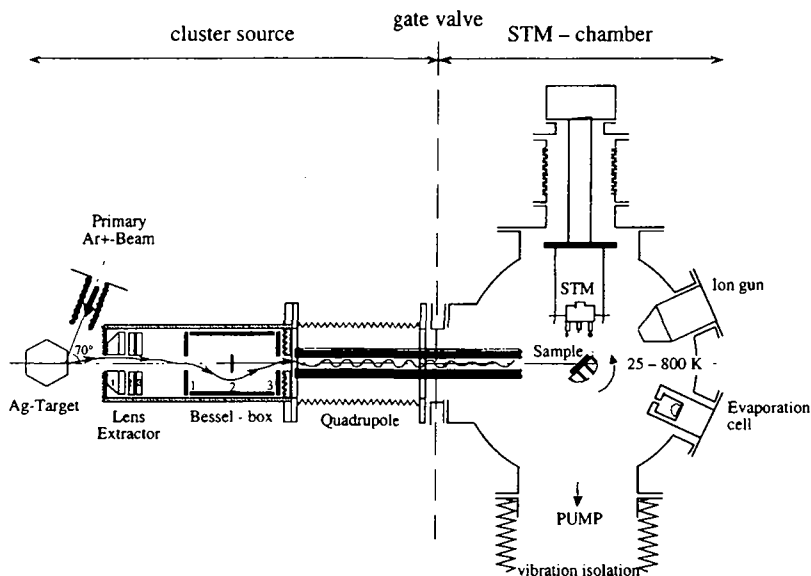


**Fig. 5.1:** The apparatus of the cluster deposition experiment consists of two UHV chambers separated by a gate valve. The Ag clusters were produced by sputtering of an Ag target in a differentially pumped secondary ion source, energy-filtered (Bessel-box), and mass-selected by a quadrupole [48]. During deposition, the non-rare gas background pressure was held in the  $10^{-10}$  mbar range. Cluster current densities were on the order of several  $10^{11}$  atoms  $\text{cm}^{-2} \text{s}^{-1}$ , the equivalent to deposition of 0.1 monolayers in about 10 min. After deposition onto the Pt(111) crystal, the resulting structures can be examined by variable-temperature STM (25 to 800 K). All STM images were measured in constant-current mode, with a typical tunneling resistance of  $10^8 \Omega$ .

A useful reference experiment for the cluster deposition is the "thermal" condensation of vapor-deposited Ag atoms onto the clean Pt(111) surface under otherwise identical conditions, that is, a typical molecular beam epitaxy (MBE) experiment. During thermal growth of 0.1 monolayers (ML) of Ag on Pt(111) at 80 K (Fig. 5.2A), small ramified Ag clusters of monoatomic height were formed in

a nucleation and aggregation process that has been analyzed in detail in Refs. [13, 76]. The average island size was  $\approx 100$  atoms and the island size distribution showed the expected scaling [27] with a rather large normalized standard deviation of  $\sigma^* = 0.55$ . Here,  $\sigma^* = \sigma / \langle s \rangle$  is defined as the standard deviation over all island areas, normalized to the mean island area. Upon annealing of the islands to 300 K, the Ag clusters decayed as a result of Ostwald ripening, that is, by vaporization of single atoms from the island edges into a two-dimensional gas phase, and the Ag condensed at preexistent Pt step edges, leaving behind clean substrate terraces (Fig. 5.2B) [160].

The aggregates that formed after deposition of size-selected nanoclusters showed markedly different structures, exhibiting compact forms (Fig 5.3). Further, the islands created by deposition of (3D) clusters were always observed to

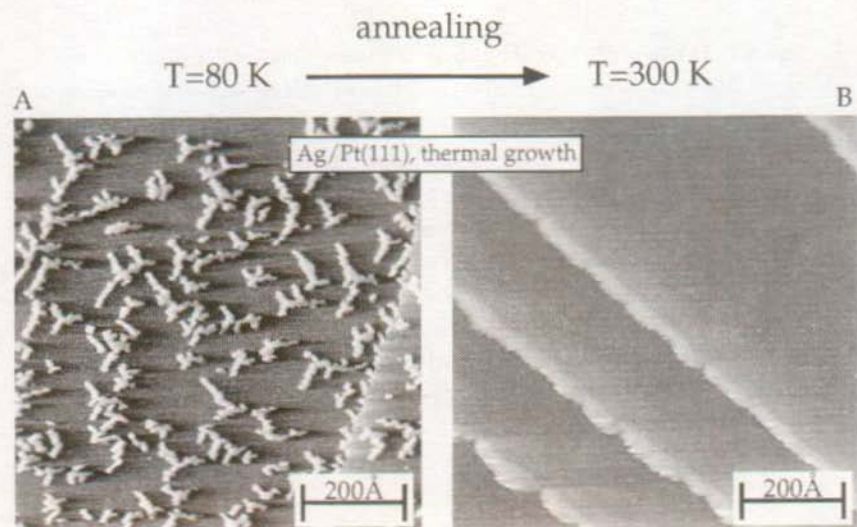


Fig. 5.2: Growth of ramified Ag clusters upon deposition of thermal Ag atoms onto Pt(111) at 80 K. Coverage  $\Theta = 0.1$  ML, deposition flux  $R = 2 \times 10^{-5}$  ML/s. B) The MBE-grown Ag islands decay by Ostwald ripening upon annealing to 300 K.

be two-dimensional (2D) on the surface, that is, of monoatomic height, implying that the 2D structure is energetically favored. This finding can be rationalized using simple bond-counting arguments. For small clusters, a 2D structure permits an increased number of metal-metal bonds<sup>1</sup>.

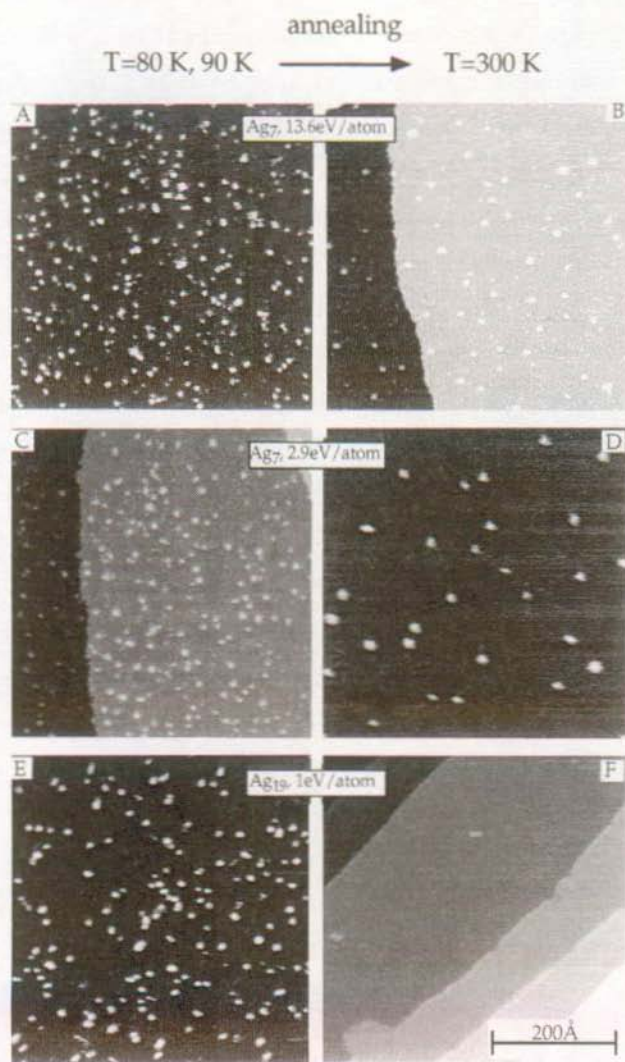
In a deposition experiment, the kinetic energy released during the impact might cause even a more substantial reorganization of the atomic structure, which can include cluster fragmentation or substrate damage. These effects were observed for the "harder" landing conditions investigated. After the low-temperature ( $T = 80$  K) deposition of Ag<sub>7</sub> clusters onto the bare substrate with an impact energy of 95 eV (that is, 13.6 eV per atom) and subsequent annealing to 300 K, there were still small islands found on the terraces (Fig. 5.3, A and B). As explained above, small MBE-grown Ag islands on Pt(111) decay under these conditions by Ostwald ripening. Hence, the cluster deposition process must have created surface defects that now act as pinning centers for the diffusing atoms up to temperatures of at least 300 K. It is likely that these defects are either Pt adatoms or Ag substitutional atoms in the substrate that are created in an exchange process during the energetic impact. Above 600 K, Ag forms a surface alloy with the Pt(111) surface [25, 125]. Locally, this temperature can be reached upon an energetic cluster impact. The density of the pinning centers was found to increase with the kinetic energy per atom of the impinging clusters, saturating at about one pinning center per four to six deposited clusters in the energy range investigated (that is, up to 13.6 eV per cluster atom). In the case of Ag<sub>7</sub> clusters deposited with 2.9 eV per atom, for example, only one pinning center per  $\approx 10$  deposited clusters was created (Fig. 5.3, C and D). This dependency shows the way towards a nondestructive deposition of clusters onto bare substrates: Lowering the kinetic energy per cluster atom should drive the system towards a soft-

---

<sup>1</sup> Effective-medium calculations corroborate this simple picture. For a Ag<sub>7</sub> cluster on Pt(111) we calculated an energy difference of 2.7 eV in favor of the 2D structure.



landing behavior. Indeed, for Ag<sub>19</sub> clusters with a kinetic energy of 20 eV (that is  $\approx 1$  eV per atom), no pinning centers were found and all the deposited material had condensed at the step edges of the substrate crystal after annealing to 300 K (Fig. 5.3, E and F).



The absence of any surface defects does not necessarily imply that the deposition process is nondestructive for the clusters themselves. The released energy might be sufficient to disintegrate the clusters without creating any substrate damage. To investigate this possibility, we examined quantitatively the island size distributions (Table 5.1). As expected, the normalized width  $\sigma^*$  was sharpest for the nondestructive landing and increased with harder landing conditions, indicating substantial fragmentation during the deposition process in the latter cases. The mean island size in the nondestructive landing case corresponded within the experimental error with the number of atoms in the deposited clusters. But even after a hard landing, the average island size on the surface equals the original cluster size, and the width of the size distribution does not exceed that seen in an MBE-growth experiment. This result indicates that parts of the clusters stay together in the fragmentation process and act as effective nucleation sites for released adatoms. The overall island density on the surface is thus determined by the number of deposited clusters.

To study the influence of a rare-gas buffer layer on the deposition process, we compared two similar experiments: the landing of Ag<sub>7</sub> with  $E_{\text{kin}} = 20$  eV on the clean surface (see above) and via an Ar buffer layer. In the latter case, the clusters were deposited at  $T = 26$  K into a preadsorbed Ar layer of about 10 ML [49, 161]. By subsequent annealing to 90 K, the Ar was desorbed, and the clusters could

**Fig. 5.3 (other side):** Destructive and nondestructive deposition of Ag<sub>7</sub> and Ag<sub>19</sub> clusters at 80 K (90 K for E) onto the bare Pt(111) surface. The kinetic energy per cluster atom was 13.6 eV (A), 2.9 eV (C), 1 eV (E). (B, D, and F) The surfaces after annealing to 300 K. Because of the thermal drift during the annealing procedure, the STM does not picture exactly the same spot. By lowering the kinetic energy of the clusters to 1 eV per atom, the deposition process became nondestructive. The size of all images is 500 Å by 500 Å.

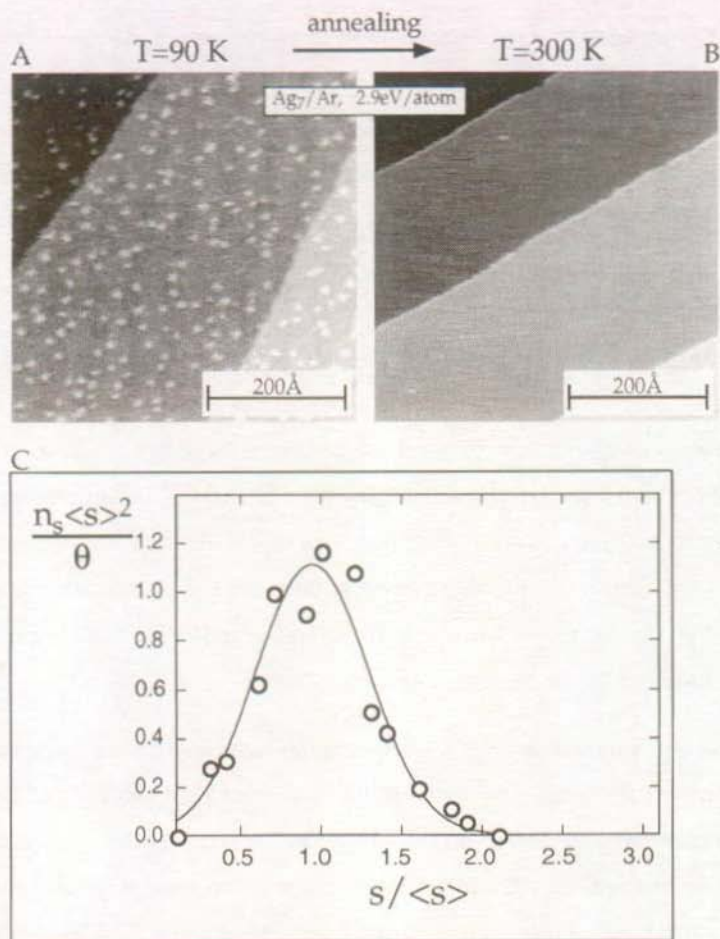


Fig. 5.4: Soft landing of Ag<sub>7</sub> clusters (2.9 eV per atom) through energy dissipation in an Ar buffer layer (10 ML) on Pt(111) at 26 K. The surface is imaged after desorption of the Ar layer at 90 K (A) and after further annealing to 300 K (B). (C) The normalized island size distribution of the aggregates at 90 K. With  $n_s$  being the density of clusters of area  $s$ ,  $\langle s \rangle$  the average cluster area, and  $\theta$  the total Ag coverage,  $n_s \langle s \rangle^2 / \theta$  is the normalized density of clusters of relative size  $s / \langle s \rangle$ . The standard deviation  $\sigma^*$  as a fraction of mean island size is 0.35, compared to  $\sigma^* = 0.49$  for landing on the bare substrate. The line is a Gaussian fit which serves as a guide to the eye.

be imaged on the Pt surface (Fig. 5.4A). In contrast to the bare substrate case, this landing procedure did not create any pinning centers (Fig. 5.4B). Furthermore, the small relative width of  $\sigma^* = 0.35$  indicates a sharp size distribution (Fig. 5.4C).

Our experiments illustrate the possibility of soft landing of nanoclusters through energy dissipation into a rare-gas buffer layer. Clusters, which under otherwise identical conditions decay during the deposition process and create substrate defects, were landed nondestructively by the help of such layers. The opposite case of a hard landing also provides interesting potential for the nanostructuring of surfaces. In our experiments, otherwise thermally unstable

| Cluster size n                            | Kinetic energy (eV) | Kinetic energy per cluster atom | Average size   | Width $\sigma^*$ |
|---|---------------------|---------------------------------|----------------|------------------|
| <i>Thermal atoms</i>                      |                     |                                 |                |                  |
| 1   | 0.2                 | 0.2                             | $f(T, \theta)$ | 0.55             |
| <i>Clusters/bare substrate</i>            |                     |                                 |                |                  |
| 7   | 95                  | 13.6                            | $7 \pm 2$      | 0.54             |
| 19  | 95                  | 5.0                             | $13 \pm 3$     | 0.48             |
| 7   | 20                  | 2.9                             | $8 \pm 2$      | 0.49             |
| 19  | 20                  | 1.0                             | $16 \pm 4$     | 0.37             |
| <i>Clusters/Ar buffer layer/substrate</i> |                     |                                 |                |                  |
| 7   | 20                  | 2.9                             | $7 \pm 2$      | 0.35             |

**Table 5.1:** Analysis of the size distribution of Ag aggregates formed upon low-temperature deposition of size-selected  $\text{Ag}_n$  clusters on Pt(111). The width  $\sigma^*$  of the size distribution is described by the standard deviation over all island areas, normalized to the average island area. The error in the average island size does not describe the width of the distribution, but rather the uncertainty of its center position. In the case of MBE-grown Ag islands, the average island size is a function of temperature and coverage. Note that in the two soft-landing cases the  $\sigma^*$  values are resolution-limited.

structures could be stabilized by the use of defects which were created in the violent deposition process.

#### Annotation to chapter 5.1

The direct connection of cluster source and STM chamber in this experiment caused a shortcut of the external vibration isolation of the STM chamber which had a strong negative effect on the resolution of the microscope. Atomic resolution was not within reach with this set-up. Therefore, the number of atoms in a cluster on the surface could not be determined by direct counting but had to be inferred from the island areas apparent in the STM image. If the islands are large (better, if the ratio of island area to edge perimeter is large so that edge effects can be neglected) this does not influence the relative precision of the measurement very much. If the islands are small, imaging effects of the edges due to the finite curvature of the STM-tip become increasingly important. This, together with the vibrational perturbations of the combined apparatus mentioned above, gave rise to a different imaging of clusters of the same size (the same number of atoms) and lead to an experimental residual width, which can be estimated by the imaging of isolated atoms at very low temperature where diffusion is completely frozen in. For such a system we obtained a relative width of the size distribution of 0.28. However, in the case of larger islands this effect becomes smaller due to the increased area-to-perimeter ratio. This result shows that the experimentally determined widths of the cluster size distributions in the soft-landing cases are already influenced by the resolution limit of our experiment and have, hence, to be regarded as upper limits.

## 6 Outlook

The present thesis deals with metallic nanostructures. It focuses on structural properties of the model system Ag/Pt(111). Three different ways to create nanostructures on metallic surfaces are investigated (self-organized MBE-growth, exploitation of equilibrium properties, and controlled deposition of nano-clusters), and key atomic processes involved in the formation of the structures could be determined.

The present work forms part of a rapidly developing field of scientific research. Nanostructures are studied from many different points of view, and research activities treat a variety of aspects. A possible way to classify the different approaches is to divide them into studies that focus on structural properties and examinations of functionality of the structures, i.e., their electronic, magnetic, superconducting, etc. behavior. Both of these two complementary aspects will be followed in the continuation of the presented work.

Concerning structural aspects, the increased resolution of the microscope allows to reveal further details of atomic behavior and their impact on nanostructure formation. Further, the experience gained in the cluster deposition experiment influenced the design of a new built, combined cluster deposition-STM apparatus in the institute.

Concerning functionality, a magneto-optical Kerr-effect measurement system was developed during this thesis that will be mounted to the STM chamber in the near future. The combination of STM and Kerr-effect measurements provides the possibility to study structural properties in situ with the surface magnetic behavior of a system. Side effects, resulting from the imperfections of real systems like finite terrace widths etc., can be determined, leading to a more direct access to the magnetic properties of the nanostructures.



## 7 References

1. J. Faist, F. Capasso, D. L. Sivco, C. Sirtori, A. L. Hutchinson, and A. Y. Cho, *Science* **264**, 553 (1994).
2. M. F. Doerner and R. L. White, *Mat. Res. Soc. Bull.* **21**, 28 (1996).
3. W. Blum, *Groß, weil klein, Die Zeit*, 49, 18th October, (1996).
4. M. F. Crommie, C. P. Lutz, and D. M. Eigler, *Science* **262**, 218 (1993).
5. P. Avouris, Ed., *Atomic and Nanometer Scale Modification of Materials: Fundamentals and Applications*, (Kluwer, Dordrecht, Netherlands, 1993).
6. P. Avouris, *Accounts Chem. Res.* **28**, 95 (1995).
7. H. Röder, E. Hahn, H. Brune, J. P. Bucher, and K. Kern, *Nature* **366**, 141 (1993).
8. G. Binnig and H. Rohrer, *Helv. Phys. Acta* **55**, 726 (1982).
9. G. Binnig, H. Rohrer, C. Gerber, and E. Weibel, *Phys. Rev. Lett.* **49**, 57 (1982).
10. C. J. Chen, *Introduction to Scanning Tunneling Microscopy*, (Oxford University Press, New York, 1993).
11. J. A. Venables, *Philos. Mag.* **17**, 697 (1973).
12. J. A. Venables, G. D. T. Spiller, and M. Hanbücken, *Rep. Prog. Phys.* **47**, 399 (1984).
13. H. Brune, H. Röder, C. Boragno, and K. Kern, *Phys. Rev. Lett.* **73**, 1955 (1994).
14. T. Michely, M. Hohage, M. Bott, and G. Comsa, *Phys. Rev. Lett.* **70**, 3943 (1993).
15. J. Jacobsen, K. W. Jacobsen, P. Stoltze, and J. K. Nørskov, *Phys. Rev. Lett.* **74**, 2295 (1995).
16. C. Herring, *Phys. Rev.* **82**, 87 (1951).
17. T. A. Witten and L. M. Sander, *Phys. Rev. Lett.* **47**, 1400 (1981).
18. T. A. Witten and L. M. Sander, *Phys. Rev. B* **27**, 5686 (1983).
19. P. Meakin, *Phys. Rev. A* **27**, 1495 (1983).
20. H. Röder, K. Bromann, H. Brune, and K. Kern, *Phys. Rev. Lett.* **74**, 3217 (1995).



21. M. Hohage, M. Bott, M. Morgenstern, Z. Zhang, T. Michely, and G. Comsa, *Phys. Rev. Lett.* **76**, 2366 (1996).
22. R. L. Schwoebel and E. J. Shipsey, *J. Appl. Phys.* **37**, 3682 (1966).
23. R. L. Schwoebel, *J. Appl. Phys.* **40**, 614 (1969).
24. G. Ehrlich and F. G. Hudda, *J. Chem. Phys.* **44**, 1039 (1966).
25. J. Tersoff, *Phys. Rev. Lett.* **74**, 434 (1995).
26. R. J. Needs, M. J. Godfrey, and M. Mansfield, *Surf. Sci.* **242**, 215 (1991).
27. M. C. Bartelt and J. W. Evans, *Phys. Rev. B* **46**, 12675 (1992).
28. J. G. Amar and F. Family, *Phys. Rev. Lett.* **74**, 2066 (1995).
29. H.-P. Cheng and U. Landman, *Science* **260**, 1304 (1993).
30. H.-P. Cheng and U. Landman, *J. Phys. Chem.* **98**, 3527 (1994).
31. T. Michely and C. Teichert, *Phys. Rev. B* **50**, 11156 (1994).
32. T. Michely, Ph.D. Thesis, Universität Bonn (1991).
33. H. Röder, Ph.D. Thesis, Ecole Polytechnique Fédérale de Lausanne (1994).
34. H. Brune, H. Röder, K. Bromann, and K. Kern, *Thin Solid Films* **264**, 230 (1995).
35. Eurotherm 818, Eurotherm Regler GmbH, Limburg, Germany.
36. K. Besocke, *Surf. Sci.* **181**, 145 (1987).
37. G. Binnig and D. P. E. Smith, *Rev. Sci. Instrum.* **57**, 1688 (1986).
38. M. Bott, T. Michely, and G. Comsa, *Rev. Sci. Instrum.* **66**, 4135 (1995).
39. B. Gasser, A. Menck, H. Brune, and K. Kern, *Rev. Sci. Instrum.* **67**, 1925 (1996).
40. Newport Vibration Control System, Newport Corporation, Irvine, CA 92714, USA.
41. Besocke-Delta-Phi-Elektronik, Postfach 2243, 52428 Jülich, Germany.
42. STM 2000, RHK Technology Inc., Rochester Hills, MI 48309, USA.
43. H. Brune, Ph.D. Thesis, Freie Universität Berlin (1992).
44. J. Wiechers and R. J. Behm, Universität Ulm.
45. J. Tersoff and D. R. Hamann, *Phys. Rev. Lett.* **50**, 1998 (1983).
46. J. Tersoff and D. R. Hamann, *Phys. Rev. B* **31**, 805 (1985).

47. J. Wintterlin, J. Wiechers, H. Brune, T. Gritsch, H. Höfer, and R. J. Behm, *Phys. Rev. Lett.* **62**, 59 (1989).
48. G. Vandoni, C. Félix, R. Monot, J. Buttet, and W. Harbich, *Chem. Phys. Lett.* **229**, 51 (1994).
49. J. Unguris, L. W. Bruch, E. R. Moog, and M. B. Webb, *Surf. Sci.* **109**, 522 (1981).
50. G. Ehrlich, *Surf. Sci.* **246**, 1 (1991).
51. G. L. Kellogg, *Surf. Sci. Rep.* **21**, 1 (1994).
52. M. Bott, M. Hohage, M. Morgenstern, T. Michely, and G. Comsa, *Phys. Rev. Lett.* **76**, 1304 (1996).
53. J. Li, R. Berndt, and W.-D. Schneider, *Phys. Rev. Lett.* **76**, 1888 (1996).
54. B. Müller, B. Fischer, L. Nedelmann, H. Brune, and K. Kern, *Phys. Rev. B* in press (1996).
55. G. S. Bales and D. C. Chrzan, *Phys. Rev. B* **50**, 6057 (1994).
56. J. Tersoff, A. W. D. v. d. Gon, and R. M. Tromp, *Phys. Rev. Lett.* **72**, 266 (1994).
57. J. H. v. d. Merwe, D. L. Tönsing, and P. M. Stoop, *Surf. Sci.* **312**, 387 (1994).
58. C. Günther, J. Vrijmoeth, R. Q. Hwang, and R. J. Behm, *Phys. Rev. Lett.* **74**, 754 (1995).
59. H. Brune, H. Röder, C. Boragno, and K. Kern, *Phys. Rev. B* **49**, 2997 (1994).
60. S. V. Ghaisas, *Surf. Sci.* **223**, 441 (1989).
61. H. Brune, H. Röder, C. Romainczyk, C. Boragno, and K. Kern, *Appl. Phys. A* **60**, 167 (1995).
62. C. Romainczyk, M. Krzyzowski, P. Zeppenfeld, G. Comsa, and K. Kern, to be published (1995).
63. G. Rangelov, T. Fauster, U. Strüder, and J. Küppers, *Surf. Sci.* **331-333**, 948 (1995).
64. K. W. Jacobsen, J. K. Nørskov, and M. J. Puska, *Phys. Rev. B* **35**, 7423 (1987).
65. P. Stoltze, *J. Phys. Condens. Matter* **6**, 9495 (1994).
66. J. A. Meyer, P. Schmid, and R. J. Behm, *Phys. Rev. Lett.* **74**, 3864 (1995).
67. D. D. Chambliss, K. E. Johnson, R. J. Wilson, and S. Chiang, *J. Magn. and Magn. Mat.* **121**, 1 (1993).
68. B. Fischer, L. Nedelmann, A. Fricke, H. Brune, and K. Kern, in preparation.

69. J. Jacobsen, K. W. Jacobsen, and P. Stoltze, *Surf. Sci.* **317**, 8 (1994).
70. T. Michely, M. Hohage, S. Esch, and G. Comsa, *Surf. Sci.* **349**, L89 (1996).
71. D. Grier, E. Ben-Jacob, R. Clarke, and L. M. Sander, *Phys. Rev. Lett.* **56**, 1264 (1986).
72. Y. Sawada, A. Dougherty, and J. P. Gollub, *Phys. Rev. Lett.* **56**, 1260 (1986).
73. M. B. Amer, P. Pelcé, and P. Tabeling, *Growth and Form: nonlinear aspects*, (Plenum Press, New York, 1991).
74. H. Takayasu, *Fractals in the physical sciences*, (Manchester University Press, Manchester, New York, 1990).
75. P. Meakin, *Phys. Rev. A* **33**, 3371 (1986).
76. H. Brune, C. Romainczyk, H. Röder, and K. Kern, *Nature* **369**, 469 (1994).
77. J. Nittmann and H. E. Stanley, *J. Phys. A: Math. Gen.* **20**, L1185 (1987).
78. T. Vicsek, *Fractal Growth Phenomena*, (World Scientific, Signapore, 1989).
79. P. Meakin, *Phys. Rev. A* **36**, 332 (1987).
80. D. D. Chambliss and R. J. Wilson, *J. Vac. Sci. Technol. B* **9**, 928 (1991).
81. A. Brodde, G. Wilhelmi, D. Badt, H. Wengelnik, and H. Neddermeyer, *J. Vac. Sci. Technol. B* **9**, 920 (1991).
82. R. Q. Hwang, J. Schröder, C. Günther, and R. J. Behm, *Phys. Rev. Lett.* **67**, 3279 (1991).
83. M. C. Bartelt and J. W. Evans, *Surf. Sci.* **314**, L829 (1994).
84. G. S. Bales and D. C. Chrzan, *Phys. Rev. Lett.* **74**, 4879 (1995).
85. A. Pimpinelli, J. Villain, and D. E. Wolf, *J. Phys. (Paris)* **3**, 447 (1993).
86. P. Jensen, A. L. Barabási, H. Larraide, S. Halvin, and H. E. Stanley, *Nature* **368**, 22 (1994).
87. L. Bardotti, P. Jensen, A. Hoareau, M. Treilleux, and B. Cabaud, *Phys. Rev. Lett.* **74**, 4694 (1995).
88. S. Liu, Z. Zhang, G. Comsa, and H. Metiu, *Phys. Rev. Lett.* **71**, 2967 (1993).
89. Z. Zhang, X. Chen, and M. G. Lagally, *Phys. Rev. Lett.* **73**, 1829 (1994).
90. S. C. Wang and G. Ehrlich, *Phys. Rev. Lett.* **67**, 2509 (1991).
91. J. Kertész and T. Vicsek, *J. Phys. A: Math. Gen.* **19**, L257 (1986).
92. W. W. Mullins and R. F. Sekerka, *J. Appl. Phys. A* **34**, 323 (1963).
93. E. Bauer, *Z. Kristallogr.* **110**, 372 (1958).

94. R. Kunkel, B. Poelsema, L. K. Verheij, and G. Comsa, *Phys. Rev. Lett.* **65**, 733 (1990).
95. S. Esch, M. Hohage, T. Michely, and G. Comsa, *Phys. Rev. Lett.* **72**, 518 (1994).
96. H. A. v. d. Vegt, H. M. v. Pinxteren, M. Lohmeier, E. Vlieg, and J. M. Thornton, *Phys. Rev. Lett.* **68**, 3335 (1992).
97. G. Rosenfeld, R. Servaty, C. Teichert, B. Poelsema, and G. Comsa, *Phys. Rev. Lett.* **71**, 895 (1993).
98. J. Vrijmoeth, H. A. v. d. Vegt, J. A. Meyer, E. Vlieg, and R. J. Behm, *Phys. Rev. Lett.* **72**, 3843 (1994).
99. D. W. Bassett, *Surf. Sci.* **53**, 74 (1975).
100. S. C. Wang and T. T. Tsong, *Surf. Sci.* **121**, 85 (1982).
101. C. Romainczyk, Ph.D. Thesis, Ecole Polytechnique Fédérale de Lausanne (1994).
102. Y. Li and A. E. DePristo, *Surf. Sci.* **319**, 141 (1994).
103. H. Brune, K. Bromann, H. Röder, K. Kern, J. Jacobsen, P. Stolze, K. Jacobsen, and J. Nørskov, *Phys. Rev. B* **52**, R14380 (1995).
104. R. Stumpf and M. Scheffler, *Phys. Rev. Lett.* **72**, 254 (1994).
105. M. Villarba and H. Jónsson, *Surf. Sci.* **317**, 15 (1994).
106. J. A. Meyer, J. Viemoeth, H. A. v. d. Vegt, E. Vlieg, and R. J. Behm, *Phys. Rev. B* **51**, 14790 (1995).
107. T. Härtel, U. Strüber, and J. Küppers, *Thin Solid Films* **229**, 163 (1993).
108. F. Sette, T. Hashizume, F. Comin, A. A. MacDowell, and P. H. Citrin, *Phys. Rev. Lett.* **61**, 1384 (1988).
109. J. L. Stevens and R. Q. Hwang, *Phys. Rev. Lett.* **74**, 2078 (1995).
110. J. Jacobsen, L. P. Nielsen, F. Besenbacher, I. Stensgaard, E. Lægsgaard, T. Rasmussen, K. W. Jacobsen, and J. K. Nørskov, *Phys. Rev. Lett.* **75**, 489 (1995).
111. M. Seul and M. J. Sammon, *Phys. Rev. Lett.* **64**, 1903 (1990).
112. K. To, S. Akamatsu, and F. Rondelez, *Europhys. Lett.* **70**, 343 (1993).
113. M. Seul and V. S. Chen, *Phys. Rev. Lett.* **70**, 1658 (1993).
114. M. Seul, L. R. Monar, L. O'Gorman, and R. Wolfe, *Science* **254**, 1616 (1991).

115. K. Kern, H. Niehus, A. Schatz, P. Zeppenfeld, J. Goerge, and G. Comsa, *Phys. Rev. Lett.* **67**, 855 (1991).
116. T. Garel and S. Doniach, *Phys. Rev. B* **26**, 325 (1982).
117. D. Andelman, F. Borchard, and J.-F. Joanny, *J. Chem. Phys.* **86**, 3673 (1987).
118. Y. Yafet and E. M. Gyorgy, *Phys. Ref. B* **38**, 9145 (1988).
119. M. M. Hurley and S. J. Singer, *Phys. Ref. B* **46**, 5783 (1992).
120. P. Zeppenfeld, M. Krzyzowski, C. Romainczyk, G. Comsa, and M. G. Lagally, *Phys. Rev. Lett.* **72**, 2737 (1994).
121. D. Vanderbilt, *Surf. Sci.* **286**, L300 (1992).
122. K.-O. Ng and D. Vanderbilt, *Phys. Ref. B* **52**, 2177 (1995).
123. V. I. Marchenko, *JETP Lett.* **55**, 73 (1992).
124. J. Tersoff and R. M. Tromp, *Phys. Rev. Lett.* **70**, 2782 (1993).
125. H. Röder, R. Schuster, H. Brune, and K. Kern, *Phys. Rev. Lett.* **71**, 2086 (1993).
126. A. F. Becker, G. Rosenfeld, B. Poelsema, and G. Comsa, *Phys. Rev. Lett.* **70**, 477 (1993).
127. H. Hörnis, J. R. West, E. H. Conrad, and R. Ellialtioglu, *Phys. Rev. B* **47**, 13055 (1993).
128. R. A. Swalin, *Thermodynamics of Solids*, (Wiley, New York, 1962).
129. B. Poelsema and G. Comsa, *Scattering of Thermal Energy Atoms from Disordered Surfaces*, Springer Tracts in Modern Physics 115, (Springer Verlag, Berlin, 1989).
130. W. A. Schlup and K. H. Rieder, *Phys. Ref. Lett.* **56**, 73 (1986).
131. H. Kubo, I. Cornelis, and C. M. Wayman, *Acta Met.* **28**, 405 (1980).
132. D. Vanderbilt, in *Computations for the Nano-Scale*, Eds. P. E. Blöchl, (Kluwer, 1993), p. 1.
133. J. V. Barth, H. Brune, G. Ertl, and R. J. Behm, *Phys. Rev. B* **42**, 9307 (1990).
134. S. Narasimhan and D. Vanderbilt, *Phys. Rev. Lett.* **69**, 1564 (1992).
135. V. I. Marchenko, *JETP Lett.* **33**, 381 (1981).
136. O. L. Alerhand, D. Vanderbilt, R. D. Meade, and J. D. Joannopoulos, *Phys. Rev. Lett.* **61**, 1973 (1988).
137. V. I. Marchenko and A. Y. Parshin, *Sov. Phys. JETP* **52**, 129 (1981).

138. H. Röder, H. Brune, J. P. Bucher, and K. Kern, *Surf. Sci.* **298**, 121 (1993).
139. P. Zeppenfeld, M. A. Krzyzowski, C. Romainczyk, R. David, G. Comsa, H. Röder, K. Bromann, H. Brune, and K. Kern, *Surf. Sci. Lett.* **342**, L1131 (1995).
140. J. Fassbender, U. May, B. Schirmer, R. M. Jungblut, B. Hillebrands, and G. Güntherodt, *Phys. Rev. Lett.* **75**, 4476 (1995).
141. F. C. Frank and J. H. v. d. Merwe, *Proc. R. Soc. London A* **198**, 205 (1949).
142. J. Frenkel and T. Kontorova, *Zh. Eksp. Teor. Fiz.* **8**, 1340 (1939).
143. W. A. Jesser and D. Kuhlmann-Wilsdorf, *Phys. Stat. Sol.* **19**, 95 (1967).
144. J. W. Matthews and A. E. Blakeslee, *J. Cryst. Growth* **27**, 118 (1974).
145. J. H. v. d. Merwe and C. A. B. Ball, in *Material Science Series, Epitaxial Growth*, Eds. J. W. Matthews, (Academic Press, London, 1975), p. 493.
146. B. Müller, B. Fischer, L. Nedelmann, A. Fricke, and K. Kern, *Phys. Rev. Lett.* **76**, 2358 (1996).
147. G. O. Pötschke and R. J. Behm, *Phys. Rev. B* **44**, 1442 (1991).
148. R. Q. Hwang, J. C. Hamilton, J. L. Stevens, and S. M. Foiles, *Phys. Rev. Lett.* **75**, 4242 (1995).
149. C. Ratsch, A. P. Seitsonen, and M. Scheffler, to be published .
150. Y. Chen and J. Washburn, *Phys. Rev. Lett.* **77**, 4046 (1996).
151. M. Bott, M. Hohage, T. Michely, and G. Comsa, *Phys. Rev. Lett.* **70**, 1489 (1993).
152. W. Harbich, S. Fedrigo, J. Buttet, and D. M. Lindsay, *Mat. Res. Soc. Symp.* **206**, 369 (1991).
153. I. Yamada, *Appl. Surf. Sci.* **43**, 23 (1989).
154. Y. Kuk, M. F. Jarrold, P. J. Silverman, J. E. Bower, and W. L. Brown, *Phys. Rev. B* **39**, 11168 (1989).
155. W. Eberhardt, P. Fayet, D. M. Cox, Z. Fu, A. Kaldor, R. Sherwood, and D. Sondericker, *Phys. Rev. Lett* **64**, 780 (1990).
156. P. M. S. John, R. D. Beck, and R. L. Whetten, *Phys. Rev. Lett* **69**, 1467 (1992).
157. H.-V. Roy, P. Fayet, F. Patthey, W.-D. Schneider, B. Delley, and C. Massobrio, *Phys. Rev. B* **49**, 5611 (1994).
158. G. M. Francis, I. M. Goldby, L. Kuipers, B. v. Issendorf, and R. E. Palmer, *J. Chem. Soc., Dalton Trans.* 665 (1996).
159. S. Fedrigo, W. Harbich, and J. Buttet, *Phys. Rev. B* **47**, 10706 (1993).

- 160. H. Röder, H. Brune, and K. Kern, *Phys. Rev. Lett.* **73**, 2143 (1994).
- 161. P. Zeppenfeld, U. Becher, K. Kern, and G. Comsa, *Phys. Rev. B* **45**, 5179 (1992).

# Merci!!!

Merci beaucoup à tous ceux qui ont contribué à l'élaboration de cette thèse:

au Prof. Klaus Kern, mon directeur de thèse, pour m'avoir donné l'opportunité de réaliser le travail présent et pour son engagement tout au long de ce temps. J'ai particulièrement apprécié son esprit d'initiative, sa disponibilité et son soutien en toutes circonstances;

à Harri Brune, le meilleur post-doc et assistant du monde. L'aboutissement de ce travail doit beaucoup à sa clairvoyance remarquable devant les problèmes. Les heures passées ensemble, au labo et dehors, resteront une de mes meilleures souvenirs de mon temps à Lausanne;

à l'équipe du labo, Holger Röder, Christian Félix, Marcella Giovannini et Pascal Vallotton, pour leur collaboration fructueuse;

à tous les collaborateurs des ateliers de mécanique et d'électronique pour leur précieuse contribution et à Claire-Lise Bandelier qui a réalisé beaucoup des figures de ce manuscrit;

à tous les assistant(e)s, post-docs et doctorant(e)s dans le group et dans l'institut pour avoir créé une bonne atmosphère;

et à tous ceux qui ne sont pas mentionnés ici par nom, surtout mes parents et mes amis qui m'ont accompagné pendant mes études avec intérêt et soutien.



# Curriculum Vitae

## Personal

Name: Karsten Bromann  
Address: Avenue de Montoie 2  
1007 Lausanne  
Switzerland  
Date of birth: 08.10.1965 in Celle, Germany

## Education

1972 - 1976 Primary school in Celle  
1976 - 1985 Secondary school in Celle  
1987 - 1993 Study of physics at the University of Hamburg  
Philosophy as subsidiary subject  
Diploma thesis at the Institute of Applied Physics, Prof. Dr. U. Merkt: "Ferninfrarotspektroskopie an Quantentopfstrukturen aus  $\text{Hg}_{1-x}\text{Cd}_x\text{Te}$ "  
(Far-infrared spectroscopy of quantum well structures of  $\text{Hg}_{1-x}\text{Cd}_x\text{Te}$ )  
since 1994 Ph.D. student at the Ecole Polytechnique Fédérale de Lausanne,  
Institute of Experimental Physics, Prof. Dr. K. Kern  
Scientific research activities: epitaxial metal growth, metal nanostructures